2014

Numerical and experimental investigation of turbulence and transport in mixing geometries

Katrine Marsteng Nilsen
Iowa State University

Numerical and experimental investigation of turbulence and transport in mixing geometries

by

Katrine Marsteng Nilsen

A dissertation submitted to the graduate faculty

in partial fulfillment of the requirements for the degree of

DOCTOR OF PHILOSOPHY

Major: Mechanical Engineering

Program of Study Committee:

Michael G. Olsen, Major Professor

Rodney O. Fox

James C. Hill

Terrence Meyer

Shankar Subramaniam

Iowa State University

Ames, Iowa

2014

TABLE OF CONTENTS

LIST OF TABLES

LIST OF FIGURES

ACKNOWLEDGEMENTS

I would like to take this opportunity to express my thanks to those who helped me with various aspects of conducting research and the writing of this thesis. First and foremost, Dr. Michael G. Olsen for his guidance and support and confidence in me throughout this research and the writing of this thesis. I would also like to thank Dr. Rodney O. Fox and Dr. James C. Hill for their insights and great advice. To fellow students, whose effort, support and contributions have been very valuable, thank you. I would further like to thank Dr. Bo Kong for his support and for patiently sharing his knowledge. To my family and friends, thank you for your love and support.

ABSTRACT

Turbulent mixing processes in three different flow configurations are studied using a combination of experimental data and computational fluid dynamics. The turbulent transport of a passive scalar in a wake and jet with co-flow in a rectangular reactor is studied using large eddy simulation and experimental data from particle image velocimetry (PIV), planar laser-induced fluorescence (PLIF), and simultaneous PIV/PLIF. In addition, the vortex flow in a four-inlet vortex reactor is studied by means of Reynolds-averaged Navier-Stokes simulations and stereo-PIV. The investigations shed light on the flow features and mixing mechanisms of the flows and provide in-depth evaluation of the effect of simulation parameters and performance of the numerical methods.

This work shows that computational fluid dynamics in combination with PIV/PLIF data is an excellent tool to study mixing in the current flow configurations. Furthermore, this work demonstrates the value of in-depth evaluation of CFD methods.

CHAPTER 1. INTRODUCTION

1.1 General background

Turbulent flows are all around us, and still our knowledge of this complex phenomenon is far from complete. Turbulence contributes to mixing and plays an important role in many situations, for example in chemically reacting flows, heat transfer, and pollution dispersion. In industry, turbulence is often used to enhance mixing, and chemical reactors are commonly designed to operate in the turbulent regime. An understanding of the turbulent transport processes is then crucial for reactor design and optimization. It is therefore highly relevant to study turbulent mixing.

Experimental investigation of turbulent flows has a long history, starting with simple visualization techniques and qualitative descriptions, and advancing to today's highly sophisticated quantitative measurement methods. A beneficial aid in expanding our understanding of turbulent mixing and an important addition to experimental investigation methods is computational fluid dynamics (CFD). CFD is a relatively new field and is under constant development. It has the potential to provide more extensive data than experiments can at a lower cost. However, in order to use CFD to study turbulence, validation of the simulation methods is necessary. Therefore, experimental studies of turbulent flows serves two purposes; to gain knowledge of the turbulence directly and to use as basis for validation of numerical simulations.

1.1.1 Turbulent mixing

Turbulence is characterized by the momentum forces of a flow being larger than the viscous forces, causing chaotic motion. This results in a large range of scales in the flow; from the smallest, energy dissipating eddies to the large, coherent structures of the flow. Thus, although the governing equations of turbulent flows are known, there is no simple solution to them. The Navier-Stokes and the continuity equations are the governing equations for fluid flow. For incompressible flows they are given by

$$\frac{\partial u_i}{\partial t} + u_j \frac{\partial u_i}{\partial x_j} = -\frac{1}{\rho}\frac{\partial p}{\partial x_i} + \nu \frac{\partial^2 u_i}{\partial x_j x_j} \tag{1.1}$$

$$\frac{\partial u_i}{\partial x_i} = 0 \tag{1.2}$$

where u_i are components of velocity, t is time, ρ is density, p is pressure, ν is viscosity and x_i are spatial coordinates.

A passive scalar is a contaminant that is transported by the flow but that has no influence on the flow itself. Studying turbulent transport of a passive scalar is not only useful in passive scalar applications, it can also teach us important lessons about turbulence. The transport of a passive scalar, ϕ, is given by

$$\frac{\partial \phi}{\partial t} + u_i \frac{\partial \phi}{\partial x_i} = D \frac{\partial^2 \phi}{\partial x_i \partial x_i} \tag{1.3}$$

where D is the diffusivity of the passive scalar in the fluid. Warhaft [98] gives a review of passive scalars in turbulent flows and points out that the need for further research on this topic is prominent.

1.1.2 Advanced experimental methods

Because of the complex nature of turbulent mixing, detailed data are necessary in order to obtain understanding of the underlying mechanisms. Traditional experimental methods of studying turbulence are either point-wise quantitative methods such as pitot

tubes and hot-wires, or full-field methods of a qualitative nature such as smoke visualization. Ideally, one would like full-field *quantitative* measurements in order to study the mechanisms of turbulence and turbulent transport. Particle image velocimetry (PIV) and planar laser-induced fluorescence (PLIF) are two non-intrusive, laser-based measurement methods that provide full-field velocity and concentration data. Thus, the methods are excellent tools in studying turbulence and turbulent mixing and provide terrific basis for evaluating simulation methods.

In PIV the fluid is seeded with neutrally buoyant tracer particles. A pulsating laser sheet is used to illuminate the flow with the tracer particles in a given plane. The laser light is scattered off of the tracer particles so that a camera can capture particle images. The laser pulses must be so short that the particles move minimally during the pulse. The displacement of the particles between two succeeding images can be found and knowing the time difference between two images, velocity vectors can be obtained. Adrian [1] gives a thorough description of the method.

In PLIF, a fluorescent dye is added to the flow. The laser light is used to excite the dye and a camera captures the emitted fluorescent light. Using a carefully selected amount of dye and calibrating to reduce noise, local dye concentration can be deduced from local intensity of fluorescent light.

These two procedures can be applied simultaneously by adding both tracer particles and dye to the flow and letting the laser sheet illuminate the tracer particles as well as excite the dye. The light scattered from the particles and the emitted fluorescent light will have different wavelengths and can thus be separated and directed to separate cameras. The pictures can then be evaluated separately according to the PIV and PLIF procedures and the result is simultaneous velocity and concentration data. Thus this data can give very valuable information about turbulent mixing. Examples of simultaneous PIV/PLIF can be found in [7, 44, 23].

1.1.3 Computational fluid dynamics

In computational fluid dynamics (CFD) the governing equations are attempted solved numerically. The fluid domain is divided into a finite number of parts and the governing equations are discretized and solved for each part. In order to obtain a sufficiently accurate solution when solving the discretized equations directly, the domain must be resolved down to the smallest scale of the flow. This approach is called direct numerical simulation (DNS). Most practical flows are too complex for DNS to be feasible, it would require too much computer power. Instead, simplifications must be made and models are introduced. Two main approaches for reducing the complexity of the problem are Reynolds-averaging and spatial filtering.

The Reynolds-averaged Navier-Stokes (RANS) approach is an ensemble-averaging of the governing equations and solving the resulting equations for the mean values while modeling the effect of turbulence. The averaged equations take the form

$$\frac{\partial \bar{u}_i}{\partial t} + \bar{u}_j \frac{\partial \bar{u}_i}{\partial x_j} = -\frac{1}{\rho}\frac{\partial \bar{p}}{\partial x_i} + \nu \frac{\partial^2 \bar{u}_i}{\partial x_j x_j} - \frac{\partial \overline{u'_j u'_i}}{\partial x_j} \tag{1.4}$$

$$\frac{\partial \bar{u}_i}{\partial x_i} = 0 \tag{1.5}$$

where overbar indicates averaged values and $u_i = \bar{u}_i + u'_i$. The last term of equation 1.4 is a derivative of the Reynolds stress tensor, $\overline{u'_j u'_i}$, and is the only unclosed term. It is through the Reynolds stress tensor that the effect of turbulence enters the equation. Commonly, the effect of turbulence is modeled as an enhanced diffusion and an eddy viscosity is introduced.

$$-\overline{u'_j u'_i} \approx \nu_T \left(\frac{\partial \bar{u}_i}{\partial x_j} + \frac{\partial \bar{u}_j}{\partial x_i} \right) \tag{1.6}$$

The modeling is then reduced to modeling ν_T. One of the earliest and the most widely used model is the k-ϵ model [47] in which

$$\nu_T = C_\mu \frac{k^2}{\epsilon} \tag{1.7}$$

and C_μ is a constant, k is turbulent kinetic energy and ϵ is energy dissipation. k and ϵ are determined by solving model transport equations.

Although RANS with k-ϵ model is widely used, there are many limitations to the method and it is not applicable to all flows. For example, the model does not correctly account for anisotropy in the flow. Near solid boundaries, the model is not able to predict the flow accurately and adjustments such as wall functions are needed. Also, in flows where strong streamline curvature or rotation is present, the model has limitations.

A more extensive approach is to solve model equations for the transport of the Reynolds stress tensor. These models are called Reynolds-stress models. This approach has several advantages, one of them is that anisotropy can better be represented. However, a drawback of this method is added computer costs because more equations are solved.

Although numerous efforts have been invested in developing new models and improving existing ones, attempting to address some of the issues or to expand the range of applicable flows, there is still much room for improvement. Therefore, RANS turbulence modeling is a subject of ongoing research.

Large eddy simulation (LES) is based on the assumption that the large scales of turbulence are the most influential and the smallest scales are universal and can be modeled. The governing equations for the large, resolved scales are obtained by filtering equations 1.1 and 1.2 and modeling the effect of the unresolved scales. The filtered equations take the forms

$$\frac{\partial \tilde{u}_i}{\partial t} + \frac{\partial}{\partial x_j}(\tilde{u}_i \tilde{u}_j) = -\frac{1}{\rho}\frac{\partial \tilde{p}}{\partial x_i} + \nu \frac{\partial}{\partial x_j}(\frac{\partial \tilde{u}_i}{\partial x_j} + \frac{\partial \tilde{u}_j}{\partial x_i}) - \frac{\partial \tau_{ij}}{\partial x_j} \tag{1.8}$$

$$\frac{\partial \tilde{u}_i}{\partial x_i} = 0 \tag{1.9}$$

where tilde represents filtered values. The effect of the unresolved scales enters through the subgrid tensor, τ_{ij} as defined in

$$\tau_{ij} = (\widetilde{u_i u_j}) - \tilde{u}_i \tilde{u}_j \tag{1.10}$$

Since τ_{ij} is unknown, the last term of equation 1.8 is unclosed and modeling is needed. A common approach is to assume that the energy transfer from resolved to subgrid scales is analogous to molecular diffusion. This gives

$$\tau_{ij} - \frac{1}{3}\tau_{kk}\delta_{ij} = -\nu_{sgs}\left(\frac{\partial \tilde{u}_i}{\partial x_j} + \frac{\partial \tilde{u}_j}{\partial x_i}\right) = -2\nu_{sgs}\tilde{S}_{ij} \tag{1.11}$$

where $\tilde{S}_{ij}$ is the rate of strain tensor of the resolved scales and ν_{sgs} is the subgrid viscosity, also called eddy viscosity [29]. A widely used subgrid model is the Smagorinsky eddy viscosity model as proposed by Smagorinsky [87]. The eddy viscosity is computed from

$$\nu_{sgs} = (C_s\Delta)^2\sqrt{(2\left|\tilde{S}\right|^2)}. \tag{1.12}$$

where C_s is a model constant and Δ is the filter width.

Also LES is far from being a closed chapter of research and there is still much research going on to improve the method. Potential areas of improvement are subgrid models, near-wall treatment, grid requirements and transitional flows, to mention a few.

The advantages of CFD as a tool to study turbulence are many. Because computer power is becoming relatively less and less expensive, CFD is the cheaper alternative to experiments in many cases. CFD can provide knowledge about all flow variables in the whole domain and input parameters are easily varied. The work to develop and improve CFD models is therefore essential for expanding our knowledge of turbulent flows. The rapid development of CFD methods combined with increasing computer power availability expanding the range of applications for CFD, raises the need of validation studies in order to assess the reliability and applicability of the methods. After all, the simulations are of no use if we cannot trust the results. It is clear that the more in-depth we wish to use the simulation results, the more detailed the validation process needs to be. The field measurements of PIV and PLIF provides an excellent basis for in-depth validation. Comparing simulation results to PIV/PLIF data can teach us much more than when comparing to one-point measurements or qualitative measurements as

is commonly done. However, remarkably few detailed validation studies of complex turbulent flow simulations have been reported.

1.1.4 Aim of this work

In this work several complex turbulent flows in models of chemical reactors are investigated by PIV/PLIF and CFD. A turbulent confined wake flow and a turbulent jet with co-flow at Reynolds numbers up to 50,000 are studied. These shear flows are of relevance to chemical process industry as they represent commonly employed ways of bringing fluids together. The turbulent transport processes in these flows have been studied by LES with passive scalar transport and simultaneous PIV/PLIF data. In addition, the turbulent flow in a scale-up model of a four-inlet vortex reactor is studied. The flow is studied by use of RANS and stereo-PIV. The study is of direct interest for users of this particular reactor design, but the swirling flow feature seen in this reactor is also found in other applications and the study is therefore of wider interest. The aim of this work is to gain understanding about the turbulent mixing processes and the reactor performances that will aid future reactor design and optimization.

Through in-depth comparison of the simulation results to the experimental data, a second goal is to extract as much knowledge and experience as possible about the CFD methods. Important topics to investigate are applicability of different CFD methods, effect of simulation parameters, and limitations to the methods. The hope is that the lessons learned can contribute to improved methods and best practices for CFD as well as provide greater confidence in simulation results. This will benefit users of CFD both in research and industry.

1.2 Dissertation organization

The remainder of this thesis is organized as follows: Chapter 2 presents a LES study of a turbulent confined wake flow where the effect of simulation parameters and in particular the effect of LES inlet conditions are examined by comparing the simulation results to PIV data. In Chapter 3 the findings in Chapter 2 are made use of in order to simulate the transport of a passive scalar in the turbulent confined wake by LES. The simulation results are evaluated in detail by comparison to simultaneous PIV/PLIF data. A study of passive scalar transport in a turbulent confined jet with co-flow by use of LES and comparison to simultaneous PIV/PLIF data is described in Chapter 4. Chapter 5 takes a closer look at the cross-gradient transport mechanisms in the jet by examining simultaneous PIV/PLIF data at two Reynolds numbers and LES results. In Chapter 6 RANS and stereo-PIV are employed to study the flow in a four-inlet vortex reactor. Finally, summary and conclusions are given in Chapter 7.

CHAPTER 2. EFFECT OF INLET CONDITIONS ON THE ACCURACY OF LARGE EDDY SIMULATIONS OF A TURBULENT RECTANGULAR WAKE

This chapter is modified from a paper accepted by

Chemical Engineering Journal

Katrine M. Nilsen[1], Bo Kong, Rodney O. Fox,

James C. Hill and Michael G. Olsen[2]

Abstract

A large eddy simulation (LES) study was performed on a turbulent incompressible wake flow in a rectangular channel. The simulation results were evaluated using particle image velocimetry (PIV) data from a previous experimental study of the same flow [61]. Comparisons were made of one-point statistics as well as spatial correlations. An extensive pre-simulation study was carried out in which the effect of inlet conditions, grid resolution, time step and subgrid model was investigated and the parameters were optimized. Using the digital filter method of Klein et al. [50], turbulent inflow velocities were generated based on velocity mean and variance obtained from the experimental data and correlation length scales. It was found that the simulation results in large parts of the domain were strongly dependent on the inlet

[1]Primary researcher and author

[2]Corresponding author

length scales specified. With a suitable set of length scales, the inlet method was successful at providing inlet conditions that generated accurate simulation results. The very good agreement seen between experiment and simulation demonstrates LES as a method that, with carefully selected inlet conditions, not only can predict the pointwise turbulence statistics of a liquid wake flow, but also capture key features of its large-scale turbulent structures.

2.1 Introduction

The wake is together with the jet and the mixing layer a commonly studied free shear flow. A wake is generated when a fluid flows over a body leaving a region of velocity deficit behind the body. The study of the turbulent wake is not only important for gaining understanding of turbulence, but also relevant in many engineering applications, such as aviation industry, chemical process industry and wind power engineering. In this context, and in the study of turbulent flows in general, computational fluid dynamics (CFD) has for many years been an important tool [80, 90].

Common wake configurations are wake behind a bluff body [52, 14, 73] and wake behind a flat plate [31]. An incompressible confined rectangular wake has been studied experimentally by Liu et al. [61] and Feng et al. [24] who employed particle image velocimetry (PIV) and planar laser-induced fluorescence (PLIF) to measure instantaneous velocity and concentration fields in the wake, and studied in particular the mixing of a passive scalar. Liu et al. [61] simulated the confined rectangular wake flow using Reynolds-averaged Navier Stokes (RANS) method and compared the result to the experimental data with good agreement. Although RANS is a cost-effective numerical method, it has limitations in that instantaneous structures of the flow cannot be captured. Large eddy simulation (LES) is a computational method that aims to solve the transient Navier-Stokes equations for the larger energy containing scales of a flow directly

while modeling the smaller dissipative scales. Thus LES can provide very detailed flow information for turbulent scales down to the smallest resolved scale. LES is therefore the preferred alternative in many situations. In this work the confined rectangular wake is simulated using LES and PIV data are used for detailed assessment.

PIV is a non-intrusive method to measure instantaneous velocity fields [1]. The fluid is seeded with light scattering particles with small enough Stokes number that they accurately follow the flow. The flow is illuminated by a pulsating laser sheet, and a camera is used to capture images of the particles for each laser pulse. A correlation technique is used to determine the displacement of the particles for each picture pair. Thus PIV provides instantaneous two-dimensional velocity fields that are excellent for validation of CFD methods and offers the possibility of comparisons on a high level including spatial structure information.

In terms of complexity, the flow investigated lies between the simple flow configurations that are commonly used for testing and validation of CFD and the highly complex flow cases found in industry where only limited experimental data are available. Thus a successful utilization of CFD methods for this flow contributes to wider applicability and higher reliability of the methods.

A challenge in LES is setting the inlet condition. Large eddy simulation requires a turbulent inlet condition that ensures the right distribution of kinetic energy as well as coherence of the fluctuations [82]. For dissipative flows where little turbulence is generated inside the domain the result will heavily depend on the inlet condition specified. The traditional way of generating turbulent inflow velocities is to superimpose random fluctuations on a specified mean velocity. This method is easy to implement, but the drawback is that it produces uncorrelated inflow velocities and an improper energy spectrum. This causes the inflow turbulence to decay rapidly when entering the solution domain [94, 64]. When the geometry allows for it, the inlet values can be obtained by applying a periodic boundary condition or by performing a precursor simulation of the

region upstream of the inlet. To limit the extra computational cost of a precursor simulation, Li et al. [58] used a finite time series of the precursor simulation and recycled through the values to get continuous inflow. In cases where sufficiently detailed experimental values are available, the inlet condition can be based on these, as in the digital filter method of Klein et al. [50] where turbulent inlet conditions with specified first and second order statistics are generated. Unless the experimental data are of such resolution both in time and space that they can be used directly as inflow condition in LES, inflow generation necessarily includes modeling and assumptions. It is therefore highly important to evaluate the turbulent inlet condition employed. This should be done not only by looking at the generated inflow velocities themselves but also by assessing how they perform in a simulation by evaluating the simulation results that are obtained using the inflow velocities. In this work the geometry does not allow for periodic boundary conditions or precursor simulation. Instead, inlet velocities were generated using the digital filter method of Klein et al. [50] and PIV data from Liu et al. [61] and the performance of the method in a simulation as well as the sensitivity to the input parameters were investigated.

Another challenge in LES lies in modeling the effect of the unresolved scales. Many subgrid models have been suggested, defined in spectral space, see e.g. [11], or physical space. Examples of the latter are the Smagorinsky model [87],the one-equation model [69, 100, 42] and the structure function model [67]. Further information regarding subgrid models can be found in e.g. [57],[28] and [82]. Even for simple flows, the performance of the subgrid models can vary greatly depending on the flow and modeling parameters. For example, Fureby et al. [28] compared different subgrid models in simulation of forced and decaying homogeneous isotropic turbulence and found that the difference in performance of the different subgrid models was dependent on the Reynolds number of the flow and the grid resolution.

Considering the challenges in LES it becomes clear that some form of validation of

the entire simulation method is required. When evaluation of LES is based on direct numerical simulation (DNS) values, the same inlet conditions can be used in the LES simulations. In addition, DNS offers the advantage of fully resolved data that can be taken as the exact solution. A comparison with DNS values is therefore quite straightforward. However, DNS data are not readily available for complex flows. Validation using DNS data is limited to demonstrating how well LES performs on flows where DNS is already feasible [96]. Thus this approach has limited use.

Evaluation of LES results by comparison to experimental data widens the range of applicable flows since experiments can be performed on flows too complex for DNS. When comparing LES results to experimental values there are several aspects that must be considered. First, experimentally measured values are averaged values over a probe volume and thus are effectively filtered values [77]. LES gives the filtered field, and since an experiment essentially also gives filtered results, one might conclude that when the two filter sizes match, the comparison can be carried out directly. However, useful definitions for filter size are lacking both for LES and for experiments [49]. Moreover, comparison with experimental values requires a simulation inlet condition that corresponds to the inlet of the experimental flow. It is then clear that the assessment of LES is closely related to evaluating the inlet condition.

In the context of evaluation by comparison the question of what values to compare arises. Intuitive first choices are mean and variance. However, since LES provides detailed full field transient flow data, the comparisons can also include comparisons of temporal and spatial correlations, higher order statistical moments, and distribution functions [2, 49, 51].

In this work OpenFOAM (Open Field Operation and Manipulation)[63], an open source software package for CFD, was used to perform the simulations. OpenFOAM offers a wide range of CFD tools and is rapidly growing in use. A successful demonstration of this software package is therefore of great interest to many, both in research and in

industry.

In the following section the flow geometry will be presented followed by a detailed description of the numerical method used to simulate the flow in the experiment. The results and comparisons are presented and discussed in part 2.4. Finally, a summary is given and conclusions are drawn in section 2.5.

2.2 Experimental Setup

Figure 2.1 shows the test section used in the experiments. The test section is a rectangular channel having a cross-section measuring 6 cm by 10 cm and a length of one meter. The channel has three inlets separated by two splitter plates so that the width of each inlet is 2 cm. This distance will in the following be noted d and used as a characteristic length for normalizing purposes. Before the fluid enters the test section it goes through flow conditioning sections consisting of a packed bed and turbulence reducing screens followed by a 16:1 contraction. The flow rate in each stream was set to 1 L/s, corresponding to a bulk velocity, U_0, of 0.5 m/s. This gives a Reynolds number based on hydraulic diameter of the channel of 37,500.

The optical setup consists of a dual-pulse New Wave Gemini Nd:YAG laser with laser light wavelength of 532 nm and a 12-bit LaVision Flowmaster 3S CCD camera with a resolution of 1280x1024 pixels. The time delay between two laser pulses were set to 700 μs and the duration of each laser pulse was about 5 ns. The image pair acquisition was at a frequency of 4 Hz and 10,000 image pairs were collected at each measurement location. The numerical aperture used was 8 and the image magnification was 0.12. The resolution of the measurements as reported in Liu et al. [61] was at the lowest 8.7 Kolmogorov length scales. Further details of the flow facility and measurement system can be found in Feng et al. [25]. The PIV data used for comparison here are taken from Liu et al. and further details of the PIV measurements in the wake can be found in [61].

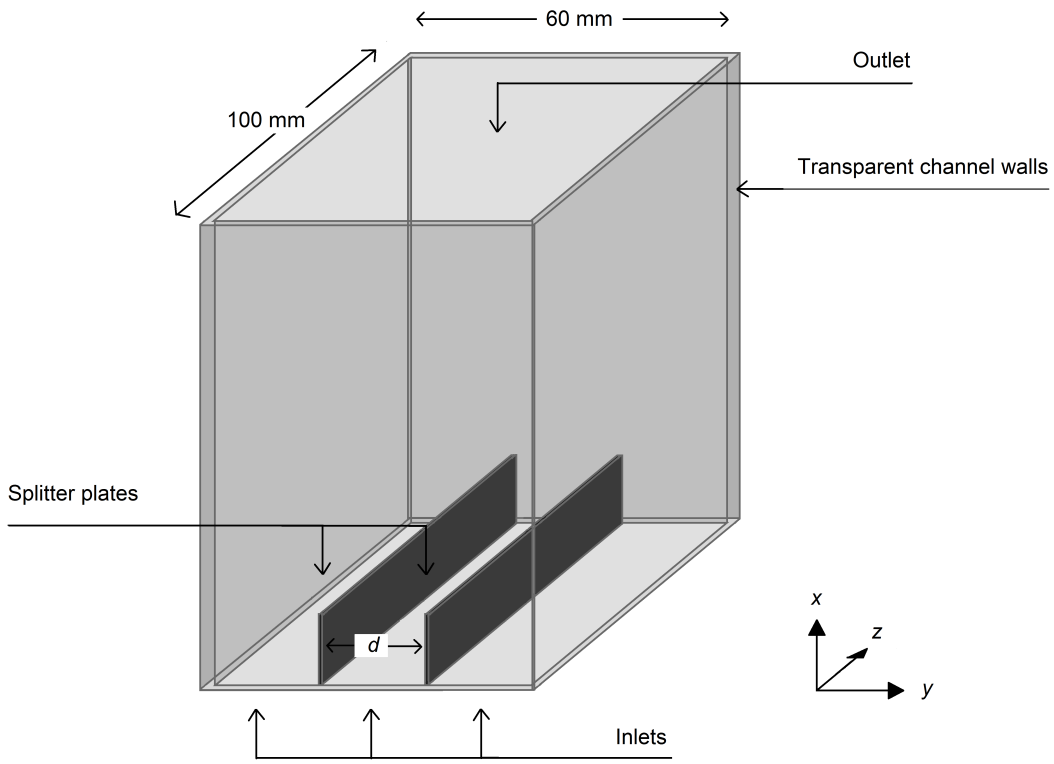

Figure 2.1: The test section.

2.3 Numerical Method

2.3.1 Large Eddy Simulation

LES is based on separation of the larger scales of the flow from the smaller scales by a filtering of the governing equations. A simple and widely used filter is the box filter which is a simple averaging within the filter length scale, $\bar{\Delta}$. This filter was chosen with a filter length scale based on the cell size of the computational grid:

$$\bar{\Delta} = (\Delta_1 \Delta_2 \Delta_3)^{1/3} \tag{2.1}$$

where Δ_1, Δ_2 and Δ_3 are the grid spacing in the x,y and z direction respectively.

The filtered Navier-Stokes and continuity equations govern the evolution of the resolved scales and take the form:

$$\frac{\partial \bar{u}_i}{\partial t} + \frac{\partial}{\partial x_j}(\bar{u}_i \bar{u}_j) = -\frac{1}{\rho}\frac{\partial \bar{p}}{\partial x_i} + \nu \frac{\partial}{\partial x_j}(\frac{\partial \bar{u}_i}{\partial x_j} + \frac{\partial \bar{u}_j}{\partial x_i}) - \frac{\partial \tau_{ij}}{\partial x_j} \tag{2.2}$$

$$\frac{\partial \bar{u}_i}{\partial x_i} = 0 \tag{2.3}$$

$(\bar{*})$ represents filtered values. u_i are components of velocity, x_i are spatial coordinates, t is time, and p is pressure. ρ and ν are the fluids density and kinematic viscosity respectively. τ_{ij} is the subgrid tensor as defined in

$$\tau_{ij} = (\overline{u_i u_j}) - \bar{u}_i \bar{u}_j \tag{2.4}$$

and is the only term that includes information from the subgrid scales. Since τ cannot be computed directly, a subgrid model is needed.

2.3.2 Subgrid modeling

Assuming that the energy transfer from the resolved to the subgrid scales is analogous to molecular diffusion gives:

$$\tau_{ij} - \frac{1}{3}\tau_{kk}\delta_{ij} = -\nu_{sgs}\left(\frac{\partial \bar{u}_i}{\partial x_j} + \frac{\partial \bar{u}_j}{\partial x_i}\right) = -2\nu_{sgs}\bar{S}_{ij} \tag{2.5}$$

where $\bar{S}_{ij}$ is the rate of strain tensor of the resolved scales and ν_{sgs} is eddy viscosity or the subgrid viscosity [29]. Models based on this hypothesis are called eddy viscosity models and this will be the approach employed in this work.

A widely used subgrid model is the Smagorinsky eddy viscosity model, proposed by Smagorinsky [87] applied to atmospheric flow calculations. This model suggests a relation between the subgrid viscosity and the filtered rate of strain tensor as

$$\nu_{sgs} = (C_s\bar{\Delta})^2\sqrt{(2\left|\bar{S}\right|^2)}. \tag{2.6}$$

C_s is a constant that takes a value between 0.1 and 0.2. The method is based on an assumption of equilibrium between energy dissipation and production in the subgrid scales. One problem with this model is that the subgrid viscosity does not automatically go to zero at the walls where there are no subgrid-scale stresses, and to compensate a damping function is normally used [82].

Another eddy viscosity model is the one-equation model. In addition to solving the described filtered governing equations, the balance equation for subgrid kinetic energy is solved. The balance equation is

$$\frac{\partial k_{sgs}}{\partial t} + \frac{\partial \bar{u}_j k_{sgs}}{\partial x_j} = -\tau_{ij}\bar{S}_{ij} - \epsilon + \frac{\partial}{\partial x_j}\left(\nu_{eff}\frac{\partial k_{sgs}}{\partial x_j}\right) \tag{2.7}$$

Here ν_{eff} represents the effective viscocity and is the sum of the molecular viscosity and the eddy viscosity. k_{sgs} represents the subgrid kinetic energy and is defined as

$$k_{sgs}(\mathbf{x},t) = \frac{1}{2}\overline{u_i'u_i'} = \frac{1}{2}\overline{(u_i(\mathbf{x},t) - \bar{u}_i(\mathbf{x},t))^2} \tag{2.8}$$

ϵ is the turbulent energy dissipation and is here modeled as

$$\epsilon = C_1\frac{k_{sgs}^{3/2}}{\bar{\Delta}} \tag{2.9}$$

The subgrid viscosity is calculated as a function of the subgrid kinetic energy:

$$\nu_{sgs}(\mathbf{x},t) = C_m\bar{\Delta}\sqrt{k_{sgs}(\mathbf{x},t)} \tag{2.10}$$

where C_m is a constant.

The dynamic eddy viscosity method was proposed by Germano [30] and later improved by Lilly [59]. The method presented by Germano calculates the constant C_s in equation 2.6 as a function of space and time based on information from the smallest resolved scales [30]. The method can be applied to other subgrid viscosity models. The approach is to apply a second filter of larger size than the original filter to the governing equations, and assume that the subgrid tensors from the first and the second filtering operations can be modeled in the same manner. A problem with this method is that it can be unstable. The usual approach to help stabilize the method is to use some kind of averaging of the flow variables in the solution.

2.3.3 Turbulent Inlet

In this work the digital filter method of Klein et al. [50] was used to generate the turbulent inlet condition. This method includes specifying first- and second-order one-point statistics at the inlet based on experimental data. The experimental data can be point-wise, but must be of high enough resolution to capture local features that are important for the flow field. In addition, the sample must be large enough for the statistics to be converged. The PIV data used in this work fulfill these requirements perfectly. The velocity at a given time and location is calculated using

$$u_i = \bar{u}_i + a_{ij} U_j. \tag{2.11}$$

Here $\bar{u}_i$ is the mean velocity based on values from the experiment and a_{ij} is

$$a_{ij} = \begin{bmatrix} \sqrt{R_{11}} & 0 & 0 \\ \frac{R_{21}}{a_{11}} & \sqrt{(R_{22} - a_{21}^2)} & 0 \\ \frac{R_{31}}{a_{11}} & \frac{(R_{32} - a_{21}a_{31})}{a_{22}} & \sqrt{(R_{33} - a_{31}^2 - a_{32}^2)} \end{bmatrix}. \tag{2.12}$$

R_{ij} is the correlation tensor of the fluctuating component of the experimentally measured velocity at the inlet given by

$$R_{ij} = \left\langle u_i' u_j' \right\rangle \tag{2.13}$$

Here and in the following $\langle * \rangle$ represents ensemble averaging. u' is calculated for each timestep and location as

$$u'(x,y) = u(x,y) - \langle u(x,y) \rangle \tag{2.14}$$

The experiment did not provide velocity data in the z-direction. Therefore assumptions had to be made. It was expected that the main coherent motion would be in the x-y-plane. $\langle v'w' \rangle$ and $\langle u'w' \rangle$ were therefore assumed negligible compared to $\langle u'v' \rangle$. $\langle w'w' \rangle$ was however assumed not negligible and set equal to $\langle v'v' \rangle$. These assumptions have no effect on the generated streamwise and cross-stream inlet velocities; only the spanwise inlet velocity is affected.

The U_j in equation 2.11 is a three-dimensional field with prescribed two-point spatial statistics generated using a random field, f, that satisfies $\bar{f}_j = 0$ and $\overline{f_i f_j} = \delta_{ij}$. A spatial filter is applied to the random field. In one dimension, it takes the form

$$U_m = \sum_{n=-N}^{N} b_n f_{m+n} \tag{2.15}$$

N is here connected to the support of the filter. In order to determine the filter coefficients b_n the autocorrelation of the filtered field

$$\frac{\overline{u_m u_{m+k}}}{\overline{u_m u_m}} = \frac{\sum_{j=-N+k}^{N} b_j b_{j+k}}{\sum_{j=-N}^{N} b_j^2} \tag{2.16}$$

is used. The autocorrelation function is assumed to take the form

$$R_{uu}(r) = e^{\left(-\pi r^2/4L^2\right)} \tag{2.17}$$

Here L is the characteristic length scale and is an input parameter, and r is the spatial variable. In extending the inlet model to three dimensions, the filters for each dimension can simply be convoluted. This means three length scales can be specified, one for each dimension. It was found that all three length scales greatly influenced the results and several initial simulations were run in order to find the optimal parameters.

In this work, the simulation inlet is a plane while the experimental data at the inlet is one-dimensional. The experimental data were extended to the whole inlet plane by

assuming constant values of mean velocity and correlation tensor components in the spanwise direction. As a consequence, wall effects from the front and back walls are not accounted for in the inlet velocities. The walls are however far enough from the center plane that this is not expected to influence the results in the plane of interest. It is important to note that this assumption does not result in constant simulation inlet velocity values in the spanwise direction.

2.3.4 Simulation Conditions

The simulated domain corresponds to the geometry of the experimental channel and has a cross-section of 6 cm by 10 cm and reaches 30 cm downstream of the inlet. The grid is uniform with hexahedron shaped cells. The filtered and closed governing equations were solved using the finite-volume method with co-located grid and Gaussian integration. OpenFOAM's PISO (Pressure Implicit with Splitting of Operators) solver was employed. The spatial scheme chosen was second order and central because of its non-diffusive properties following the findings of [68, 66] and [51]. For the convective term, linear interpolation was used to obtain cell face values of the variables that appear in the surface integral that results from Gauss' theorem. The convective term was linearized with the previous iteration value of the face flux. The cell face gradients of the diffusion term were computed by central differencing. The time scheme used was implicit and second-order backward. The boundary conditions at the walls were no-slip velocity and zero pressure gradient. At the outlet a convective outflow condition that gives zero velocity gradient whenever the velocity direction is out of the domain was used. The pressure was fixed at the outlet.

An extensive pre-simulation study was performed to optimize the model parameters. Here, grid resolution, timestep, subgrid model and inlet length scales were varied separately and the effect of each parameter was investigated. While the mean velocity was quite insensitive to the change of parameter values, the RMS of velocity was affected.

The appropriate grid size was determined by increasing the grid resolution until a further increase in grid resolution did not improve the results. Similarly, the timestep was decreased until no improvement in simulation results was seen. The Smagorinsky and the one-equation subgrid models and their respective dynamic versions were tested. Figures 2.2 and 2.3 show RMS of streamwise and cross-stream velocity respectively for the four tested subgrid models at four locations. It can be seen that the simulations using different subgrid models predicted very similar values in the center of each stream where the turbulence intensity is low and thus the subgrid scales of less importance. In the wake regions and by the walls, however, differences are seen and at location $x/d = 1$ the peak values in the wake region differ by up to 20% of the reported values. The dynamic models perform similarly well and in general better than the constant subgrid models. The dynamic Smagorinsky model was chosen based on performance and computational time consumption.

It was found that the results are quite sensitive to the inlet length scales. This finding is contrary to what was found for a jet case in the same channel as investigated by Kong et al. [51]. This is because the the wake flow is purely dissipative and thus heavily dependent on the inflow conditions, while the mean shear of the jet generates turbulence downstream of the inlet, and thus the importance of the inlet conditions is reduced.

The influence of the inlet length scales on the simulation results is quite complex, and it was seen that not only the magnitude of the length scales in each of the three directions, but also the ratio between them are important. In general, larger length scales corresponded to higher turbulence levels and turbulence that persisted longer downstream, while smaller scales corresponded to lower velocity fluctuations and turbulence that dissipated sooner. Figure 2.4 compares profiles of streamwise and cross-stream velocity RMS resulting from two simulations, one using a set of small length scales and the other using a set of larger length scales. The large length scales are approximately twice the size of the small ones. It is seen in Fig. 2.4 that using large length scales gives higher

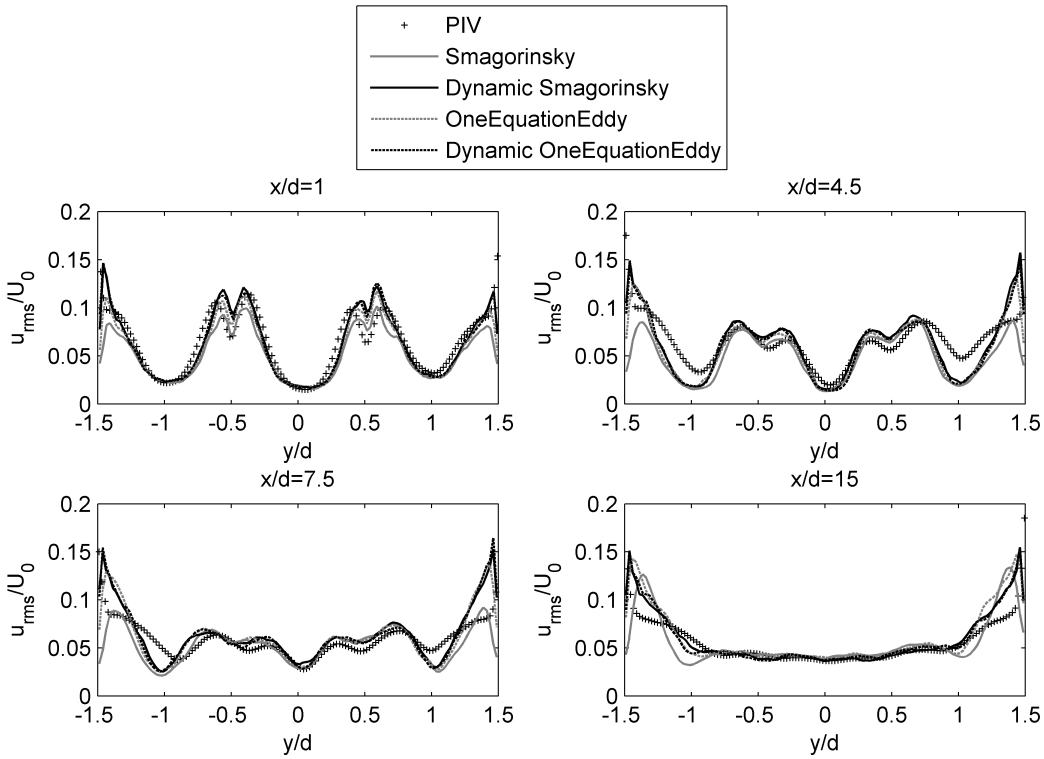

Figure 2.2: RMS of streamwise velocity component. Profiles across the channel at downstream locations $x/d = 1$, 4.5, 7.5 and 15. Symbols represent experiment values, solid lines are simulation results using the Smagorinsky model and dashed lines are simulation results using the one-equation model. Black is used for lines representing the dynamic version of the subgrid model and gray lines are used for the corresponding non-dynamic version. Values are normalized by the bulk velocity, U_0

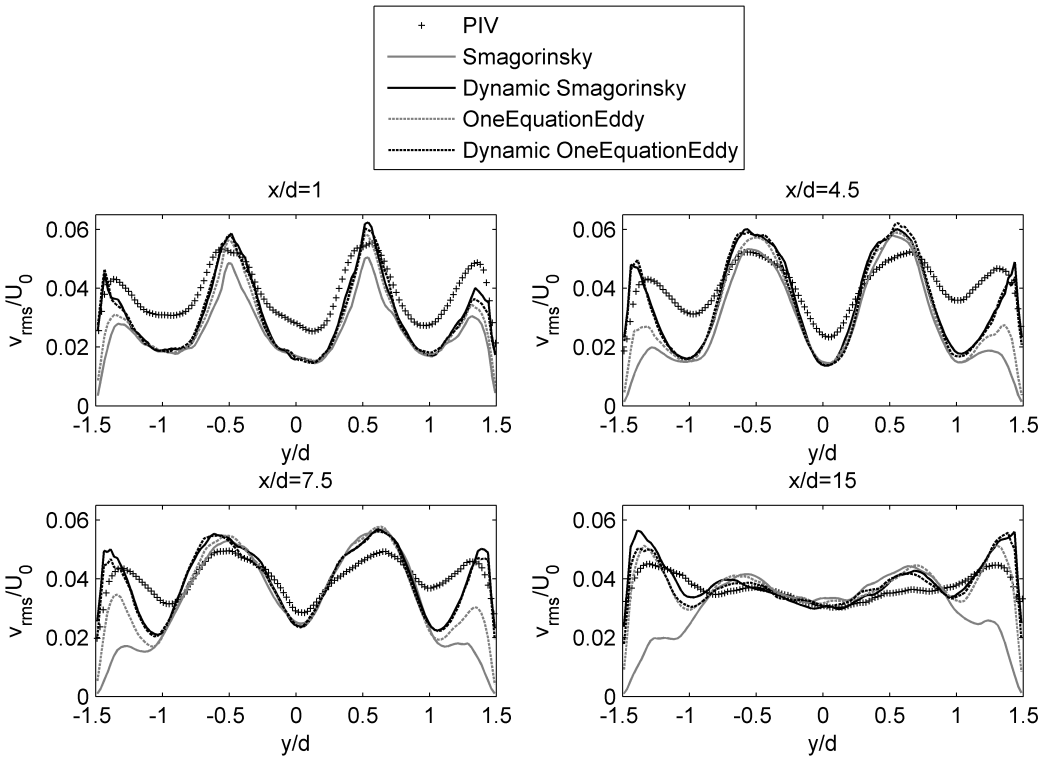

Figure 2.3: RMS of cross-stream velocity component. Profiles across the channel at downstream locations $x/d = 1$, 4.5, 7.5 and 15. Symbols represent experiment values, solid lines are simulation results using the Smagorinsky model and dashed lines are simulation results using the one-equation model. Black is used for lines representing the dynamic version of the subgrid model and gray lines are used for the corresponding non-dynamic version.

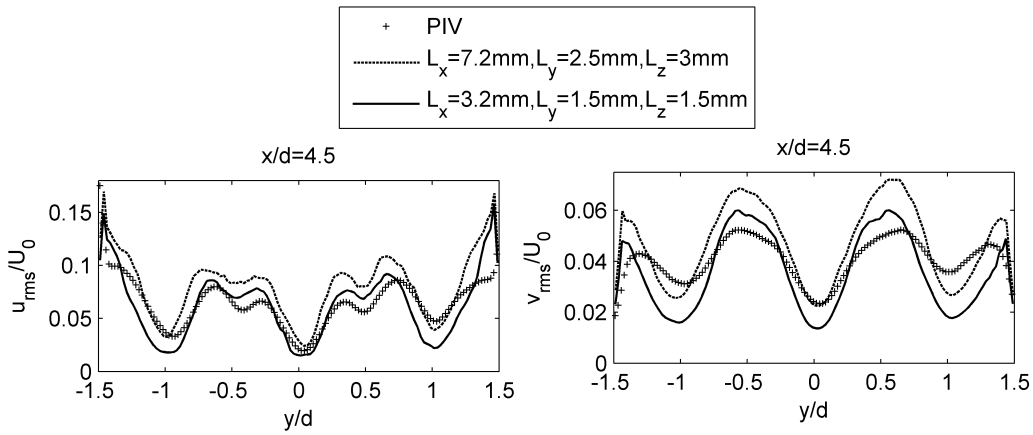

Figure 2.4: RMS of streamwise (left) and cross-stream (right) velocity component. Profiles across the channel at downstream location $x/d = 4.5$. Symbols represent experiment values, solid lines are simulation results using inlet length scales $(L_x, L_y, L_z) = (3.2, 1.5, 1.5)$mm and dashed lines are simulation results using $(L_x, L_y, L_z) = (7.2, 2.5, 3)$mm.

RMS levels than when using smaller length scales. The peak velocity RMS values in the wake region at location $x/d = 4.5$ are about 20% higher for the large length scales than for the smaller length scales. The inlet length scales can be interpreted as correlation lengths in the incoming flow and thus related to the size of coherent structures. Smaller turbulent structures can be expected to dissipate sooner than larger structures, and this is indeed reflected in the results.

It was also discovered that the different regimes of the flow field required different length scales. This is because the optimal inlet length scales are closely related to the characteristic length scale of the flow locally. Therefore two sets of length scales were specified, one set of smaller length scales for the boundary layers at the walls and at the splitter plates, and one set of larger length scales for the freely flowing centers of the inlet streams. The width of the boundary layer at the inlet was determined from the experimental profiles.

It was found that reasonable initial guesses for inlet length scales can be obtained

from PIV data using

$$L = \frac{k^{3/2}}{\epsilon} \tag{2.18}$$

where k is the turbulent kinetic energy and ϵ is the turbulent energy dissipation rate. k was estimated as

$$k = \frac{1}{2}\left(\left\langle u^2 \right\rangle + 2\left\langle v^2 \right\rangle\right) \tag{2.19}$$

and ϵ was estimated according to equation 2.21 and the discussion in section 2.4.1.4. This method also reflects the different length scales in the different regimes of the flow.

The simulation setup following the conclusions from the pre-simulations is summarized in Table 2.1. In order to let initial transients die out, the simulations were run for 5 seconds of flow time before velocity statistics were collected. The simulation was run for 80 seconds simulated time while collecting 10,000 velocity fields at a location corresponding to the measurement plane in the experiment.

Grid Type	Uniform
Grid Cell Shape	Hexahedron
Grid Cells	320x120x134
Grid Cell Size	0.9375x0.50x0.75 mm
Timestep	0.8 ms
Subgrid Model	Dynamic Smagorinsky
Solver	PISO
Time Scheme	Second Order Backwards
Spatial Scheme	Second Order Central
Inlet Method	Digital Filter
Inlet Free Stream Length Scales (L_x, L_y, L_z)	6.4 mm, 3.0 mm, 1.5 mm
Inlet Boundary Layer Length Scales (L_x, L_y, L_z)	3.2 mm, 1.5 mm, 1.5 mm

Table 2.1: Simulation Parameters

2.4 Results

The simulation results are compared to data from the experiment. Natural first choices of quantities to compare are one-point statistics of velocity as well as shear stress and turbulent energy dissipation. The two-dimensional, instantaneous nature of the

experiment data combined with the ability of LES to provide instantaneous velocity fields gives the opportunity to investigate the results more in depth by comparing spatial structure information from the simulations with the experiments. These comparisons give information about how well the turbulent structures of the flow such as vortices are captured by the simulation.

2.4.1 One-Point Comparisons

The one-point comparisons are made for profiles across the channel at six downstream locations, $x/d = 0$, 1, 4.5, 7.5, 12 and 15 as indicated in Fig. 2.5. In the following figures + represents data from the experiment, and the simulation results are presented using a solid line. It is seen for all the one-point statistics presented that at the inlet, where x/d is zero, the match between experiment and simulation is exact. This is because the simulation values at the inlet were specified from the experiment data.

2.4.1.1 Mean Velocity

Figure 2.6 shows the comparison between the simulated and measured mean streamwise velocity. Two wake regions with velocity deficiency are recognizable behind the splitter plates which are located at y/d = 0.5 and -0.5. As the flow develops the wake decays and thus the velocity profiles become flatter and approach that of a channel flow. One inlet width downstream of the inlet the agreement between simulation and experiment is quite good except for a slight discrepancy in the center of each wake. Further downstream, the simulation and the experiment profiles show excellent agreement. However, the simulation does predict slightly higher mean velocity values in the two outer streams and the velocity peaks on each side is in the simulation closer to the wall than in the experiment. The peak value overshoot is 3.7 % for the locations $x/d = 4.5$, 7.5 and 12 and 5.6 % at the most downstream location.

The difference in slope between the experimental and simulation profiles close to the

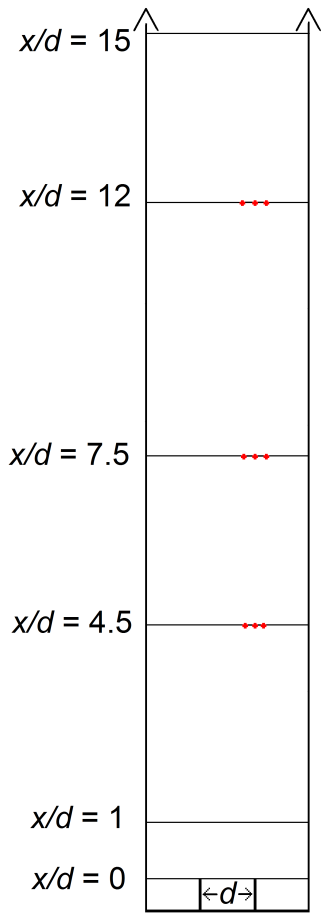

Figure 2.5: Schematic of the channel. The six cross-stream lines where one-point statistics are extracted are indicated and the nine points used for spatial velocity correlations are shown by red dots.

wall indicates that the simulation is not completely capturing the wall effect. This could be the reason for the small disagreements seen in the mean velocity profiles. All in all the profiles match well. It is important to point out that the mean profiles were not sensitive to the different parameters studied in the presimulations.

2.4.1.2 RMS of Velocity

Figures 2.7 and 2.8 display comparisons between simulation and experimental RMS profiles of streamwise and cross-stream velocity components, respectively. In Fig. 2.7 it can be seen that the RMS profile of streamwise velocity at the inlet has peak values at the splitter plate locations and at the walls. This is due to turbulence production in the boundary layers on the walls and each side of the splitter plates [79]. Correspondingly, in Fig. 2.8 the boundary layers are recognized by high RMS levels of cross-stream velocity fluctuations in regions close to the walls and splitter plates with rapidly decreasing values towards the walls and splitter plates, whose impermeable surfaces hinder cross-stream fluctuations in their vicinity and thus RMS levels must necessarily approach zero there.

It can be seen that as the flow develops, the turbulence intensities in the wake region decrease. This is due to viscous dissipation causing the wake turbulence kinetic energy to decay and the absence of mean shear in this flow to generate new turbulent eddies. Simultaneously, the RMS profiles in the wake region show a broadening trend downstream because of turbulent mixing causing transport of linear momentum and consequently the turbulent kinetic energy spreads out. Close to the walls the RMS values stay approximately constant indicating that the turbulence close to the wall mainly originates from turbulence production in the wall boundary layer and have little influence from the wake.

Overall the RMS results from the simulation agree reasonably well with the values obtained from experiment. However, there is some deviation primarily in the near wall regions and in the regions of low turbulence intensity in the centers of the streams. A common approach to improve the results by a wall is refinement of the grid towards

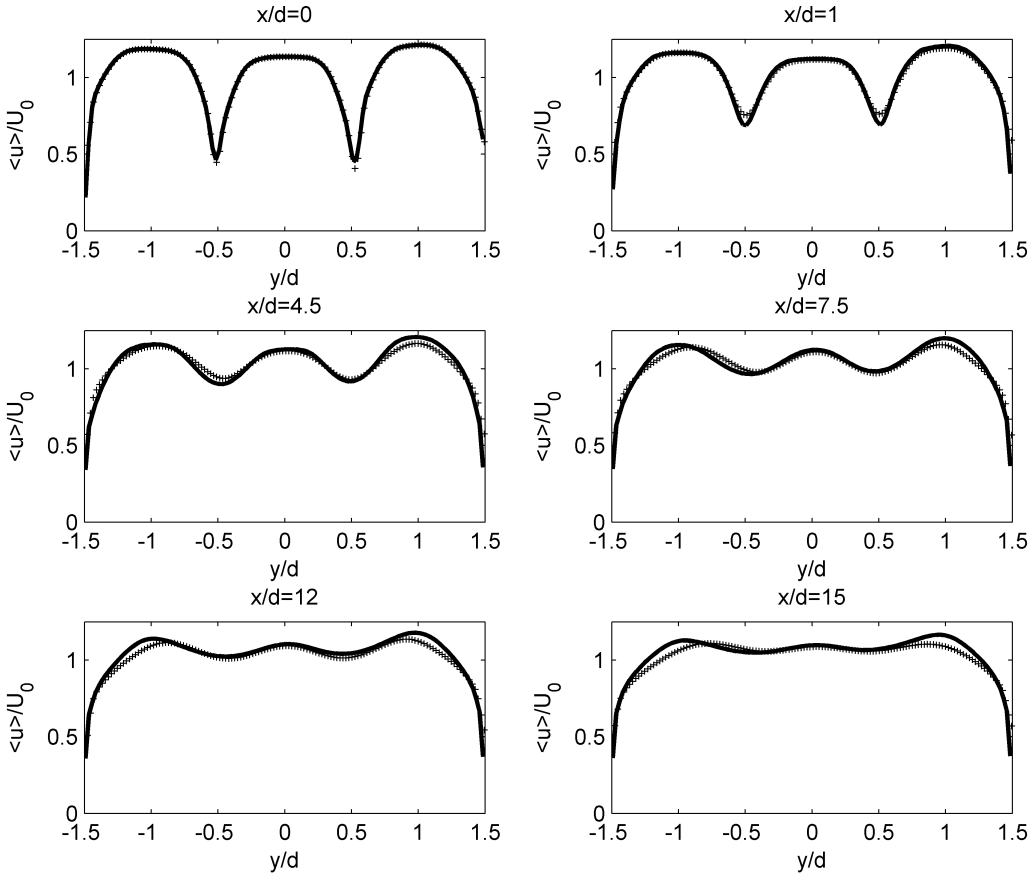

Figure 2.6: Mean velocity profiles across the channel at downstream locations $x/d =$ 0, 1, 4.5, 7.5, 12 and 15. Symbols represent experiment values and the lines are the simulation results.

the wall. However, in the presimulations it was found that a refinement of the grid did not appreciably improve the wall results. When evaluating the simulation close to the walls, it is important to notice that the PIV system is carefully adjusted to get optimal seed particle displacement in most of the channel, but that the low velocities near the walls result in seed particle displacement lower than optimal in these regions. Thus, one expects higher measurement error in the near wall regions relative to the outer streams and wakes [48]. The main interest in this work is the wake region and therefore all simulation parameters were chosen to optimize the performance of the simulation and the experiments in this region.

From the inlet to the next displayed location, $x/d = 1$, the RMS values of streamwise velocity at cross-stream locations corresponding to the splitter plate locations decrease while all other values remain unchanged. Thus downstream of the splitter plates the profiles show two peaks in each wake region. At location $x/d = 1$ the RMS of streamwise velocity fluctuations are lower behind each splitter plate in the experiment than in the simulation. It is in the regions very close to the splitter plate tips that the flow develops fastest. The disagreement between experiment and simulation there could be minimized by a refinement of the grid in this high dissipation region. The subgrid model will have a more important role here than other regions of the flow because the Kolmogorov length scales are smaller. Further downstream the match between experimental and simulation values in the wake regions is closer due to the larger dissipative scales and less reliance on the subgrid model.

The RMS of the cross-stream velocity shows relatively larger deviation from experimental values than the corresponding values for the streamwise velocity. However, since the magnitude of the cross-stream velocity as well as its RMS is smaller than the streamwise components, the absolute deviation from experimental values is actually comparable. For example, at location $x/d = 4.5$, for $y/d = 1$ the normalized deviation from experimental values is 0.2 both for streamwise and cross-stream RMS. The deviation between

simulation and experimental values is most significant in the centers of the streams. The simulated cross-stream RMS does however match the center of stream RMS of the streamwise velocity suggesting isotropic turbulence at these locations. Isotropic turbulence would also be expected since there are no shear forces in the centers of the streams. The experiments may show slightly higher cross-stream RMS than the simulations due to the smaller magnitudes of cross-stream velocity and thus a greater dependence on sub-pixel interpolation to measure these velocities.

For the farthest downstream location, the simulation prediction overshoots the experimental values along most of the cross section. A plausible explanation is that at this downstream location the wall effects begin to influence the flow near the center of the reactor. Since the LES model used here is optimized for the free shear region, and not for the near wall region, this could cause the discrepancy observed at location $x/d = 15$.

2.4.1.3 Reynolds Shear Stress

Figure 2.9 shows the Reynolds shear stress calculated from the simulation data compared with the values from experimental data. The shear stress values are positive by the right side wall and in the left side of each wake region, and negative near the left wall and in the right side of the wake regions. The shear value is close to zero in the centers of each of the three streams due to flow symmetry. It is seen from Fig. 2.9 that the simulation is able to accurately reproduce these features of the shear stress. Close to the walls there is some deviation and this follows from the disagreement seen in the RMS values of velocity.

2.4.1.4 Turbulent Energy Dissipation Rate

The turbulent energy dissipation occurs at the smallest turbulence scales. The Kolmogorov length scale is an estimate of the smallest scale of the turbulence and can be

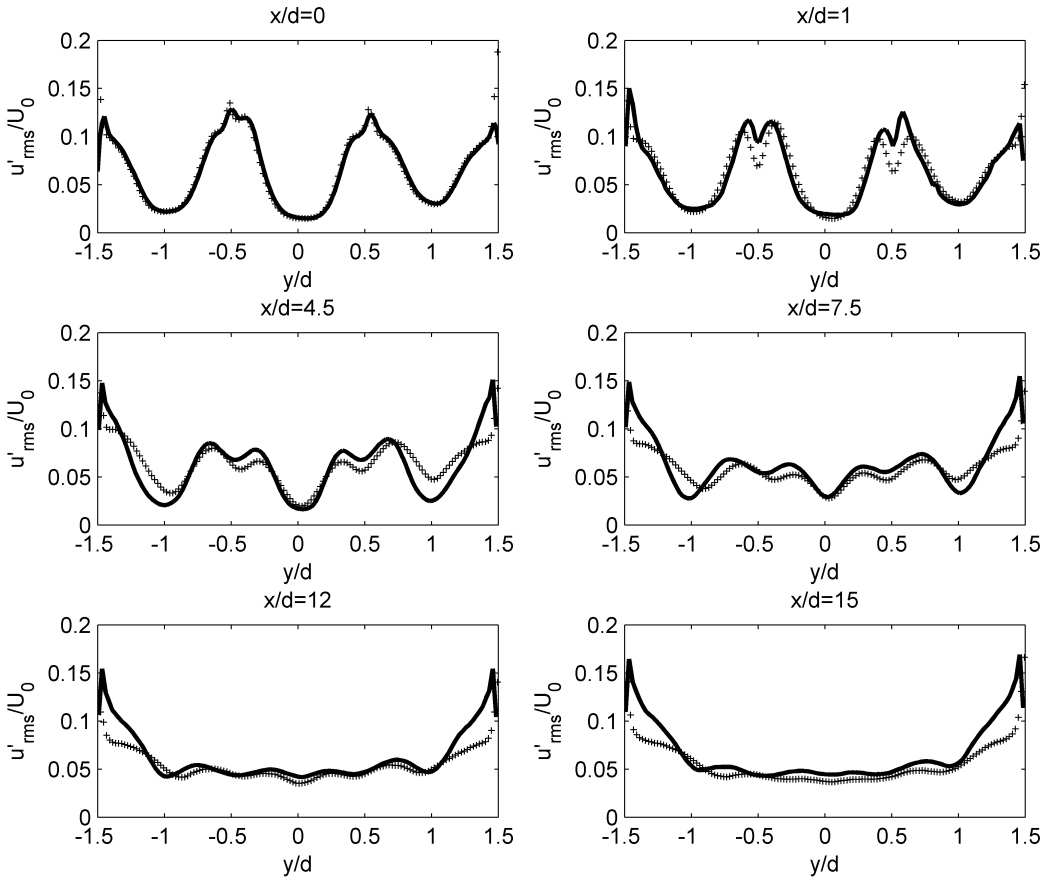

Figure 2.7: RMS of streamwise velocity component. Profiles across the channel at downstream locations $x/d = 0$, 1, 4.5, 7.5, 12 and 15. Symbols represent experiment values and lines are simulation results.

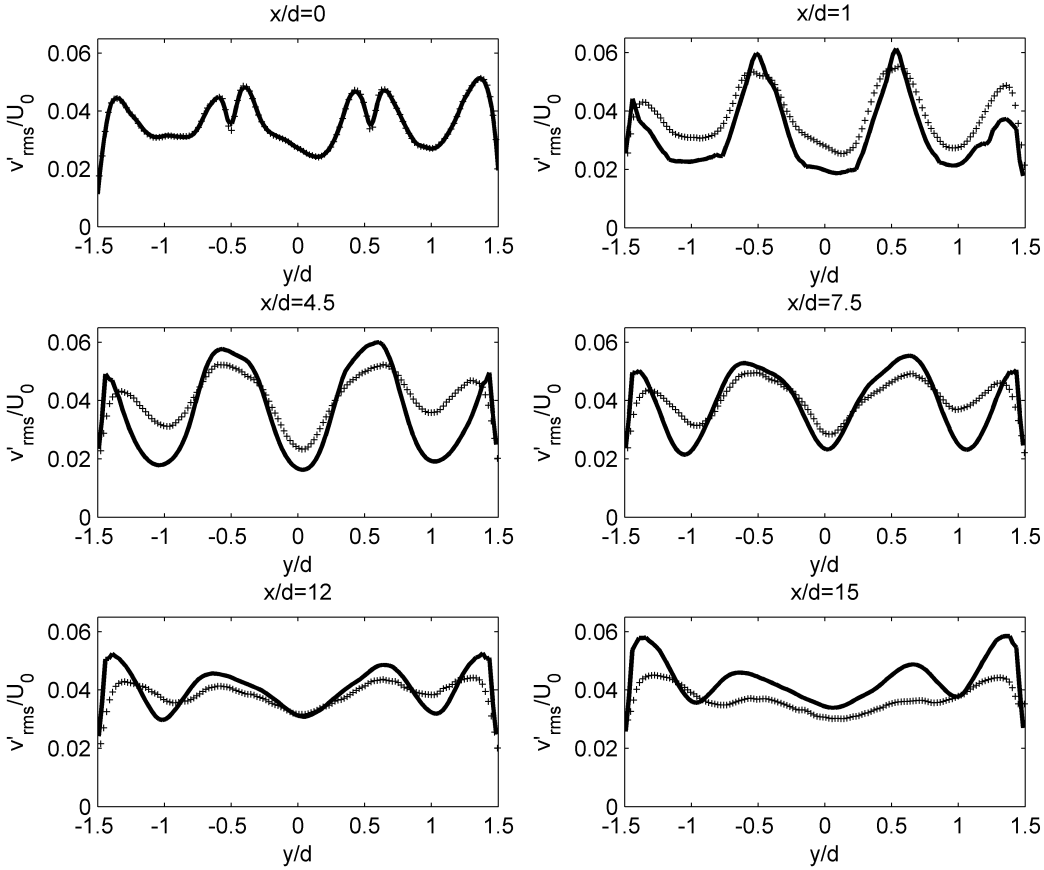

Figure 2.8: RMS of cross-stream velocity component. Profiles across the channel at downstream locations $x/d = 0$, 1, 4.5, 7.5, 12 and 15. Symbols represent experiment values and lines are simulation results.

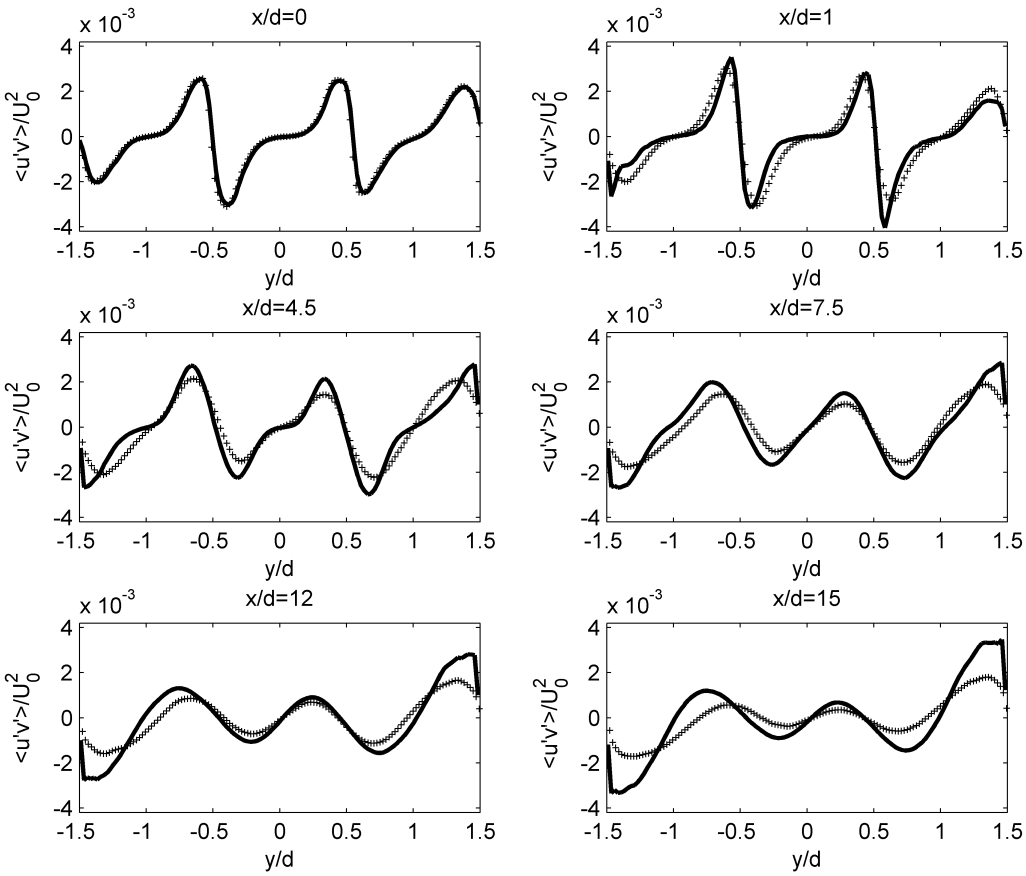

Figure 2.9: Mean shear stress, $\langle u'v' \rangle$. Profiles across the channel at downstream locations $x/d = 0$, 1, 4.5, 7.5, 12 and 15. Symbols represent experiment values and lines are simulation results.

found by

$$\eta = \left(\frac{\nu^3}{\epsilon}\right)^{1/4} \tag{2.20}$$

The turbulent energy dissipation rate, ϵ, can be estimated from

$$\begin{aligned}\epsilon \;=\; \nu \Bigg[& \overline{2\left((\frac{\partial u}{\partial x})^2 + (\frac{\partial v}{\partial y})^2 + (\frac{\partial w}{\partial z})^2\right) + (\frac{\partial u}{\partial y})^2 + (\frac{\partial u}{\partial z})^2 + (\frac{\partial v}{\partial x})^2} \\ & \overline{+(\frac{\partial v}{\partial z})^2 + (\frac{\partial w}{\partial x})^2 + (\frac{\partial w}{\partial y})^2 + 2\left(\frac{\partial u}{\partial y}\frac{\partial v}{\partial x} + \frac{\partial u}{\partial z}\frac{\partial w}{\partial x} + \frac{\partial v}{\partial z}\frac{\partial w}{\partial y}\right)}\Bigg]\end{aligned} \tag{2.21}$$

when a large part of the energy dissipating scales are resolved [83, 61]. For data of coarser resolution, a large-eddy method for estimating turbulence dissipation rate as proposed by Sheng et al. [84] can be used. Both methods were applied to the data. The PIV results showed overall agreement between the two methods of estimating dissipation, while for the LES data the large-eddy method gave a relatively large overshoot in the high dissipation regions. This indicates that the spatial resolution is such that equation 2.21 is the appropriate choice. This is further supported by the arguments of Liu et al. [61]. The presented energy dissipation results are estimated using equation 2.21.

The experimental data are two-dimensional and therefore only the four in-plane components of the velocity gradient tensor are known. A fifth component can be found using continuity. The four remaining components must be approximated. The spanwise velocity component is assumed to be close in magnitude to the cross-stream velocity component and the gradients in the spanwise direction are assumed to be similar to the gradients in the cross-stream direction. This gives the assumptions $w \approx v$ and $\frac{\partial}{\partial z} \approx \frac{\partial}{\partial y}$.

The turbulent energy dissipation rate was calculated from the simulation results using both a two-dimensional approach equal to the one used on the experiment data and a direct calculation of equation 2.21 using the three-dimensional data from the simulation.

Using the calculated energy dissipation values, the resolution of experiment and simulation can be estimated in terms of the resulting Kolmogorov length scales. The location just downstream of the splitter plates is where the turbulent energy dissipation is the

largest and thus the resolution relative to the local Kolmogorov length scale is the lowest. Here the PIV resolution is 2.7η and the LES resolution is 4.1η using the two-dimensional approach and 3.7η using the three-dimensional data. This supports the assumption that most of the energy dissipating scales are resolved. It must however be noted that the resolutions are calculated using the estimate of the energy dissipation rate and are therefore an indication that the assumption is valid rather than a confirmation.

Figure 2.10 compares the turbulent energy dissipation rate estimated using equation 2.21 for both the two-dimensional and three-dimensional simulation data compared to the estimate from the experimental data. It is seen that the energy dissipation rate is highly inhomogeneous with sharp peaks in the vicinity of the splitter plates and walls. The energy dissipation rate decays quite rapidly in the wake region. As the location of observation moves downstream, the peaks of energy dissipation rate in the wake region spread. The profiles approach the shapes of a fully developed channel flow where dissipation mainly occurs near the walls [65, 70]. Results from simulation and experiment agree very well. Also between the simulation results using the two-dimensional and three-dimensional method for estimating dissipation the results show congruence. Near the inlet the results using the three-dimensional method gives smaller values than using the two-dimensional method and the experiment values although the agreement is still good. The good agreement between the two- and three-dimensional results indicate that the assumptions made regarding the spanwise direction were valid, and the two-dimensional method provides an accurate estimation of dissipation for this flow.

2.4.2 Two-Point Statistics

The two-point spatial correlation of velocity fluctuations is the correlation between velocity fluctuations in a given point (called the basis point) and the velocity fluctuations in the field around it. The general equation is

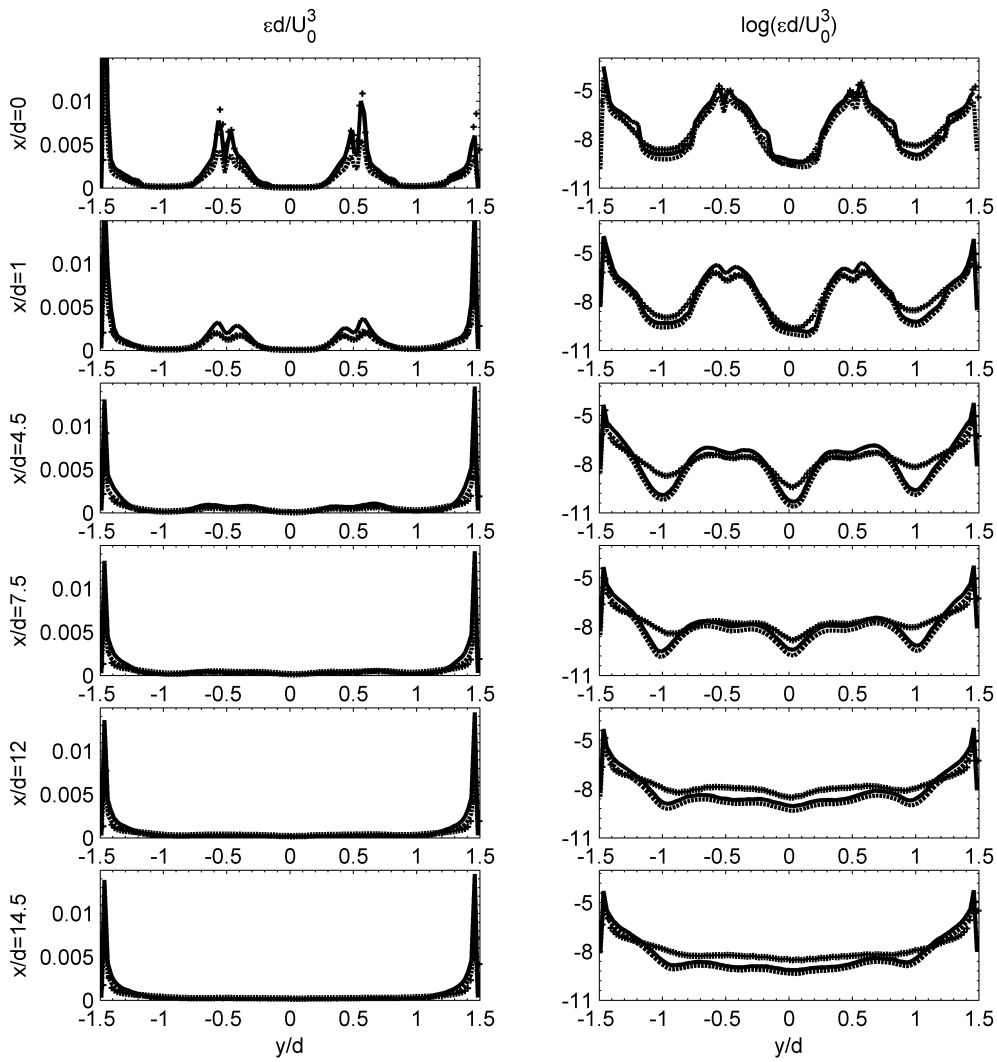

Figure 2.10: Turbulent energy dissipation rate in left column and natural logarithm of turbulent energy dissipation rate in the right column. Symbols represent PIV data, solid line is LES values using 2D-method and the dashed line is LES values using 3D data.

$$R_{u_i' u_j'}(\boldsymbol{X},\boldsymbol{x}) = \frac{\left\langle u_i'(\boldsymbol{X})\, u_j'(\boldsymbol{x})\right\rangle}{\sqrt{\langle (u_i'(\boldsymbol{X}))^2\rangle \left\langle (u_j'(\boldsymbol{x}))^2\right\rangle}} \tag{2.22}$$

Here $\boldsymbol{X}$ is the spatial coordinates of the basis points and $\boldsymbol{x}$ is the variable spatial coordinate. i can be equal to j in which case the autocorrelation is considered. When i is different from j, equation 2.22 gives the two-point cross-correlation of velocity.

The two-point correlations provide information about the dominant spatial structures of the flow in the given area. A well-known type of turbulent structure in a wake is the vortex [36, 24]. The vortices are shedded from the body and are transported downstream with the flow. The typical shedding pattern is the von Karman vortex street in which vortices are shed from alternating sides of the body with alternating direction of rotation [93, 72]. Typically, vortices are formed in the regions with high velocity gradients. Since the vortices with their swirling motion to a large extent are contributing to the transport of momentum and fluid in the flow [26], it is of great interest to be able to properly model them in the simulation. Thus validating the simulation with respect to vortices is important from a mixing perspective.

In the results presented here, the filled contours are the experiment values and the line contours are the simulation data. Two-point correlations are shown for basis points located in the wake region where the correlations were strongest. The comparisons are made at three different downstream locations, $x/d = 4.5$, 7.5 and 12. For each downstream location, contours using three different basis points are presented. One basis point is chosen in the middle of the wake, and the other two basis points are located on each side as illustrated in Fig. 2.5. Since the two wakes are similar, results are only presented for the right wake region.

Figure 2.11 shows the contours of the autocorrelation of streamwise velocity component. The correlation values are high close to the correlation point as is expected for autocorrelations. The region of positive values around the correlation point indicates

where the velocity can be expected to behave similarly as the velocity in the correlation point. Thus the size of the correlation areas gives an indication as to the typical size of coherent structures at that location.

At location $x/d = 4.5$ which is the location closest to the inlet, the experimental data give low level contours that are stretched in the streamwise direction. The simulation results do not give this stretched tendency in the low level contours. The most likely explanation for this discrepancy is that there are some weak large scale dynamics in the experimental inflow that the inlet method was not able to transfer to the simulation. As the flow develops, these low level streamwise correlation contours in the experiment decrease in size yielding very good agreement between simulation and experiment at the further downstream locations.

The basis points on either side in the wake give a negatively correlated region next to the positive region on the side towards the center of the wake for all downstream locations. The further downstream, the clearer this negative region is. A negatively correlated region implies that the velocity in this region is likely to increase when the velocity in the correlation point is decreasing and vice versa. A vortex will give a positive contribution to the streamwise velocity at one side and negative contribution on the other side of the vortex. Thus the negatively correlated region can be seen as a sign of swirling motion. The fact that the simulation is able to reproduce these negative regions is a good indicator that the coherent structures in the wake are captured by the simulation and closely resemble the structures observed in the experiments.

Figure 2.12 shows the corresponding autocorrelation contours for the cross-stream velocity fluctuations. Again the correlation is high close to the basis point. There are negatively correlated regions both upstream and downstream of the correlation point and they are seen for all three cross-stream locations of correlation points. While a swirling motion will result in negative areas of correlation to the sides of the main correlation area in the streamwise autocorrelations, the correlations of cross-stream velocity fluctuations

will correspondingly give negatively areas of correlations up- and downstream of the main correlation area. Therefore negatively correlated regions are yet another indicator of swirling motion being dominant in the wake and a further indication that the structures in the simulation closely resemble the structures observed in the experiment.

The correlation contours appear as "crescent" moon shapes with tips stretching upstream of the basis point on each side of the basis point. This is explained by the lower velocity in the wake than in the free stream on each side of the wake. The mentioned trends as well as the size and strength of the correlation areas are very well captured by the simulation.

The two-point cross-correlation between streamwise velocity fluctuation at the basis point with cross-stream velocity fluctuations in the field is shown in Fig. 2.13. For the left basis point the main correlation region is positive for all downstream locations while for the right-hand side basis point it is negative. This gives information about the preferred direction of rotation in each side of the wake. The swirling is so that the fluid is brought into the wake region downstream of the swirling center and out of the wake region upstream of the center. The correlation contours for the basis point in the center of the wake are very weak, both in the experiment and the simulation. This indicates that there is no preferred direction of rotation in the very center of the wake. These findings agree with the vortex shedding pattern commonly seen in wake flows.

Upstream and downstream of the main correlation regions on either side oppositely correlated regions can be seen. These regions further support the interpretation of swirling motion. The two secondary regions also suggest a secondary vortex as part of a vortex street. The simulation gives these secondary areas for all downstream locations, while they are not visible in the experiment contours for location $x/d = 4.5$.

The experiment gives long streamwise correlation areas for the low level contours of R_{uv} for the location $x/d = 4.5$ similarly to what was seen in Fig. 2.11. This is not captured by the simulation and the explanation for the discrepancy follows the same

reasoning as for the autocorrelation case. The simulation contours show over all good agreement with the experiment suggesting that the simulations accurately model the large-scale turbulent structure behavior.

2.5 Summary and Conclusions

A large eddy simulation study was performed on a turbulent incompressible wake flow in a rectangular channel. The same flow has previously been investigated experimentally using particle image velocimetry to obtain velocity field data from the spanwise center plane of the channel [61]. The PIV data were used to evaluate the results by comparing one-point statistics as well as spatial correlations between simulation and experiment.

The simulation proved to be strongly dependent on the inlet condition. The digital filter method of Klein et al. [50] was employed to generate turbulent inflow conditions with the same mean and variance as the experiment data at the inlet. It was found that the simulation results in large parts of the domain depended heavily on the inlet length scales specified. With a suitable set of length scales, the inlet method was successful and proved to be a flexible and good choice of method.

The simulation results compared very well to the experimental data. Comparisons of one-point statistics across the channel at six different locations were made and the simulation proved able to reproduce mean velocity values as well as the fluctuating velocity components and shear stress in the flow. Estimations of turbulent energy dissipation rate showed good agreement between simulation and experiment.

Two-point velocity correlations also showed a good match between experiment and simulation. Agreement in size, shape, orientation and growth for both auto- and cross-correlations shows that the simulation effectively captures the dominant turbulent structures of the flow. The good agreement seen between experiment and simulation demonstrates LES as a method that, with carefully selected inlet conditions, can reproduce not

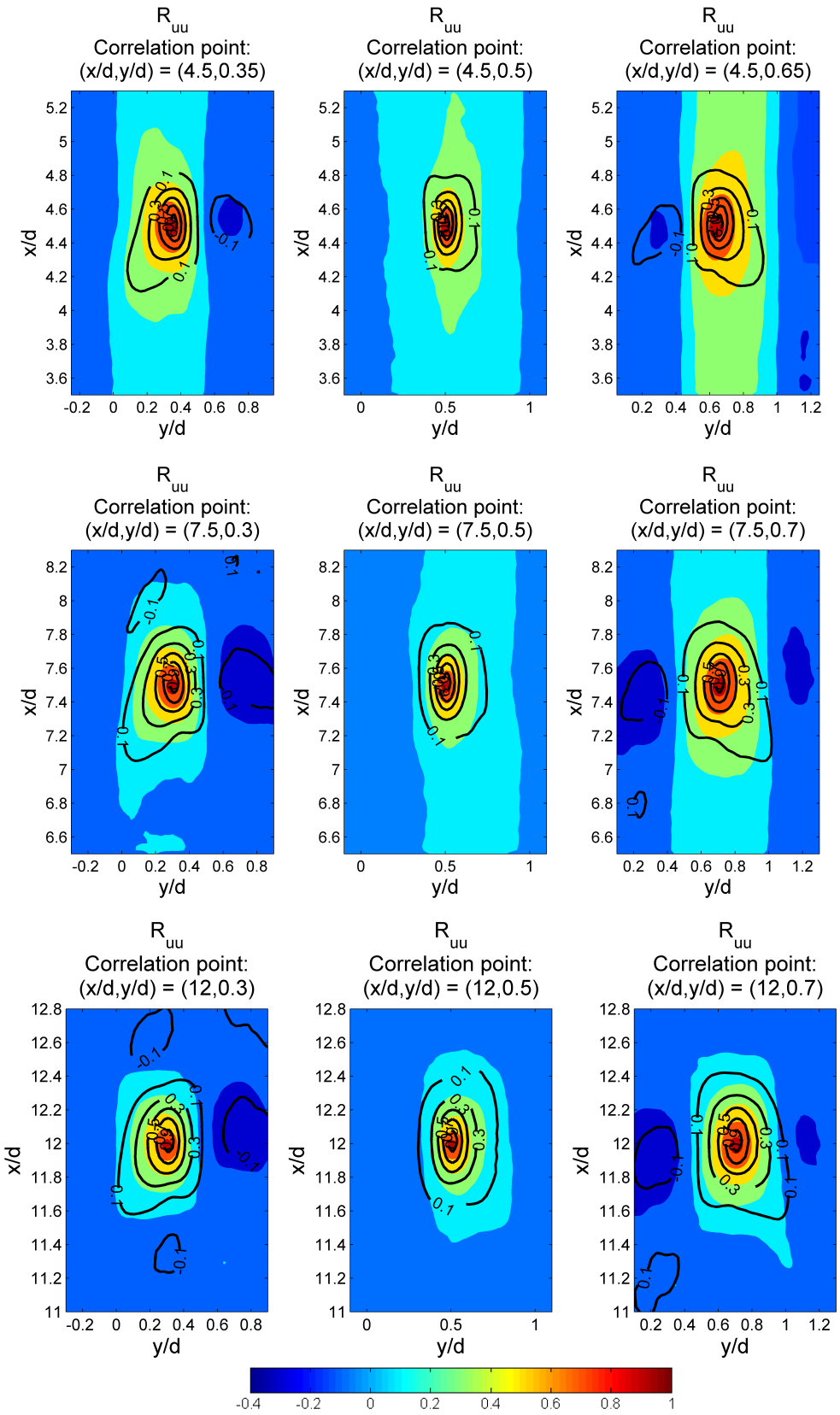

Figure 2.11: Two-point autocorrelation of streamwise velocity.

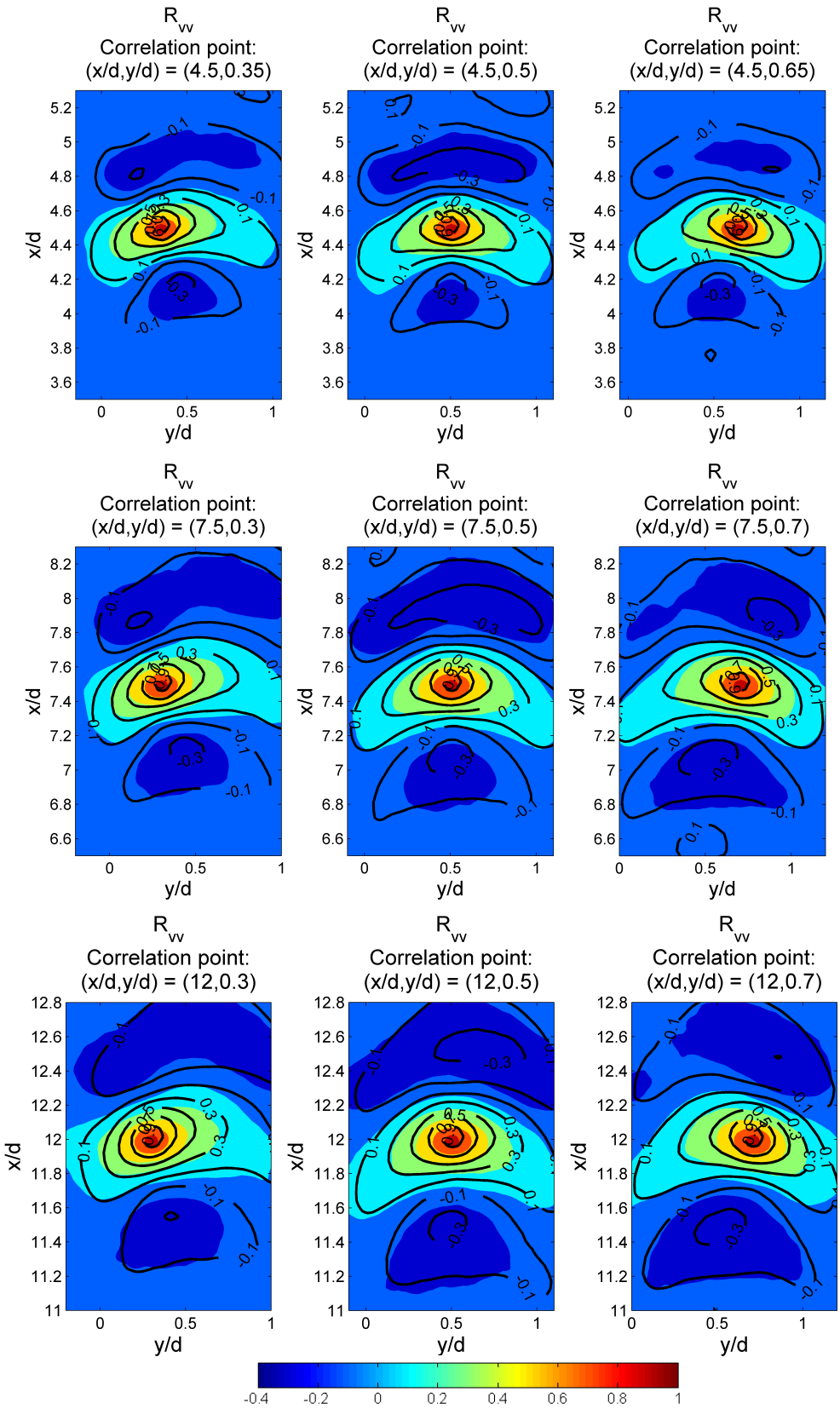

Figure 2.12: Two-point autocorrelation of cross-stream velocity.

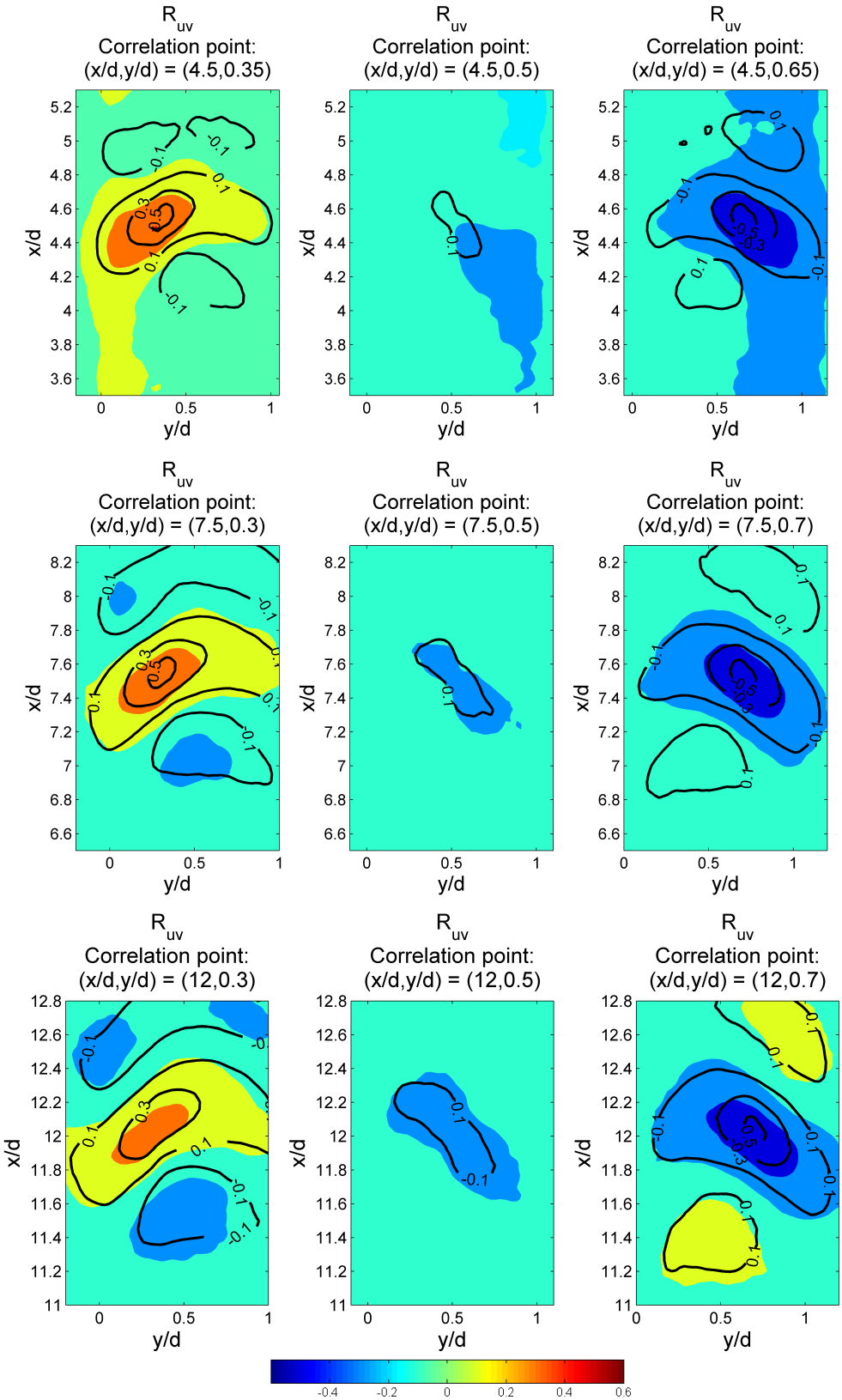

Figure 2.13: Two-point cross-correlation of streamwise velocity in correlation point with cross-stream velocity.

only the pointwise turbulence statistics of a wake flow, but also capture key features of the large-scale turbulent structures of the flow. LES therefore has the potential to be a tool that can be used in the study of mixing in wake flows.

CHAPTER 3. LARGE EDDY SIMULATION OF PASSIVE SCALAR TRANSPORT IN A TURBULENT INCOMPRESSIBLE WAKE -COMPARISON TO SIMULTANEOUS PIV/PLIF

A paper in preparation

Katrine M. Nilsen[1], Bo Kong, Rodney O. Fox,

James C. Hill and Michael G. Olsen[2]

Abstract

Large eddy simulation of the passive scalar transport in a turbulent confined wake flow was performed. The results were evaluated by comparison to experimental data from Feng et al. [24].

The gradient diffusion hypothesis was used to close the transport equation for the passive scalar. Different discretization schemes were tested in order to determine the best choice for ensuring boundedness of the passive scalar and to predict the right mixing rate.

The simulation results were compared in-depth to the simultaneous whole-field velocity and concentration data measured by Feng et al. The evaluation includes comparison of one-point statistics such as mean and variance of the passive scalar. The nature of the

[1]Primary researcher and author

[2]Corresponding author

experimental data enabled comparison of turbulent fluxes and turbulent diffusivity. In addition, two-point spatial correlations of concentration and velocity were computed from simulation and experiment and compared.

The simulation results compares well to the experimental data.

3.1 Introduction

The prediction of passive scalar transport in turbulent flows is of great importance in a wide range of applications. Turbulent mixing is relevant in for example process industry where reactants are mixed by turbulence, in dispersion of pollutants in the atmosphere or waters and in combustion applications. The accurate prediction of the transport of the passive scalar is beneficial in that it limits the need of costly experiments, both in design situations and for research purposes.

However, prediction of turbulent transport of a passive scalar is a challenging task. This arrives from the wide range of scales present in turbulent flows. A solution to the governing equations requires high level of computer power. For cases where the Schmidt number is large, the smallest scale of the passive scalar will be much smaller than the smallest scale of turbulence. Then, the presence of a passive scalar widens the range of scales and increases the computational demand.

Given the high complexity and the high computational demand, it is clear that simulation of turbulent passive scalar transport in most cases calls for modeling. With modeling, the need to evaluate the assumptions made and validate the results arises. Commonly, simulations are validated using relatively simple measurement data, such as point-wise velocity, pressure or concentration data. Examples of this can be found in [35, 37, 54, 81]. Although such data can give indications to whether the simulation is reliable or not, they give little information as to why or why not. For that, more detailed information is needed. Particle image velocimetry (PIV) [1] and planar laser-induced flu-

orescence (PLIF) are two non-intrusive full-field measurement techniques. A combined system of simultaneous PIV/PLIF offers a unique opportunity to evaluate simulation of passive scalar transport in-depth. Simultaneous PIV/PLIF provides measurement data of velocity and concentration simultaneously and in a whole field [7, 44]. Thus, both turbulent fluxes and spatial gradients can be obtained, key values in the prediction of turbulent transport. In addition, spatial information such as spatial correlations can be computed and gives valuable information about the turbulent coherent motion in the flow, which is a key feature in the transport of a passive scalar.

The two main branches of modeling of turbulent flows are Reynolds-averaged Navier-Stokes (RANS) and large-eddy simulation (LES). In RANS the governing equations are averaged and the mean values are solved for while the effect of turbulence is modeled. In LES a filtering is applied to the governing equations and only the large scales of the flow are solved for while the effect of the smaller scales is modeled. Equation 3.1 is a generic equation for the transport of a passive scalar in a turbulent flow.

$$\frac{\partial \tilde{\phi}}{\partial t} + \tilde{u}_i \frac{\partial \tilde{\phi}}{\partial x_i} = \Gamma \frac{\partial}{\partial x_i} \left(\frac{\partial \tilde{\phi}}{\partial x_i} \right) - \frac{\partial \lambda_i}{\partial x_i} \tag{3.1}$$

Here and in the following ϕ is the concentration of the passive scalar, u_i are the components of velocity, x_i are spatial coordinates and Γ is the molecular diffusivity. Tilde represents Reynolds averaging in the case of RANS and filtering in the case of LES. λ_i is the turbulent flux, or, in the LES framework, the subgrid scalar flux. It contains the unclosed terms and therefore requires modeling. The most common way of modeling is to invoke the gradient diffusion hypothesis which states that the turbulent flux is aligned with and proportional to the gradient of the scalar concentration.

$$\lambda_i = -\Gamma_T \frac{\partial \tilde{\phi}}{\partial x_i} \tag{3.2}$$

Here, Γ_T is the turbulent diffusivity or the eddy diffusivity. It is related to the turbulent viscosity or eddy viscosity, ν_T, through

$$Sc_T = \nu_T / \Gamma_T \tag{3.3}$$

where Sc_T is the turbulent Schmidt number and is often assumed to be constant.

Literature shows several examples of cases where the gradient diffusion hypothesis with a scalar turbulent diffusivity in the RANS framework does not hold. Tavoularis and Corrsin [91] and Lemoine et al. [56] studied a nearly homogeneous turbulent shear flow with a uniform mean temperature gradient and a circular heated jet with co-flow, respectively. In both cases it was found that the turbulent flux was not aligned with the mean temperature gradient.

Feng et al. [24] performed simultaneous PIV/PLIF in a confined turbulent wake flow at Reynolds number 37 500. A RANS simulation by Liu et al. [61] of the same flow showed some discrepancy in the mixing rate of the passive scalar. In this work the wake flow is simulated by LES with passive scalar transport and the results are compared in-depth to the PIV/PLIF data of Feng et al. The aim is to evaluate the method beyond the ordinary one-point comparisons and to expand on the universality and applicability of the gradient diffusion hypothesis in the LES framework.

3.2 Experimental Setup

The experimental data are reported by Feng et al. [24]. The main features of the experimental method are repeated here for reference.

3.2.1 Flow facility

The test section is a rectangular channel of cross section 100 mm by 60 mm and a length of 1 m. The working fluid is water. The test section is fed by three inlet streams, divided by two splitter plates, as seen in Figure 3.1. Each feed stream is controlled separately with an accuracy of ±0.5%. The flow rate in each stream was set to 1.0 L/s corresponding to a channel bulk velocity, U_0 of 0.5 m/s and a Reynolds number based on the bulk velocity and the channel hydraulic diameter of 37 500. Upstream of the inlet

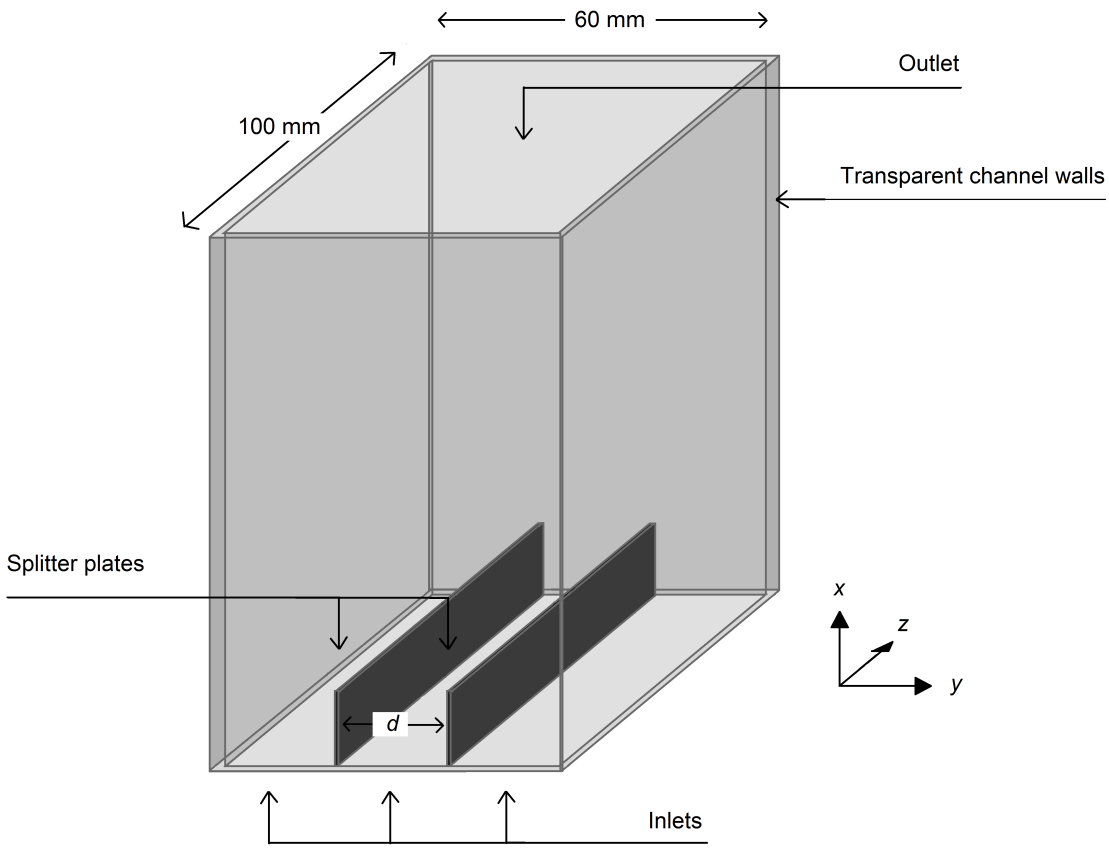

Figure 3.1: The test section

is a flow conditioning section consisting of a packed bed of spheres, turbulence reducing screens and a 1:16 contraction.

3.2.2 Simultaneous PIV/PLIF

The measurement of simultaneous velocity and concentration fields is done by combining the two laser-based techniques PIV and PLIF.

In PIV, the fluid is seeded with light scattering particles and a pulsating laser sheet is used to illuminate the flow in the plane of interest. A synchronized camera captures the scattered light from the particles for each laser pulse. Using carefully chosen time-delay between the laser pulses, the displacement of the particles from one image to the next

can be identified.

In PLIF, a fluorescent dye is added to the flow and the laser light is used to excite the dye in the measurement plane. The emitted fluorescence from the dye is recorded by a camera and the intensity of the fluorescense is related to the concentration of the dye.

Feng et al. used a New Wave Research Gemini Nd:YAG laser that provides light of wavelength 532 nm in pulses of 5 ns and a maximum pulse energy of 120 mJ. The laser light was formed into a 0.5 mm thick sheet through the spanwise center plane of the channel. The flow was seeded with hollow glass spheres with a density of 1.1 g/cm^3 and a nominal diameter of 11.7 μm. The fluorescent dye used was Rhodamine 6G which in water has a Schmidt number of 1200 [15]. The dye was added to the center stream, while the side streams did not contain dye.

Two 12-bit CCD cameras, one for PIV and one for PLIF, with a resolution of 1280x1024 pixels and an image magnification of 0.12 were used. The scattered light from the particles and the fluorescent light from the dye were separated using a dichroic mirror and directed to the respective camera. The PIV camera had a focal number of 8. The time interval between the two laser pulses was set to 700 μs. A cross-correlation technique was used to compute the velocity field from the particle image pairs. Interrogation windows of 16x16 pixels with 50% overlap gave vector spacing of 0.45 mm. The uncertainty of the velocity measurements was estimated to be 3% [61]. Through a careful calibration of the PLIF measurements, non-uniform laser intensity throughout the laser sheet was accounted for. The shot-to-shot variation of the laser intensity was found to be 2%. For the PLIF camera the focal number was 5.6. The images were captured at a rate of 1 realization per second and in total 3250 realizations were captured at each of six downstream locations.

3.3 Numerical Method

The flow was simulated by use of the large eddy simulation method in which the large, resolved scales of the flow are solved for directly while the effect of the small scales is modeled. The full set of equations equations governing the resolved scales are:

$$\frac{\partial \bar{u}_i}{\partial t} + \frac{\partial(\bar{u}_i\bar{u}_j)}{\partial x_j} = -\frac{1}{\rho}\frac{\partial \bar{p}}{\partial x_i} + \nu\frac{\partial}{\partial x_j}\left(\frac{\partial \bar{u}_i}{\partial x_j} + \frac{\partial \bar{u}_j}{\partial x_i}\right) - \frac{\partial \tau_{ij}}{\partial x_j} \tag{3.4}$$

$$\frac{\partial \bar{u}_i}{\partial x_i} = 0 \tag{3.5}$$

$$\frac{\partial \bar{\phi}}{\partial t} + \bar{u}_i\frac{\partial \bar{\phi}}{\partial x_i} = \Gamma\frac{\partial}{\partial x_i}\left(\frac{\partial \bar{\phi}}{\partial x_i}\right) - \frac{\partial \lambda_i}{\partial x_i} \tag{3.6}$$

Here $(\bar{*})$ means filtered values, p is pressure, ρ is density and ν is kinematic viscosity. The effect of the unresolved scales enters through the subgrid tensor τ_{ij} and the subgrid scalar flux vector λ_i given by

$$\tau_{ij} = \overline{u_i u_j} - \bar{u}_i\bar{u}_j \tag{3.7}$$

and

$$\lambda_i = \overline{u_i\phi} - \bar{u}_i\bar{\phi} \tag{3.8}$$

τ_{ij} and λ_i are unknowns and therefore need modeling. A widely used assumption for the modeling of the subgrid tensor is that the effect of the subgrid scales is limited to an enhanced viscosity. Mathematically this takes the form

$$\tau_{ij} - \frac{1}{3}\tau_{kk}\delta_{ij} = -\nu_{sgs}\left(\frac{\partial \bar{u}_i}{\partial x_j} + \frac{\partial \bar{u}_j}{\partial x_i}\right) = -2\nu_{sgs}\bar{S}_{ij} \tag{3.9}$$

where ν_{sgs} is the eddy viscosity and $\bar{S}_{ij}$ is the filtered rate of strain tensor. The modeling then boils down to modeling ν_{sgs}. The Smagorinsky model [87] gives

$$\nu_{sgs} = \left(C_s\bar{\Delta}\right)^2\sqrt{2\left|\bar{S}\right|^2} \tag{3.10}$$

where $\bar{\Delta}$ is the filter length scale which normally corresponds to the grid size and C_s is a model constant. C_s can be determined dynamically using the dynamic eddy viscosity

method [30, 59]. Then, a second filtering with larger filter width is applied and a subgrid tensor is obtained from the second filtering. Assuming the two subgrid tensors can be modeled in the same manner, an equation is obtained for C_s.

The subgrid scalar flux vector is modeled using the gradient diffusion hypothesis as in Equation 3.2. Subscript *sgs* for subgrid scales is adopted here for the transport coefficients corresponding to the LES equations. This gives

$$\lambda_i = -\Gamma_{sgs} \frac{\partial \bar{\phi}}{\partial x_i} \tag{3.11}$$

where Γ_{sgs} is the subgrid diffusivity and is obtained by rearranging Equation 3.3 to give

$$\Gamma_{sgs} = \nu_{sgs}/Sc_{sgs} \tag{3.12}$$

The governing equations were solved using the open source CFD software OpenFOAM [63] with the PISO (Pressure Implicit with Splitting of Operators) solver. The code is finite volume with co-located grid and Gaussian integration. The grid corresponds to a 30 cm long section of the channel starting at the tip of the splitter plates and is uniform with hexahedron shaped cells. Turbulent inlet velocities were generated using the digital filter method of Klein et al. [50]. Boundary conditions for the velocity field were no-slip at the walls and zero gradient at the outlet. The pressure was fixed at the outlet and set to zero gradient at the walls. The time scheme used in the velocity calculations was second order backwards and implicit, however with the convection term linearized with the previous flux value. Spatial schemes for the velocity field calculations were second order central and cell face values were obtained using linear interpolation. Further details about the numerical setup for the velocity field can be found in Chapter 2.

Boundary conditions for the passive scalar were convective outlet and impermeable walls. The passive scalar was set to a value of one in the center stream inlet and zero in the inlet of the two side streams. Three different time schemes for the passive scalar transport equation were tested: second order backwards, first order Euler, and second order Crank-Nicolson. All three schemes are available in OpenFOAM and are implicit.

The differences in performance of the schemes are best displayed by comparing the variance of concentration as shown in Figure 3.2. It is seen that the backwards and the Crank-Nicolson schemes perform similarly well. Only at location $x/d = 12$ a difference is evident in the right variance peak. The first order scheme gave much lower variance and slower mixing than the two second order schemes. Based on performance and consistency with the velocity field computations, the backward scheme was chosen.

Also for the passive scalar convection term, three different schemes were tried, they are in OpenFOAM named *limitedLinear01, linearUpwind* and *Gamma*. The schemes are all a blend of first and second order accurate. The *limitedLinear01* scheme is a linear scheme with a Sweby [89] limiter and keeps the scalar bounded between 0 and 1. *linearUpwind* is an upwind scheme and *Gamma* [45] is using a blend of central difference and upwind scheme. Although being a bounded scheme, the *linearUpwind* scheme gave passive scalar values out of bounds and was therefore not suitable for this case. Figure 3.3 shows the passive scalar variance values obtained using the three different schemes. It is seen that the upwind scheme gives too high variance and the *Gamma* scheme gives the lowest variance values. The *limitedLinear01* scheme gave the best fit with the experimental data and was therefore chosen. The differences in predicted variance had relatively little effect on the mean concentration profiles (maximum difference in peak mean concentration value was 2% and was at location $x/d = 12$).

The final simulation was run for 85 seconds simulated time, first five seconds to make sure initial effects were gone, then 80 seconds sampling data. Velocity and concentration fields were extracted from the center plane of the channel corresponding to the plane where the simultaneous PIV/PLIF measurements were done. In total 10,000 realizations were collected.

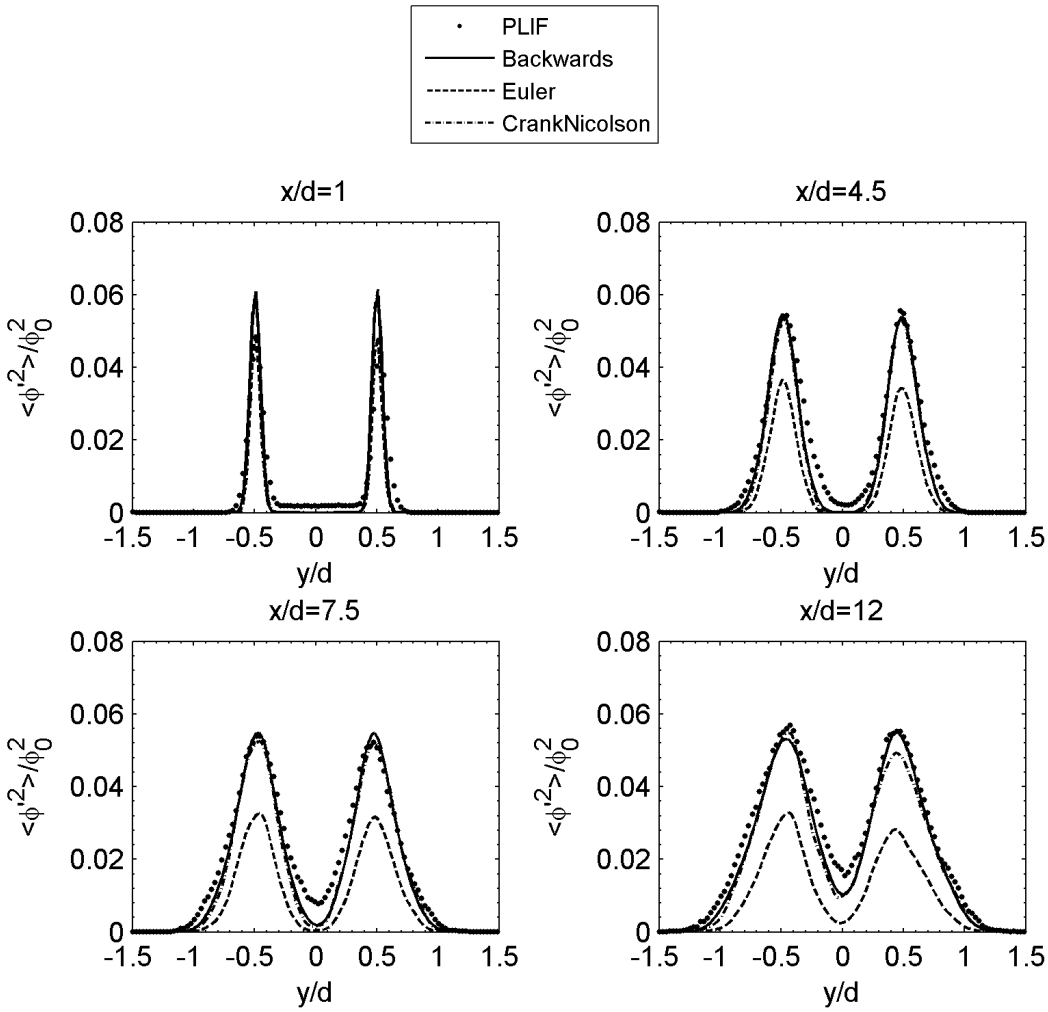

Figure 3.2: Variance of concentration across the channel at $x/d = 1$, 4.5, 7.5 and 12 using different time schemes: backwards, Euler and CrankNicolson. Symbols represent experimental data and lines represent simulation results.

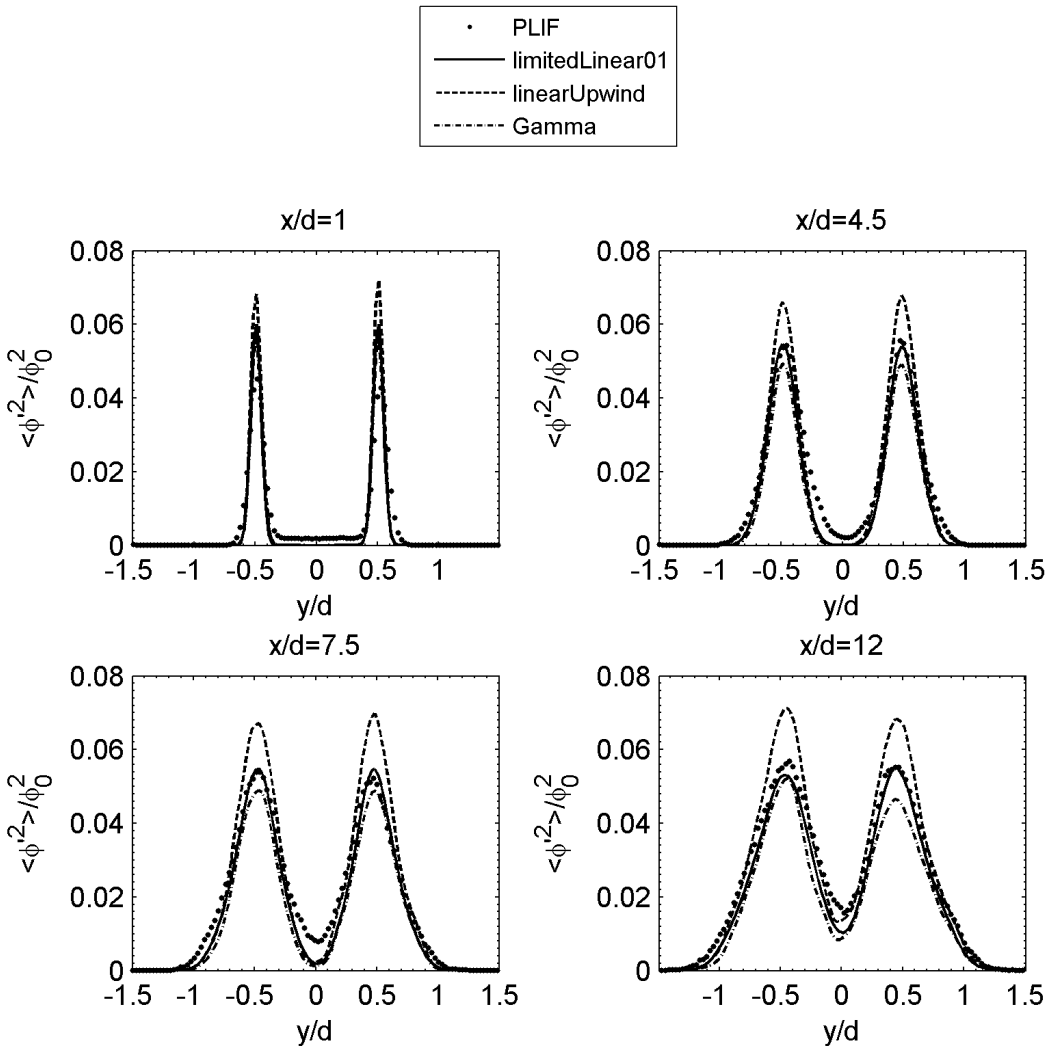

Figure 3.3: Variance of concentration across the channel at $x/d = 1$, 4.5, 7.5 and 12 using *limitedLinear01, linearUpwind* and *Gamma* spatial schemes. Symbols represent experimental data and lines represent simulation results.

3.4 Results

The results are normalized using the distance between the splitter plates, d, the bulk velocity, U_0 and the center stream inlet concentration, ϕ_0. Data are compared at four different downstream locations.

The velocity field in this work corresponds to the velocity field presented in Chapter 2. For convenience the mean and root-mean-square (RMS) of velocity and the Reynolds shear stress are also presented here. Figure 3.4 displays the mean streamwise velocity profiles across the channel at four downstream locations. At location x/d=1 the wakes created behind each of the two splitter plates are clearly recognizable as velocity deficits. It is seen that as the wake develops downstream and mixing causes transfer of momentum, the profiles even out. The simulation reproduces the velocity profiles of the experiment well. The RMS of streamwise and cross-stream velocity are displayed in Figures 3.5 and 3.6 respectively. Both quantities take on large values in the wake regions and by the walls and lower values in the center of each stream. The simulation produces RMS levels similar to the experiment. The center stream values are however a little lower in the simulation than in the experiment, especially for the cross-stream velocity. At the wall, the simulation is not able to accurately reproduce the profiles in the experiment. For that a finer grid resolution or other wall treatment would be necessary. This is however not considered important for our scope, namely the transport of the passive scalar.

The turbulent shear stress is shown in Figure 3.7. The profiles are anti-symmetric with high magnitudes in the wake regions and by the walls. It is seen that the turbulent shear stress changes sign across each wake. This agrees with a vortex street of counter rotating vortices in the wake. The vortices are important for the transport of the passive scalar. The turbulent shear stress is well predicted by the simulation in most of the channel. Also here, discrepancies are seen by the wall and this follows from the differences in the RMS of velocity.

The mean concentration profiles are displayed in Figure 3.8. The concentration profile is a top hat profile at the inlet and evens out as the wake develops and the mixing progresses. It is seen from the figure that the mean concentration is well predicted in the simulation and that the spreading rate is captured. The peak mean concentration value at location $x/d = 7.5$ deviates in the simulation a little from the experiment and the simulation peak value is 5.6% higher than the experimental value.

The variance of concentration is a good measure of the mixing rate. High variance means rapidly changing concentration values. Therefore, when the simulation can reproduce the experimental variance profiles it is a good indicator that the mixing process is well predicted. It is seen in Figure 3.9 that the concentration variance takes on high values in the wake regions. The simulation predicts the concentration variance very well. It is only at location $x/d = 1$ that the simulation overshoots the experimental profiles noteworthy. The width of the variance peaks is also well predicted in the simulation. This is a good indication that the rate the mixing is progressing with downstream distance is captured in the simulation.

Since the simultaneous PIV/PLIF offers the opportunity to compute turbulent fluxes, it is an excellent tool for studying the transport mechanisms in the turbulent flow. Figure 3.10 displays the streamwise turbulent flux computed as in the RANS framework, using ensemble averaging. The flux is negative in the outer part of the wake region and positive in the inner part. The peaks are highest at the location closest to the inlet and decrease in magnitude with downstream distance. As the wake develops downstream and the mixing region broadens, the regions of positive and negative flux broaden too. The simulation gives somewhat higher flux peaks than the experiment, especially close to the inlet. Elsewhere, the simulation profiles are closely following those of the experiment and decrease in strength and broaden in the same way as the experimental profiles do.

In Figure 3.11 the cross-stream turbulent flux is plotted. Since the concentration gradient is in the cross-stream direction, this flux is important in the mixing of the passive

scalar. The cross-stream turbulent flux profiles are anti symmetric and peak negative in the left wake region and positive in the right wake region. This is because a positive fluctuation in cross-stream velocity in the left wake region transports low concentration fluid from the left stream to the center stream (negative concentration fluctuation), while in the right wake region a positive cross-stream velocity fluctuation transports high concentration fluid from the center stream to the right stream (positive concentration fluctuation). Similarly, a negative velocity fluctuation transports low concentration fluid from right stream to center stream in the right wake region and high concentration fluid from center stream to left stream in the left wake region. The peaks are, as for the streamwise flux, decreasing in strength and broadening with downstream distance. The exception is at location $x/d = 1$, where the magnitude of the flux peaks are lower in the experiment than at the other three locations. The simulation however gives high peak at that location and this follows from the overprediction in concentration variance at that location.

In RANS the turbulent flux is described by Equation 3.2. The usual approximation is to use a scalar value for the turbulent diffusivity, Γ_T. One can however assume Γ_T to be a tensor. This gives:

$$\langle u_i' \phi' \rangle = -\Gamma_{ij} \frac{\partial \langle \phi \rangle}{\partial x_j} \tag{3.13}$$

Here and in the following $\langle\rangle$ represents Reynolds averaging and u_i' and ϕ' are fluctuating components of velocity and concentration. Now assuming the streamwise and spanwise components of the concentration gradient to be negligible, two components of the turbulent diffusivity tensor can be obtained.

$$\Gamma_{12} = \frac{\langle u' \phi' \rangle}{\frac{\partial \langle \phi \rangle}{\partial y}} \tag{3.14}$$

$$\Gamma_{22} = \frac{\langle v' \phi' \rangle}{\frac{\partial \langle \phi \rangle}{\partial y}} \tag{3.15}$$

Figure 3.12 displays the off-diagonal component of the turbulence diffusivity, Γ_{12}. This component would need to be zero for the assumption of scalar turbulent diffusivity to be valid. It is seen that only close to the walls, where the turbulent fluxes are zero, Γ_{12} is also zero. Otherwise, it takes on a anti-symmetric profile with positive peaks in the left side of each wake region and negative peak in the right side of each wake region. It is seen that Γ_{12} is well predicted by the simulation. The slightly higher peak values found in the simulation follow from the higher streamwise turbulent flux values. The success of the LES in this matter despite employing a scalar turbulent diffusivity demonstrates the superiority of LES over RANS.

Γ_{22} is displayed in Figure 3.13. It is positive and peaks in each wake region. A negative value of Γ_{22} would be surprising since it would mean turbulent diffusion in the opposite direction of the concentration gradient. The prediction of Γ_{22} is very accurate and it is only at the location most downstream that the simulation deviates from the experimental values. Here, the turbulent diffusivity is larger in the simulation than in the experiment. This follows from the slight overprediction of the cross-stream turbulent flux at this location.

The simultaneous PIV/PLIF data offer the opportunity to investigate the coherent structures of the flow. Since these are of great importance in the transport of the passive scalar, the simulation should produce turbulent coherent structures similar to those of the experimental flow. Two-point spatial correlations are an excellent way of comparing such spatial information. The two-point spatial cross-correlation of velocity and concentration is described by:

$$R_{u_i\phi}\left(\boldsymbol{x},\boldsymbol{X}\right) = \frac{\left\langle u_i'\left(\boldsymbol{x}\right)\phi'\left(\boldsymbol{X}\right)\right\rangle}{\sqrt{\left\langle u_i'^2\left(\boldsymbol{x}\right)\right\rangle\left\langle \phi'^2\left(\boldsymbol{X}\right)\right\rangle}} \tag{3.16}$$

where $\boldsymbol{x}$ is the vector of spatial coordinates and $\boldsymbol{X}$ is the position vector of the basis point of the correlation. Basis points are at $y/d = 0.5$ and at four downstream locations.

The two-point cross-correlation of streamwise velocity with concentration is shown in Figure 3.15. Left of the basis point is a positively correlated region and right is a neg-

atively correlated region. The size of the correlation regions increase with downstream distance, as the smallest coherent structures are dissipating. It can be seen that the simulation is predicting both these features well. Figure 3.16 shows the corresponding figures for the two-point cross-correlations of cross-stream velocity and concentration. Around the basis point, a positive correlation region that is stretched in the cross-stream direction is seen. Upstream and downstream of the positive region, smaller and weaker negatively correlated regions are found. The correlations correspond to positive velocity fluctuation transporting high concentration from center stream to side stream and negative velocity fluctuation transporting low concentration from side stream to center stream. The correlation with cross-stream velocity is stronger than with streamwise velocity. The two-point correlations are well predicted by the simulation, although the simulation gives somewhat stronger correlations. The difference can originate in experimental noise. The ability of the simulation to reproduce the two-point correlations is a strong indicator that the coherent structures of the flow are predicted by the simulation. The coherent structures contribute to the mixing and transport of the passive scalar and are therefore important to be able to predict.

3.5 Summary and Conclusions

This work presents a successful application of large eddy simulation to predict the transport of a passive scalar in a turbulent confined wake flow. The work builds on that of Chapter 2 and was done using the open source CFD software OpenFOAM [63]. The gradient diffusion hypothesis was used to close the transport equation of the passive scalar. Different temporal and spatial numerical schemes for the transport of the passive scalar were tested. It was found that a first order Euler time scheme was not able to predict the mixing rate correctly. The two second order time schemes tested gave good results. Of spatial schemes the upwind scheme gave unbounded values and was therefore

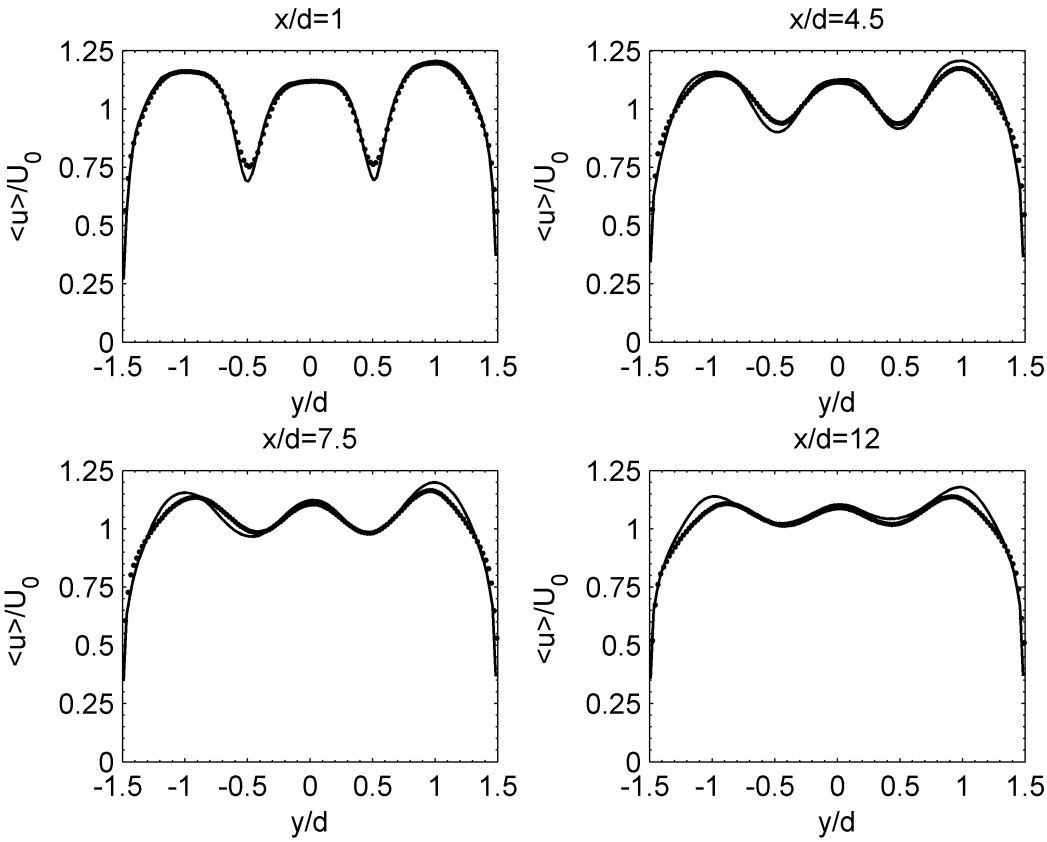

Figure 3.4: Mean velocity profiles across the channel at $x/d = 1$, 4.5, 7.5 and 12. Symbols represent experimental data and lines represent simulation results.

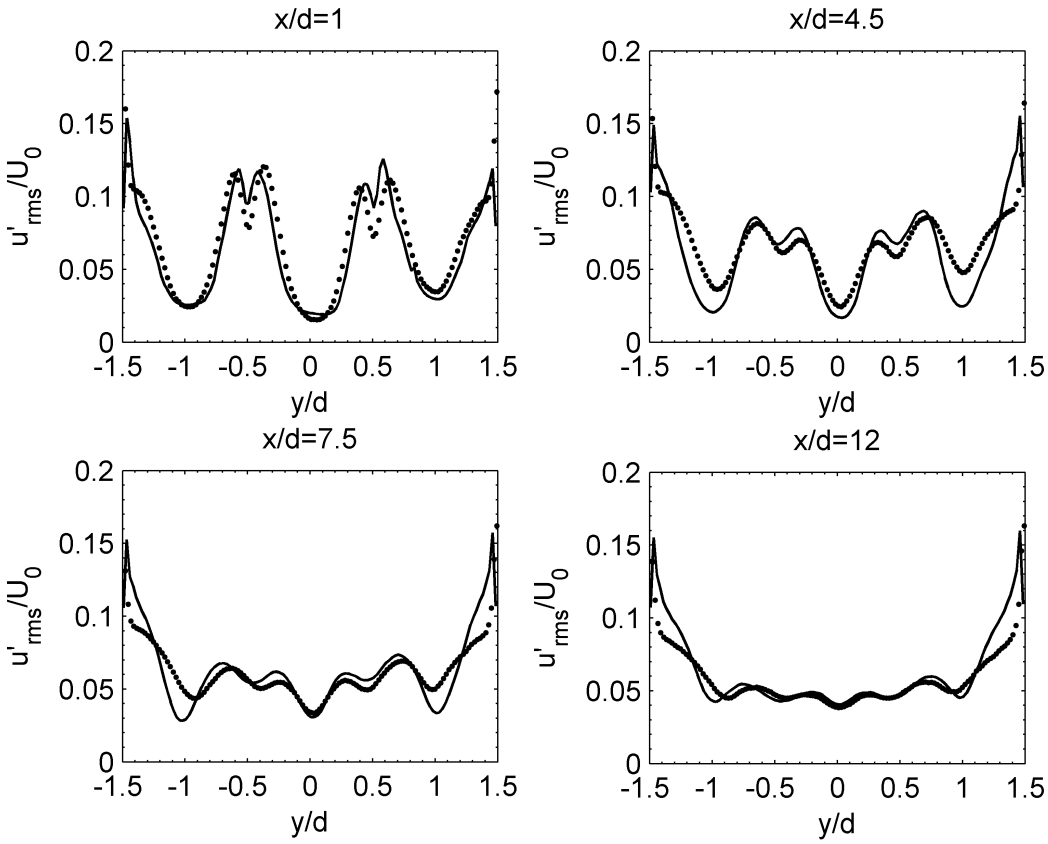

Figure 3.5: RMS of streamwise velocity. Profiles across the channel at $x/d = 1$, 4.5, 7.5 and 12. Symbols represent experimental data and lines represent simulation results.

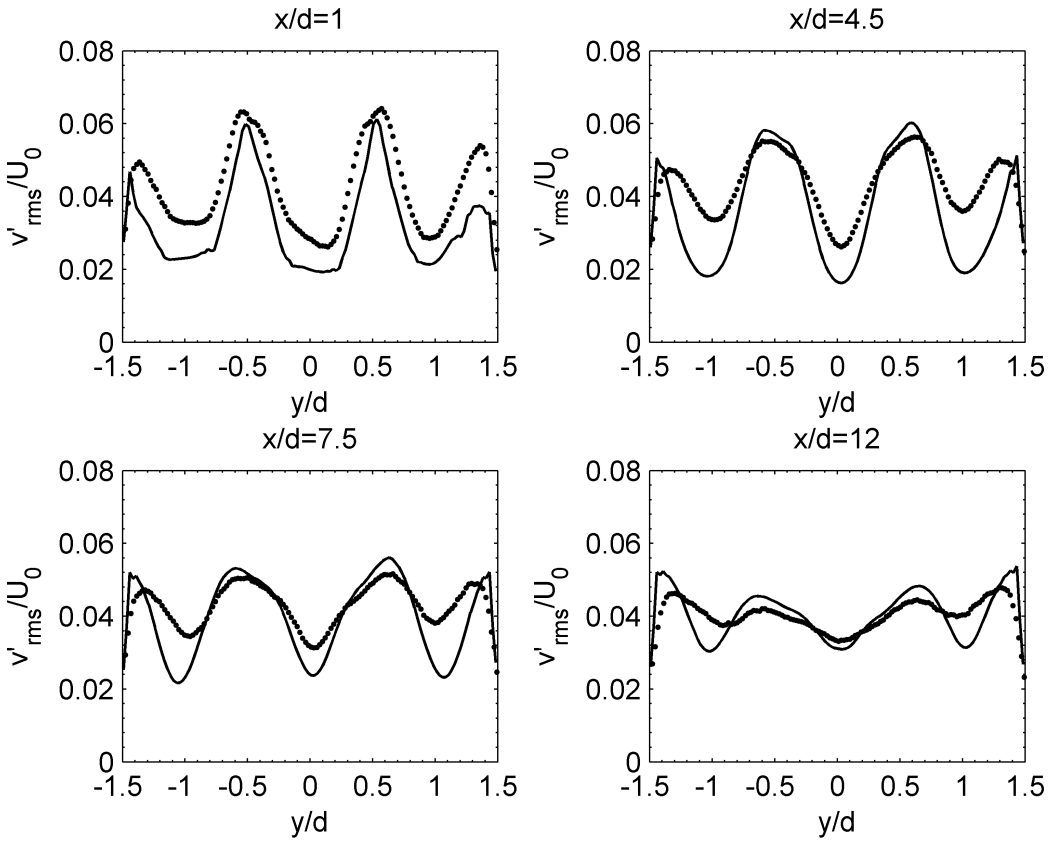

Figure 3.6: RMS of cross-stream velocity. Profiles across the channel at $x/d = 1$, 4.5, 7.5 and 12. Symbols represent experimental data and lines represent simulation results.

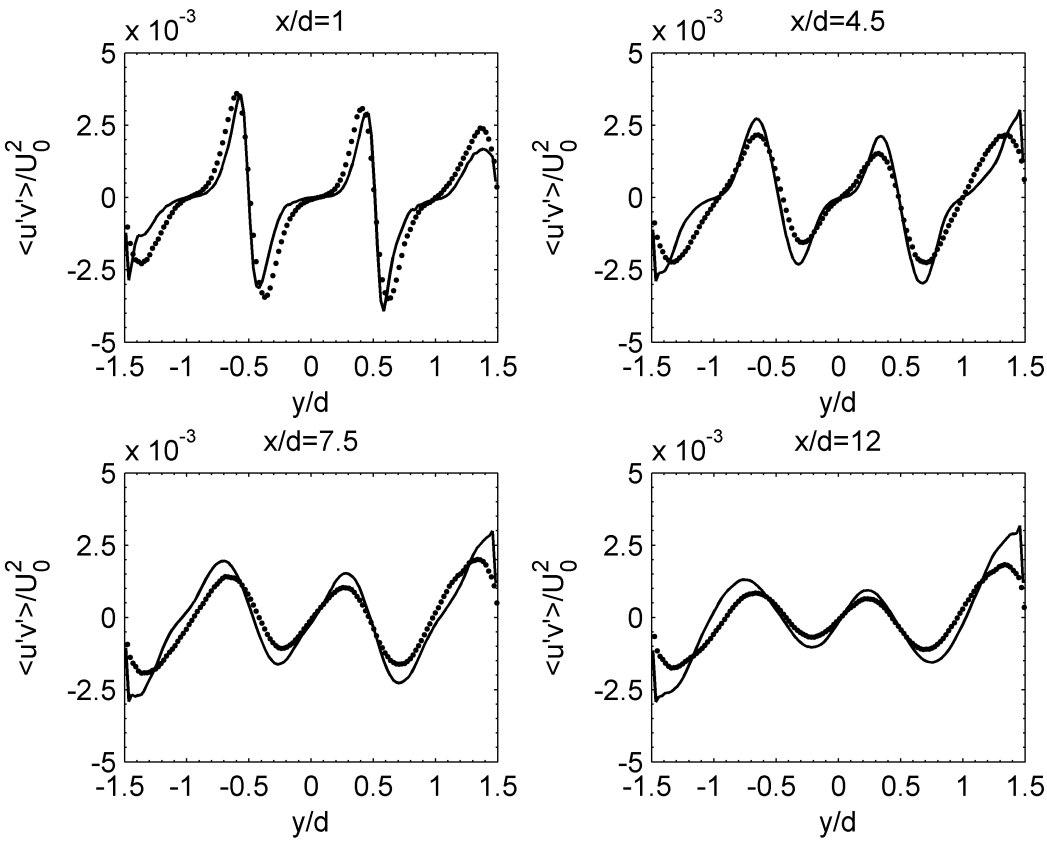

Figure 3.7: Reynolds shear stress. Profiles across the channel at $x/d = 1$, 4.5, 7.5 and 12. Symbols represent experimental data and lines represent simulation results.

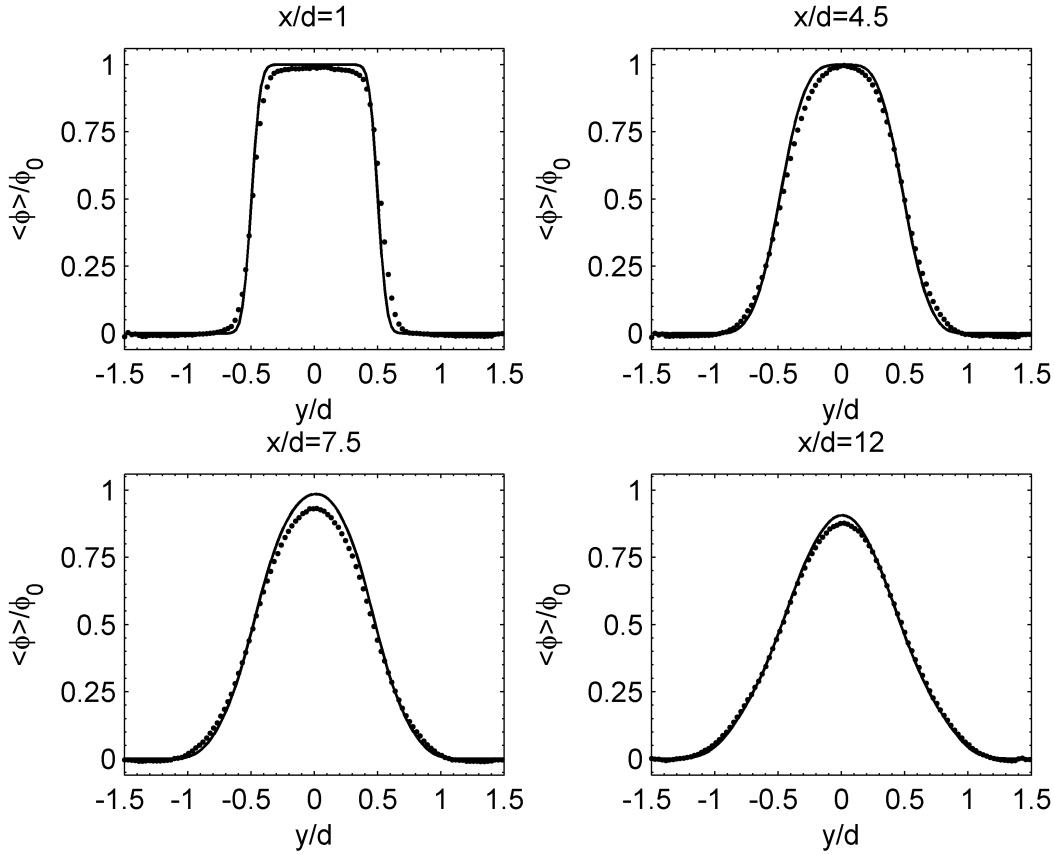

Figure 3.8: Mean concentration profiles across the channel at $x/d = 1$, 4.5, 7.5 and 12. Symbols represent experimental data and lines represent simulation results.

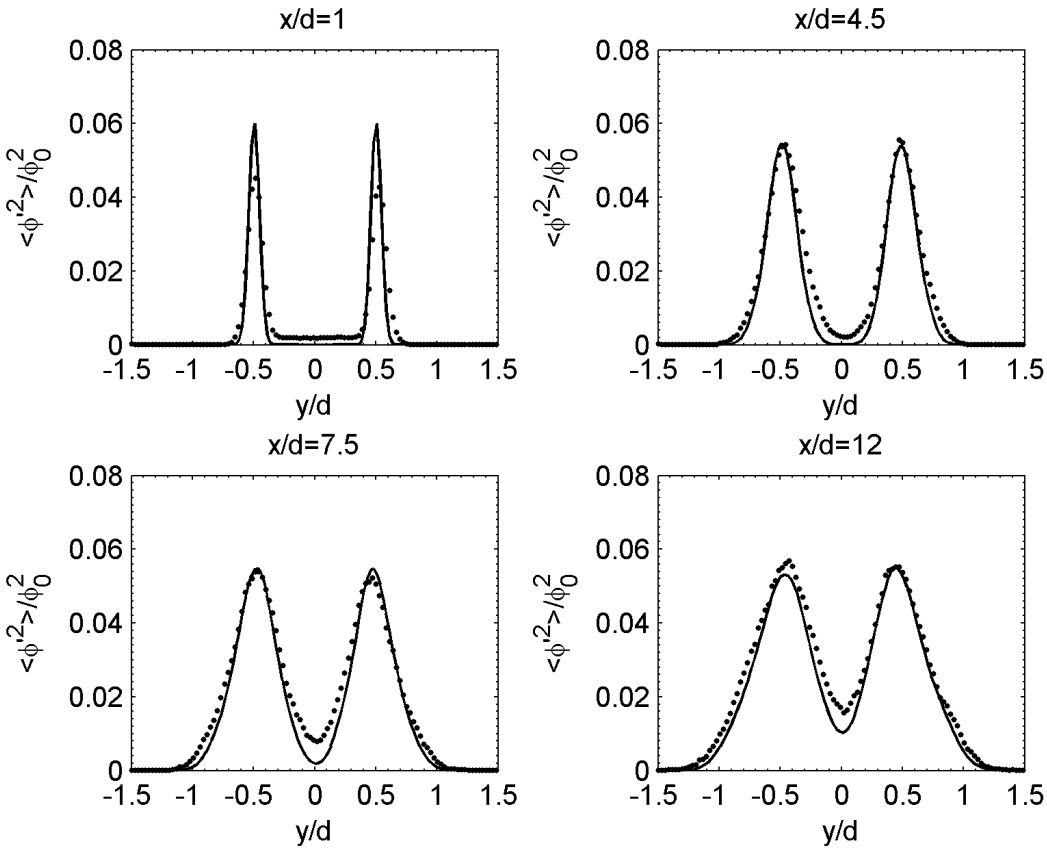

Figure 3.9: Variance of concentration across the channel at $x/d = 1$, 4.5, 7.5 and 12. Symbols represent experimental data and lines represent simulation results.

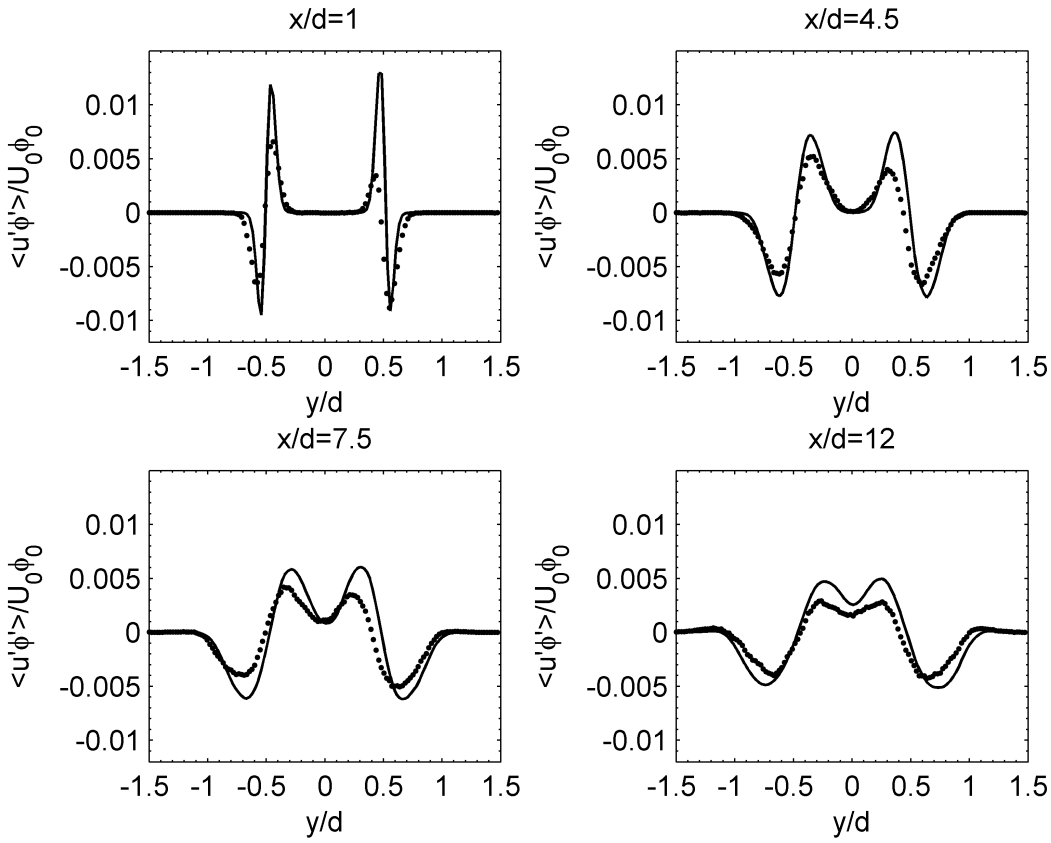

Figure 3.10: Streamwise turbulent flux. Profiles across the channel at $x/d = 1$, 4.5, 7.5 and 12. Symbols represent experimental data and lines represent simulation results.

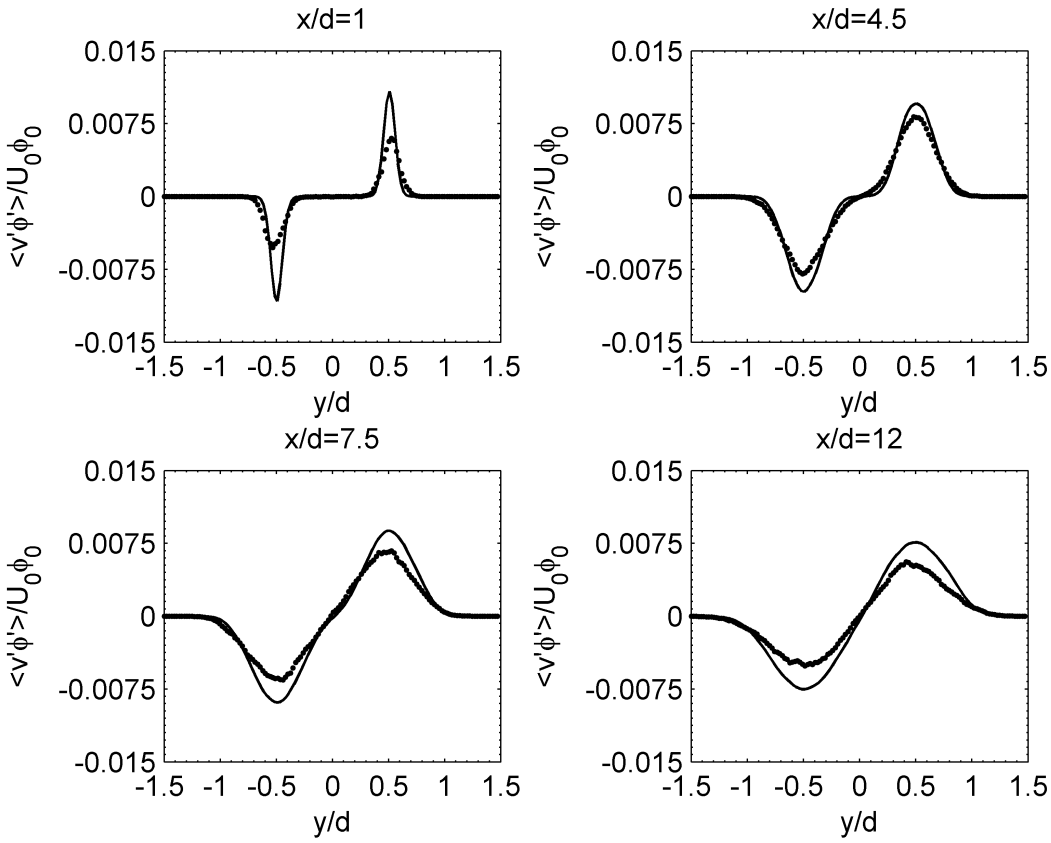

Figure 3.11: Cross-stream turbulent flux. Profiles across the channel at $x/d = 1$, 4.5, 7.5 and 12. Symbols represent experimental data and lines represent simulation results.

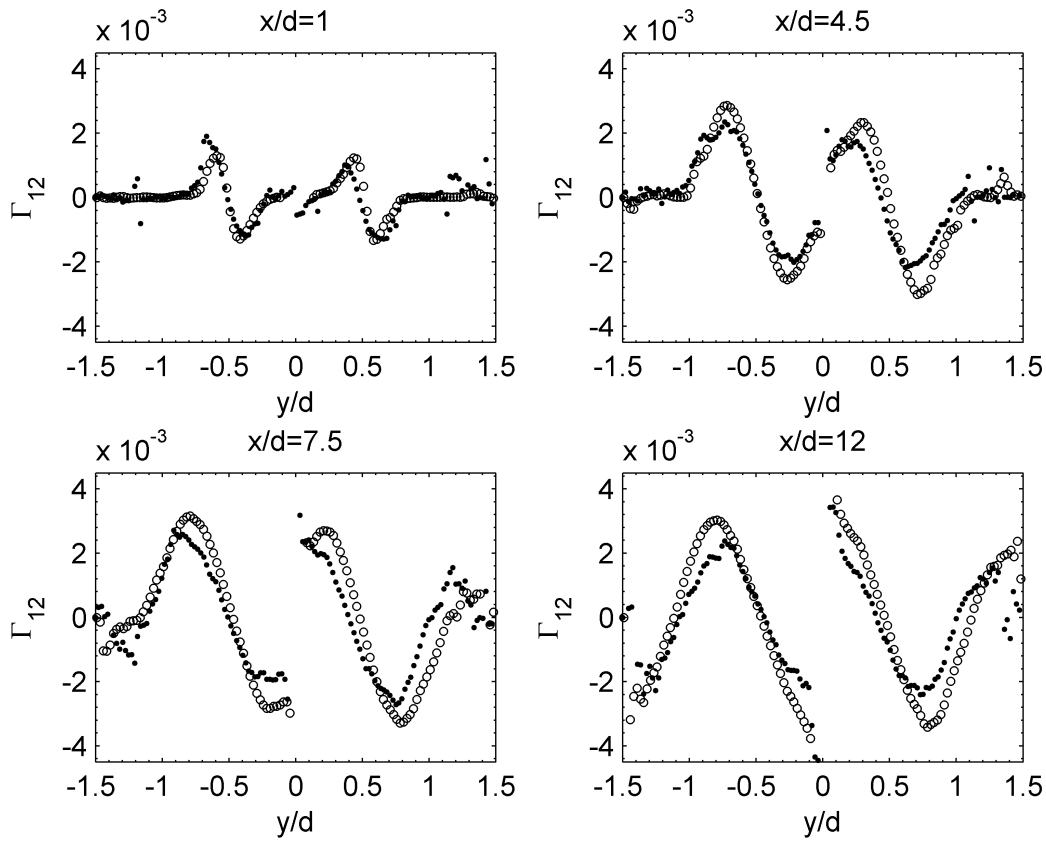

Figure 3.12: Off-diagonal component of turbulent diffusivity, Γ_{12}. Values across the channel at $x/d = 1$, 4.5, 7.5 and 12. Filled symbols represent experimental data and open symbols represent simulation results.

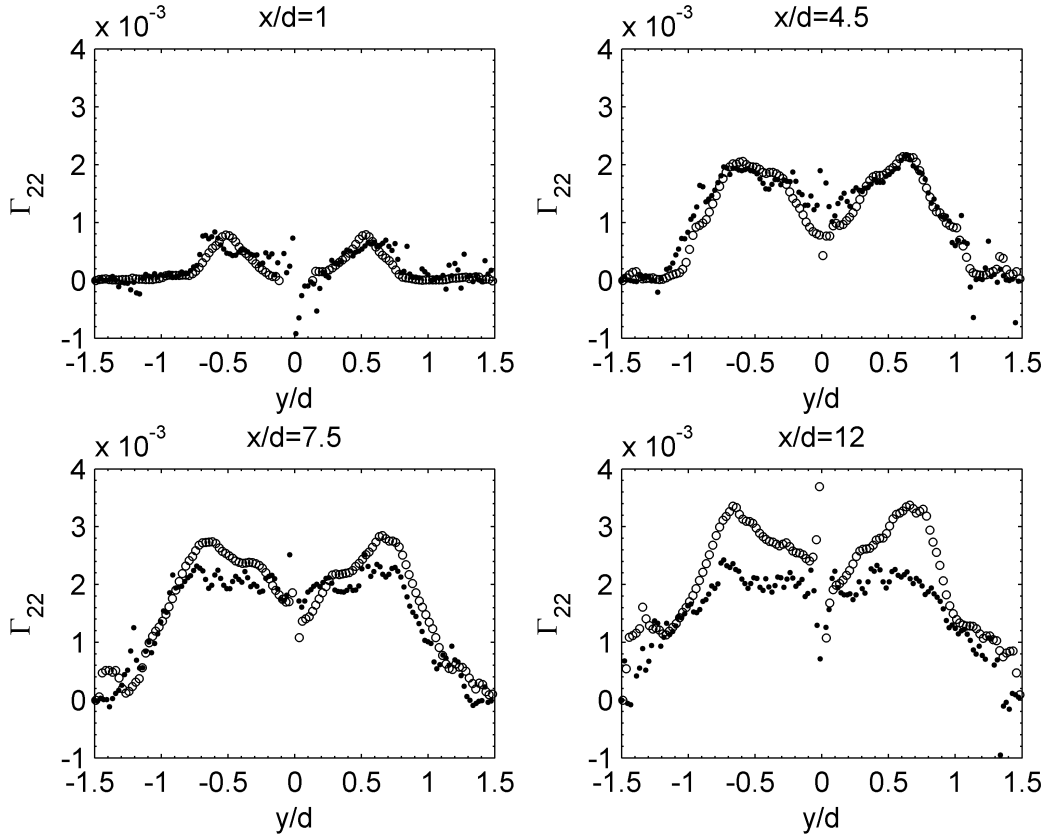

Figure 3.13: Diagonal component of turbulent diffusivity, Γ_{22}. Values across the channel at $x/d = 1$, 4.5, 7.5 and 12. Filled symbols represent experimental data and open symbols represent simulation results.

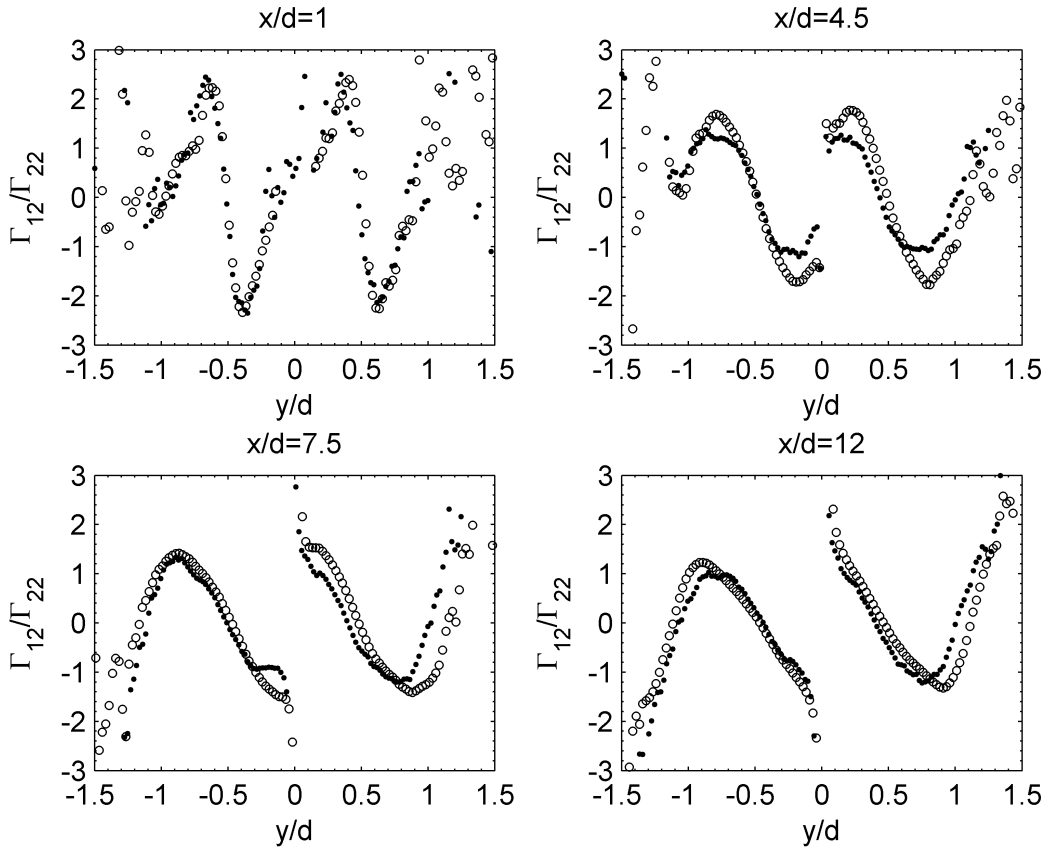

Figure 3.14: Ratio of two components of turbulent diffusivity, Γ_{12}/Γ_{22}. Values across the channel at $x/d = 1$, 4.5, 7.5 and 12. Filled symbols represent experimental data and open symbols represent simulation results.

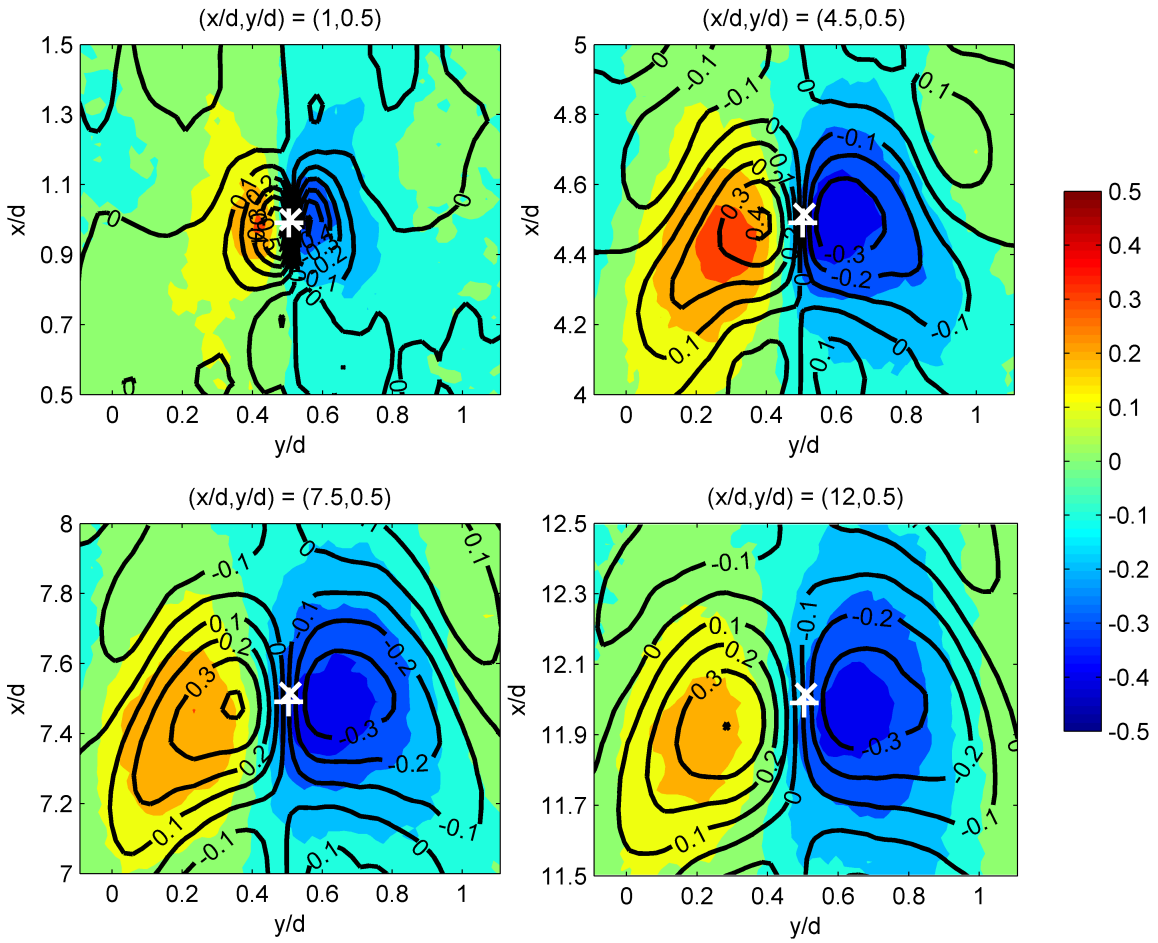

Figure 3.15: Two-point spatial cross-correlation of streamwise velocity and concentration, $R_{u\phi}$. Color contours are simultaneous PIV/PLIF data and black line contours are LES data. Contours in steps of 0.1. Basis points are marked in white.

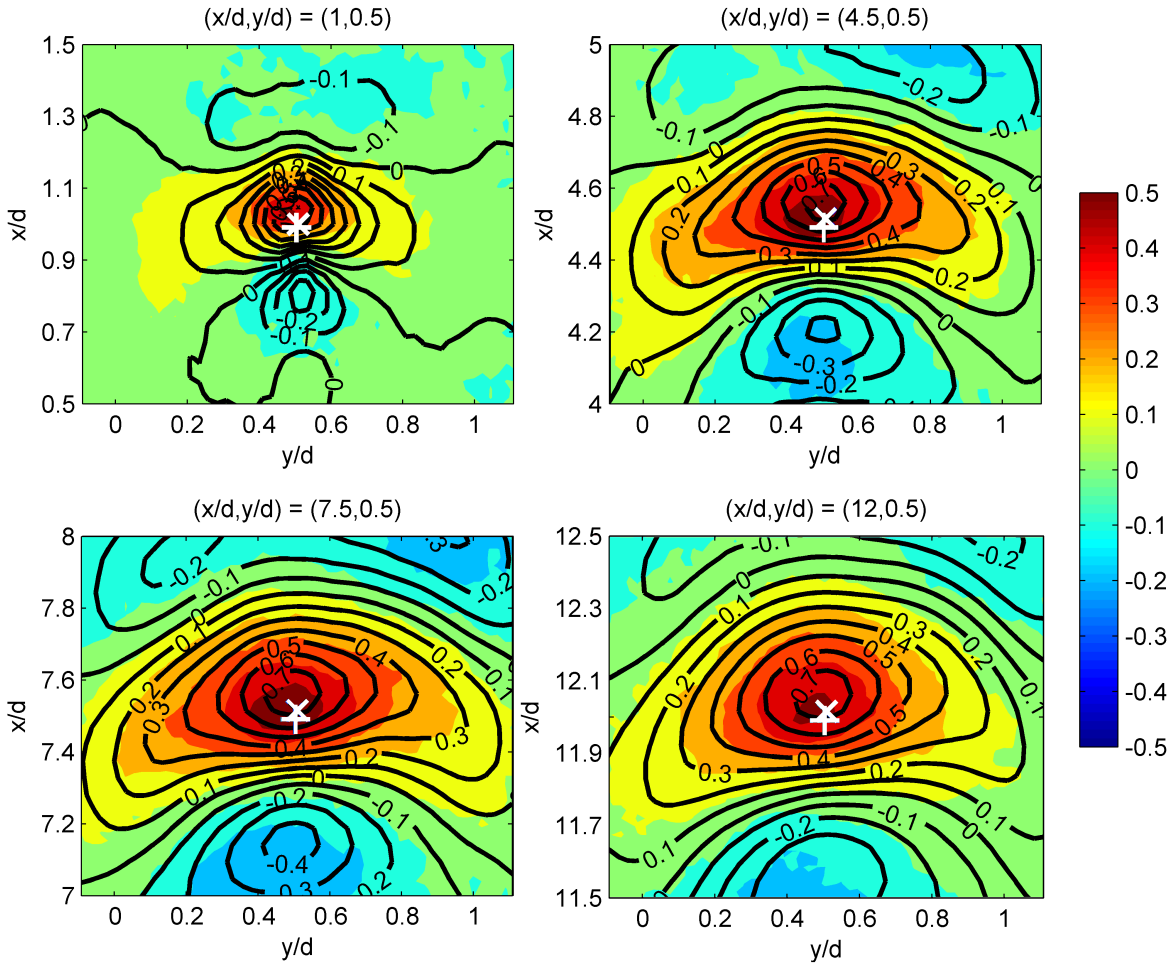

Figure 3.16: Two-point spatial cross-correlation of cross-stream velocity and concentration, $R_{v\phi}$. Color contours are simultaneous PIV/PLIF data and black line contours are LES data. Contours in steps of 0.1. Basis points are marked in white.

not suitable to predict the passive scalar transport. The limited linear scheme was found to be a good choice.

Simulation results were validated in-depth by comparison to simultaneous PIV/PLIF data of Feng et al. [24]. Point-wise statistics of the simulation compared well to the experimental data. Two components of the turbulent diffusivity tensor were computed from the simulation results and from the experimental data. They compared quite well and this demonstrates that the transport mechanisms were captured in the simulation.

Two-point spatial correlations of passive scalar with velocity showed good agreement between simulation and experiment, indicating that the turbulent coherent structures of the flow are well predicted by the simulation.

The fit with experimental data, not only of point-wise statistics, but also of transport coefficients and structural information, demonstrates that the simulation method presented is suitable to study the mixing and transport process in this turbulent wake flow.

CHAPTER 4. LARGE-EDDY SIMULATION OF PASSIVE SCALAR TRANSPORT AND MIXING IN A CO-FLOWING TURBULENT RECTANGULAR JET

A paper in preparation

Katrine M. Nilsen[1], Bo Kong[2], Rodney O. Fox,

James C. Hill and Michael G. Olsen[3]

Abstract

Turbulent transport of a passive scalar in a turbulent confined jet with co-flow was investigated. Simultaneous velocity and concentration measurements of the jet flow were made. The turbulent jet was also simulated using large eddy simulation with passive scalar transport. The simulation results were compared to the experimental data.

Statistics of velocity and passive scalar, as well as transport related quantities such as turbulent fluxes and turbulent diffusivities, were computed and compared between simulation and experiment. The coherent structures of the flow were studied using two-point spatial correlations.

The simulation results agreed overall well with the experiment.

[1]Primary author
[2]Experimental and numerical researcher
[3]Corresponding author

4.1 Introduction

One of the fundamental problems in turbulence is to predict transport of a passive scalar. Understanding of the transport process is important not only in mixing applications but also in applications ranging from dispersion of a pollutant in the atmosphere to heat transfer. Knowing the mechanisms that govern turbulent transport of a passive scalar is also a prerequisite for being able to predict turbulent reacting flows, which is of great advantage to industries like chemical processing and oil production as well as the combustion community.

One flow type in which turbulent mixing occurs is the turbulent jet. Jet configurations that have been often studied are the axisymmetric jet [5, 19, 97, 17] and the planar jet [22, 71, 92]. In studies of these types of jets it has been well established that turbulent coherent structures contribute to fluid entrainment and mixing [16, 3, 10, 33, 34]. In most practical applications where jets are present, the jet is not in one of these canonical forms; rather, in most applications the jet has some form of confinement. Examples of jets with confinement are wall-jets [95], impinging jets [38] and jets in channels [12]. These configurations, although traditionally less studied, are therefore highly relevant to investigate. A jet with co-flow is a jet that, instead of exiting into quiescent fluid, exits into a stream flowing in the same direction as the jet. The turbulent jet with co-flow has been studied for different geometries, velocity ratios and Reynolds numbers [56, 39, 62].

With improving availability of computer power, Computational Fluid Dynamics (CFD) is becoming more and more popular both in research and in industry. While the prediction of velocity statistics in turbulent flows alone is a complex task, transport of a scalar adds complexity, not to mention the challenge of predicting chemical reactions in turbulent flows. Large-Eddy Simulation (LES) [82] is a numerical method that solves a filtered set of the governing equations, thus resolving the flow down to a given scale. The effect of the unresolved scales, or subgrid scales, is modeled. LES offers a great advan-

tage over the commonly used Reynolds Averaged Navier Stokes method (RANS) in that it provides information about the large-scale flow structures. This becomes especially important when considering mixing, for example in cases where local peak concentrations or reaction rates are of interest. LES requires much less computational power than Direct Numerical Simulation (DNS) and is therefore feasible for a wider range of flows. However, LES involves modeling, and therefore validation of the method is appropriate.

Experimental data offer a good way of validating numerical simulations. The more information obtained from experiments, the more detailed the validation can be and therefore the better confidence one can have in the simulation method. Particle Image Velocimetry (PIV) [1] and Planar Laser-Induced Fluorescence (PLIF) are non-intrusive methods of measuring velocity and concentration fields, respectively. In PIV the flow is seeded with tracer particles and a plane in the flow is illuminated by a laser sheet. A camera captures images of the scattered light from the tracer particles. From the images the displacement of particles can be found. From these, knowing the time difference between two images, the velocity vectors can be obtained. PLIF also makes use of a laser sheet to illuminate a plane of the flow. In order to measure concentration, a fluorescent dye is used. The laser light excites the dye and the resulting fluorescent light emitted by the dye is captured by a camera. The intensity of the fluorescent light is dependent on the illumination intensity as well as the dye concentration. Through calibration of the system, a relation between captured light intensity and dye concentration can be obtained.

A very informative set of data is obtained when these two experimental methods are performed simultaneously. Since both measurement procedures can make use of the same laser sheet, by using two cameras, one for PIV and one for PLIF, velocity and concentration data for the same field at the same instance of time can be obtained. One application of simultaneous PIV/PLIF has been to investigate turbulent jet flames. For example, Boxx et al. [7] studied a turbulent lifted jet flame by simultaneous high-speed

stereo-PIV/OH-PLIF. Hu et al. [44] applied simultaneous PIV/PLIF to study mixing in an axisymmetric, free water jet at a Reynolds number of 6000. They were able to obtain turbulent flux values for the near field of the turbulent jet. An incompressible, rectangular turbulent jet with co-flow was studied by Feng et al. [23] using simultaneous PIV/PLIF. The measurements were made at a Reynolds number of 50,000 based on the channel hydraulic diameter. Turbulent fluxes and spatial correlations of velocity and concentration was obtained and turbulent diffusivity as well as turbulent Schmidt number was evaluated.

In the present study, the rectangular, confined channel jet with co-flow is studied experimentally and numerically at a Reynolds number of 20,000. The jet velocity is twice that of the co-flowing streams. The rectangular configuration has an experimental advantage over cylindrical facilities in that one avoids problems caused by distortion of light as it passes through the curvature in cylinder walls.

Previous work by Kong et al. [51] validated the accuracy of large-eddy simulation to predict both the pointwise and spatial characteristics of the turbulent velocity field for this confined jet flow, but did not investigate passive scalar transport. The present study extends the work of Kong et al. by investigating the accuracy of LES to predict the pointwise and spatial characteristics of the turbulent scalar field. The detailed experimental data with the unique nature of full-field simultaneous velocity and concentration data offer the possibility of a thorough validation of the LES method. The validation includes evaluation of the spatial structures of the flow and turbulent fluxes, both crucial in turbulent transport.

4.2 Experimental apparatus and methodology

The flow facility consists of a rectangular channel with three inlets separated by two splitter plates. The flow rate of the inlet streams can be controlled independently.

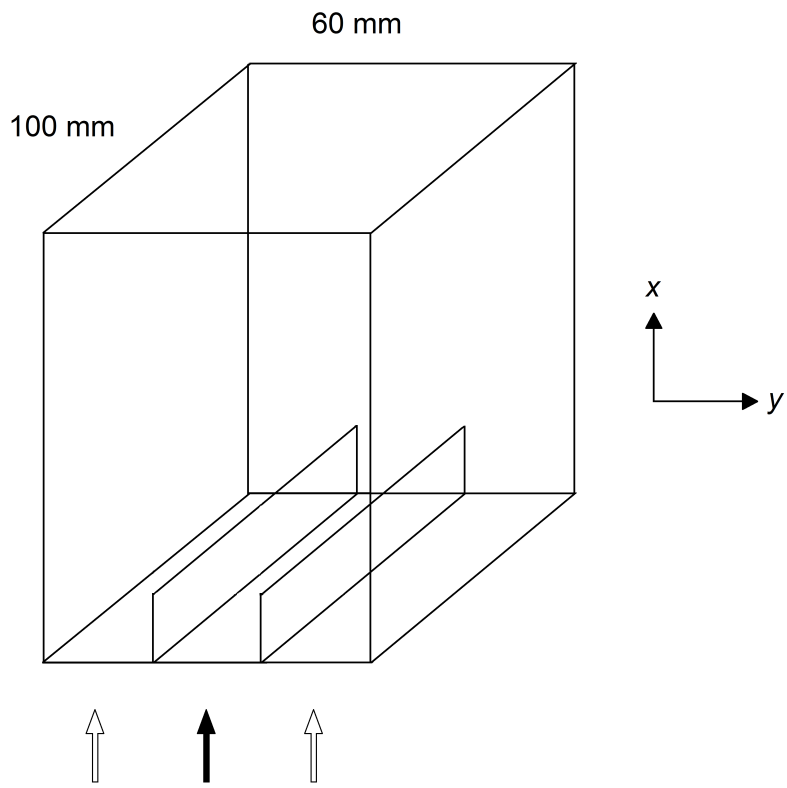

Figure 4.1: The flow geometry. Three inflow streams separated by two splitter plates. Passive scalar in the center inflow only.

Upstream of the inlet, a flow conditioning section consisting of a packed bed of marbles, turbulence reducing screens, and a 16:1 contraction is implemented. The channel cross section is 60x100 mm and the overall length is 1 m. The width of each inlet is 2 cm and the aspect ratio of the rectangular jet is 5. A schematic of the flow facility is shown in Figure 4.1. The x coordinate is chosen to be increasing in the flow direction, and the y coordinate is zero in the center of the channel and increases towards the right channel wall. The working fluid in these experiments was water. The flow rate of the two side streams was 0.4 L/s and the center stream flow rate was 0.8 L/s. This corresponds to bulk inlet velocities of 0.2 m/s and 0.4 m/s respectively and a Reynolds number of 20,000 based on the channel bulk velocity and hydraulic diameter.

Here follows a brief description of the simultaneous velocity and concentration mea-

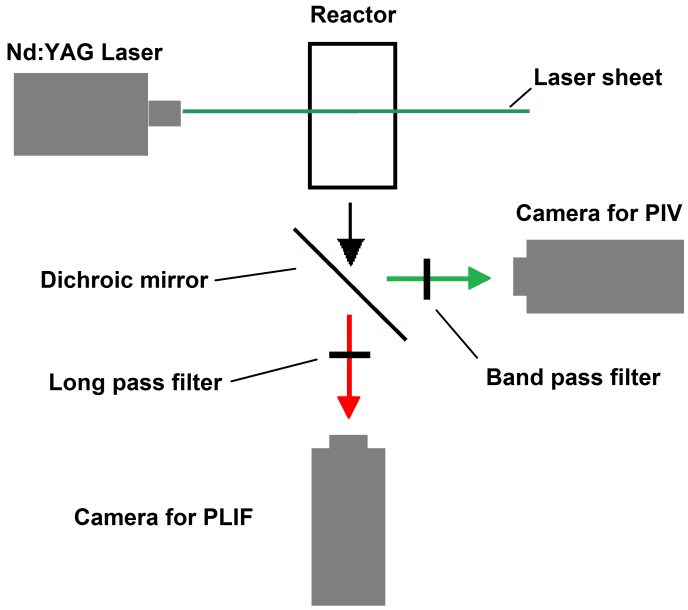

Figure 4.2: Schematic of the PIV/PLIF set up.

surements. A schematic of the PIV/PLIF set up is shown in Figure 4.2. Further details about the experimental method and facility be found in [25, 23].

4.2.1 Particle Image Velocimetry

PIV was used to measure instantaneous velocity fields in a planar cross section of the channel at its spanwise center. The flow was seeded with hollow glass spheres with a nominal diameter of 11.7 μm and a density of 1.1 g/cm^3. A double-pulsed Nd:YAG New Wave Research Gemini PIV laser was used to produce a pulsating light sheet at the spanwise center plane of the channel. The wavelength of the laser light is 532 nm, the maximum pulse energy is 120 mJ and the pulse duration is approximately 5 ns. A 12-bit LaVision Flowmaster 3S CCD camera with a resolution of 1280x1024 pixels was used to capture the scattered light from the glass particles, one image for each laser pulse. The image magnification was 0.12 and the numerical aperture was 8. A time delay between two laser pulses of 600 μs was used in the present study. Through a cross-

correlation technique using multi-pass interrogation scheme with decreasingly smaller window sizes, the displacement of the particles between one image to the next was determined. From that and the known time delay velocity data was obtained. The final interrogation window size measured 16 pixels by 16 pixels and a 50% overlap between adjacent interrogation windows were used. This results in a velocity vector spacing of 0.45 mm. The random error in PIV measurements can conservatively be estimated as one tenth of the effective particle image diameter [76]. In these measurements, the particle image diameter was 8.3μm, corresponding to an error relative to the particle displacement of $\pm$1.7% in the center stream and $\pm$3.4% in the outer streams. Christensen [13] describes the peak locking effect in which the measured particle displacement is biased towards integer pixel displacements. The peak locking coefficient [88] is a measure of how strong the peak locking effect in a given PIV system is. A peak locking coefficient of 0 indicates no peak locking effect, while a value of 1 indicates strong peak locking effect. For the results presented here, the peak locking coefficient was found to be 0.05 which is concidered an acceptably low value.

4.2.2 Planar Laser-Induced Fluorescence

Simultaneously, concentration fields were measured using PLIF. The fluorescent dye was Rhodamine 6G which in water has a Schmidt number of 1250 [15]. The center stream had a dye concentration of 45 μg/l while the two outer streams were pure water. The dye was illuminated by the same laser sheet as for the PIV measurements. When excited by the 532 nm laser light, Rhodamine 6G emits fluorescence with a peak emission wavelength of 555 nm. A second Flowmaster 3S CCD camera was used to capture the fluorescent light. The image magnification of the PLIF measurements was 0.12, and the numerical aperture was 5.6. After correcting the images for spatial illumination intensity variation and gray offset values, local dye concentration was found based on local fluorescence intensities. Sources of measurement error are the shot-to-shot variation

of laser intensity and the camera noise. These were investigated by recording test images using constant dye concentration. The image intensity variation was found to be within 2%.

A dichroic mirror was placed between the channel and the cameras in order to separate the scattered lights from the particles from the fluorescent light from the dye. The two cameras were carefully aligned in order for coordinates from PIV and PLIF to coincide. The data recording was carried through at a frame rate of 1 Hz, and in total 2500 instantaneous data sets were captured. The measurements were repeated at two downstream locations.

4.3 Large-Eddy Simulation

4.3.1 Filtered Navier-Stokes equations

LES is based on the scale-decomposition of the dependent variables into a larger, resolved scale component and a smaller, subgrid scale component. The separation of the resolved scales from the subgrid scales is obtained by applying a spatial filter to the governing equations. The filter takes the convolution form given in equation 4.1.

$$\bar{\psi}(\mathbf{x},t) = \int_{-\infty}^{\infty}\int_{-\infty}^{\infty} \psi(\xi,t')G(\mathbf{x}-\xi,t-t')dt'd^3\xi \tag{4.1}$$

G is here the filter function. $(\bar{*})$ represents filtered values.

Applying the filter to the Navier-Stokes equations gives a set of governing equations for the resolved scales.

$$\frac{\partial \bar{u}_i}{\partial t} + \frac{\partial}{\partial x_j}(\bar{u}_i\bar{u}_j) = -\frac{1}{\rho}\frac{\partial \bar{p}}{\partial x_i} + \nu\frac{\partial}{\partial x_j}(\frac{\partial \bar{u}_i}{\partial x_j} + \frac{\partial \bar{u}_j}{\partial x_i}) - \frac{\partial \tau_{ij}}{\partial x_j} \tag{4.2}$$

$$\frac{\partial \bar{u}_i}{\partial x_i} = 0 \tag{4.3}$$

Here $\bar{u}_i$ are the components of resolved velocity, ρ is density and p pressure. τ_{ij} is the subgrid tensor given by:

$$\tau_{ij} = (\overline{u_i u_j}) - \bar{u}_i\bar{u}_j \tag{4.4}$$

τ_{ij} contains the information form the subgrid scales and is modeled. All other terms in equation 4.2 are dependent on the resolved field only.

4.3.2 Subgrid modeling

There is an increasing number of subgrid models available to close the filtered governing equations. The subgrid model considered in this work is an eddy-viscosity model in which the effect of the unresolved scales is modeled as an enhanced viscosity. This gives:

$$\tau_{ij} - \frac{1}{3}\tau_{kk}\delta_{ij} = -\nu_{sgs}(\frac{\partial \bar{u}_i}{\partial x_j} + \frac{\partial \bar{u}_j}{\partial x_i}) = -2\nu_{sgs}\bar{S}_{ij} \tag{4.5}$$

[29] $\bar{S}_{ij}$ is the rate of strain tensor of the resolved scales. ν_{sgs} is the eddy viscosity or the subgrid viscosity.

Perhaps the most well-known subgrid model is the Smagorinsky eddy-viscosity model. It was proposed by Smagorinsky in 1963 applied to atmospheric flow [87]. The model suggests the relation between the eddy-viscosity and the filtered rate of strain tensor to be:

$$\nu_{sgs} = (C_s\bar{\Delta})^2\sqrt{(2\left|\bar{S}\right|^2)} \tag{4.6}$$

where C_s is a constant to be specified. C_s is commonly between 0.1 and 0.2 [82] and the value used here is 0.17.

The dynamic eddy viscosity method as proposed by Germano in 1991 and later improved by Lilly [30, 59] computes the constant C_s in equation 4.6 as a function of space and time based on information from the smallest resolved scales [30]. A second filter of larger size than the original filter is applied to the governing equations. This gives the subgrid tensor corresponding to the second filtering, τ^*_{ij}.

$$\tau^*_{ij} = \widetilde{\overline{u_i u_j}} - \tilde{\bar{u}}_i\tilde{\bar{u}}_j \tag{4.7}$$

where $(\tilde{*})$ represents second filtered values. Relating the subgrid tensors from the first and the second filtering operations to each other and assuming that they locally can be

modeled by the same constant, an equation that can be solved for the constant C_s is obtained. Lilly [59]proposed a more robust method of solving for the constant than what was originally proposed by Germano. The dynamic Smagorinsky model is employed in this work.

4.3.2.1 Turbulent inlet

Ideally, in order to compare the simulation with experimental data, inflow conditions that mimic those in the experiments are required. Since LES involves solving for the large-scale flow motion, one wants turbulent inlet conditions that can capture the coherent structures of the flow. A way to generate turbulent velocities with prescribed first and second order moments as well as local autocorrelation function is the digital filter method proposed by Klein et al. [50]. The input data are obtained from experimental values. The velocity at a given time and place at the inlet is calculated as

$$u_i = \bar{u}_i + a_{ij} U_j \tag{4.8}$$

Here $\bar{u}_i$ is the mean value and a_{ij} is given as

$$a_{ij} = \begin{bmatrix} \sqrt{R_{11}} & 0 & 0 \\ \frac{R_{21}}{a_{11}} & \sqrt{(R_{22} - a_{21}^2)} & 0 \\ \frac{R_{31}}{a_{11}} & \frac{(R_{32} - a_{21}a_{31})}{a_{22}} & \sqrt{(R_{33} - a_{31}^2 - a_{32}^2)} \end{bmatrix} \tag{4.9}$$

where R_{ij} is the correlation tensor of the fluctuating component of velocity.

$$R_{ij} = \left\langle u_i' u_j' \right\rangle \tag{4.10}$$

U_j in equation 4.8 is a three-dimensional signal with prescribed two point statistics. It is generated by filtering a random field. In the filtering operation a correlation length scale can be specified for each spatial dimension.

4.3.3 Passive scalar transport

The filtered governing equation for transport of a passive scalar is given by

$$\frac{\partial \bar{\phi}}{\partial t} + \bar{u}_i \frac{\partial \phi}{\partial x_i} = D \frac{\partial}{\partial x_i} \left(\frac{\partial \bar{\phi}}{\partial x_i} \right) - \frac{\partial \lambda_i}{\partial x_i} \tag{4.11}$$

where ϕ is the passive scalar, D is the molecular diffusivity and λ_i is the turbulent subgrid scalar flux vector.

$$\lambda_i = \overline{u_i \phi} - \bar{u}_i \bar{\phi} \tag{4.12}$$

λ_i contains information from the subgrid scales, thus equation 4.11 is unclosed. To close the equation one assumes the effect of the subgrid scales to be an enhanced diffusivity. This is analogous to the modeling of the momentum subgrid tensor and gives

$$\lambda_i = -\frac{\nu_{sgs}}{Sc_{sgs}} \frac{\partial \bar{\phi}}{\partial x_i} \tag{4.13}$$

Here Sc_{sgs} is the eddy Schmidt number, usually assumed constant. ν_{sgs} can be computed using any eddy-viscosity model, including dynamic ones.

4.3.4 Implementation

The filtered Navier-Stokes equations are solved on a finite-difference, partial-staggered grid arrangement where velocity is defined at grid nodes and pressure at cell centers. Following Harlow & Welch [40], pressure is decoupled from the momentum equation resulting in an elliptic pressure Poisson equation. The grid is uniform with hexahedron cells. A grid resolution study was performed and the chosen grid has 320x135x100 cells. The spatial scheme is a sixth-order compact scheme proposed by Lele [55] and the time scheme employed is a third-order Runge-Kutta scheme. The solutions to the equations are obtained on a parallel cluster using message passing interface to reduce memory and computing time requirements. Further details on the implementation of the numerical formulation can be found in [32]. The boundary condition at the walls is the no-slip boundary condition. At the exit, a convective outflow boundary condition [27] is used.

For the pressure, a zero normal gradient condition is used at the inflow and at the walls, while at the outlet zero gauge pressure is specified. The previous study by Kong et al. [51] validated the accuracy of using the digital filter methodology to generate the turbulent inlet velocities for employing LES to predict both the pointwise and spatial velocity characteristics of this confined jet flow. Following this study, the digital filter method was the method of choice also here. Simulation parameters and conditions are summarized in table 4.1.

Grid Type	Uniform
Grid Cell Shape	Hexahedron
Grid Cells	320x135x100
Domain Size	300x60x100 mm^3
CFL number	0.6
Subgrid Model	Dynamic Smagorinsky
Time Scheme	3rd order Runge-Kutta
Spatial Scheme Velocity	6th order compact
Spatial Scheme Scalar	2nd order upwind
Inlet Method	Digital filter

Table 4.1: Simulation Parameters

Velocity statistics of the resulting simulation are evaluated by comparison to the PIV results as shown in Figure 4.3. In order to compare the simulation data to the experimental data, results from a plane at the spanwise center of the channel were extracted from the three-dimensional simulation data. The data were normalized by the jet width, d, and the jet excess velocity, U_0.

Figure 4.3a shows the mean streamwise velocity profiles. The mean velocity profile is seen to flatten out as the flow develops and momentum is transferred from the high momentum center stream to the lower momentum side streams. The velocity profile can be expected to eventually approach that of a channel flow, and this trend is indeed seen. The simulation results compare well with the experimental data; however, the simulation profiles develop slightly faster than the experimental profiles, resulting in the maximum velocity value at location x/d = 7.5 to be 3% lower in the simulation than in

the experiments.

The fluctuating component of the streamwise velocity is plotted in Figure 4.3b. The profiles show high values in regions where the velocity gradient is high, namely close to the walls and in free shear regions between the two side streams and the center stream. The peaks of streamwise velocity fluctuations can be seen to decrease with downstream distance, as does the velocity gradient. The simulation results agree well with the experimental data and the peak values are reproduced by the simulation. As with the mean velocity profiles, the simulation profiles develop slightly faster than the experimental results, causing the peaks in the simulation profile to be somewhat broader than the experimental profiles and the minimum values to be larger than the corresponding experimental values.

Figure 4.3c shows the profiles of cross stream velocity fluctuations. Similar to the streamwise velocity fluctuations, the fluctuations of the cross stream velocity peaks in the free shear layer between high momentum and low momentum flow. The peaks have smaller values than the corresponding peaks of the streamwise velocity fluctuations. The rms values by the wall are significantly lower than the rms of streamwise velocity at the same locations. The simulation predicts the development of the cross stream velocity variance profile very well and reproduces the rms levels at the wall as seen in the experimental data. The peaks in the free shear layers are however overpredicted by the simulation, increasing momentum transport in the simulation compared to the experimental flow. This agrees with what was seen in the profiles of mean and fluctuating component of the streamwise velocity, where the simulation profiles were developing (or evening out) faster, indicating higher momentum transfer. The discrepancy between simulation and experiment could originate in the inlet condition for the simulation which is based on experimental data. The PIV measurements of cross stream velocity are relatively more uncertain than the measurements of the streamwise velocity component. This is due to the smaller displacement of the tracer particles in the cross stream direction

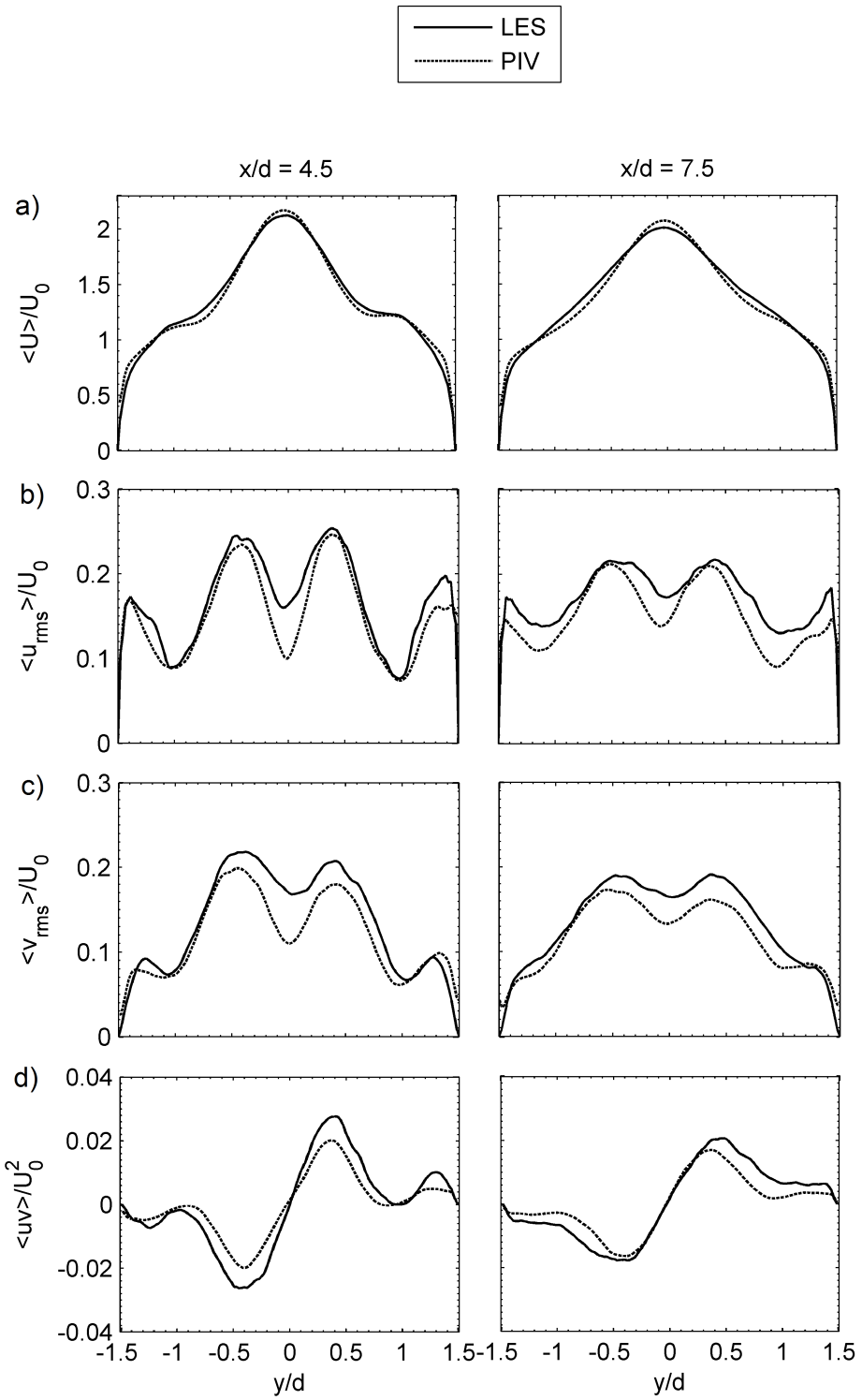

Figure 4.3: Velocity statistics of LES compared to PLIF. a) Mean streamwise velocity. b) Streamwise velocity fluctuations. c) Cross-stream velocity fluctuations. d) Reynolds shear stress.

than in the streamwise direction [48]. Therefore, the cross stream variance level specified at the inlet could deviate from the actual value and thus cause disagreement between simulation and experiment also downstream of the inlet.

The Reynolds shear stress is shown in Figure 4.3d. The profiles are anti-symmetric with maximum magnitude at locations downstream of the splitter plates. These are locations where the magnitude of mean velocity gradient also is high. This trend is well predicted by the simulation. The simulation results give peak value 37% higher than the experimental results at location x/d=4.5 and 22% higher at location x/d=7.5. The Reynolds shear stress is contributing to the spreading of the jet. The overshoot in simulation values therefore agrees with the faster spreading rate of the jet indicated in the mean velocity profiles. This also causes the peaks in Reynolds shear stress to occur at locations slightly further from the center of the channel in the simulation than in the experiment.

Overall, the simulation is predicting the velocity statistics well and only small discrepancies are seen. The successful prediction of the velocity field, as demonstrated, is substantial when simulating passive scalar mixing. The transport equation for the passive scalar is solved using a pseudo finite volume approach to ensure conservation of the scalar. An interpolation step was used to translate the finite difference solution of the velocity field to a form suitable for the finite volume approach where values are defined on the cell faces. The interpolation is done with a second order upwind scheme. Boundary conditions for the passive scalar is zero flux through the walls, and convective outlet. Inlet conditions for the passive scalar are zero in the two outer streams and a value of one in the jet stream.

4.4 Results and Discussion

4.4.1 One-point statistics

Statistics of the velocity and concentration fields predicted by the LES are in this section compared to the experimental data. The comparisons are done across the channel at two downstream locations.

Concentration results are normalized by the concentration in the center incoming stream, ϕ_0, so that at the inlet the mean concentration profile takes a top hat shape with zero values in the side streams and a value of one in the center stream. Figure 4.4 shows the mean concentration profiles at two downstream locations. As can be seen, the profile takes a bell shape which is broadening and flattening with increasing downstream distance. This trend is seen in both the experimental data and the simulation results. The profile flattens out as a result of mixing. The velocity profiles suggested higher mixing rate in the simulation than in the experiment, which would cause the mean concentration profile to flatten out faster in the simulation than in the experiment. This is indeed observed in the mean concentration profiles in Fig. 4.4. The effect is however not strong, and at location x/d = 7.5 the peak concentration value is 7% lower in the simulation than in the experimental data.

The concentration fluctuations, plotted in figure 4.5, show peaks in the shear layers at locations where also the mean concentration gradient and the mean velocity gradient are the highest. The peak locations are further from the jet center than the locations of the peaks in velocity fluctuations. Some discrepancy is seen in the peak values between simulation and experiment, and the simulation gives peak values 21% and 11% higher than the experiment at locations x/d=4.5 and x/d=7.5 respectively. This is again due to the higher mixing rate predicted by the simulation. In this high Schmidt number flow, the transport of the passive scalar is mainly due to convection by the turbulent motion and there is little effect of diffusion. Therefore, when the turbulent velocity fluctuation

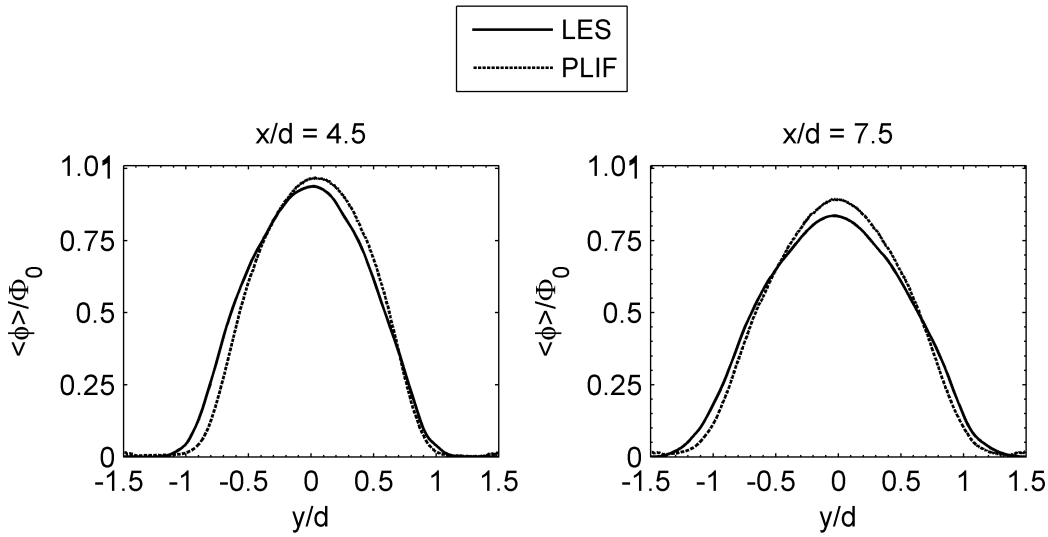

Figure 4.4: Mean concentration.

is overestimated by the simulation, the passive scalar fluctuation follows.

Figures 4.6 and 4.7 show the streamwise and cross-stream turbulent fluxes respectively. It can be seen that the fluxes are high in regions where both the mean velocity gradient and the mean concentration gradient are high. The magnitude of the fluxes in the two directions are comparable. The streamwise turbulent fluxes are positive while the cross-stream turbulent fluxes are anti-symmetric. This is because there are turbulent eddies populating the edges of the jet bringing high momentum and high concentration fluid from the center stream to the side streams, and oppositely low momentum and low concentration fluid from the side streams to the center stream. These observations also agree with what was found by Feng et al. [23] for a higher flow rate. It can be seen that the simulation predicts higher fluxes than what was seen from the experimental data, and the difference is largest on the right side of the let, where the overshoot is about 50%. The discrepancy follows from the higher concentration fluctuations and Reynolds shear stress predicted from the simulation and confirms the suspected higher mixing rates in the simulated flow than in the experimental flow.

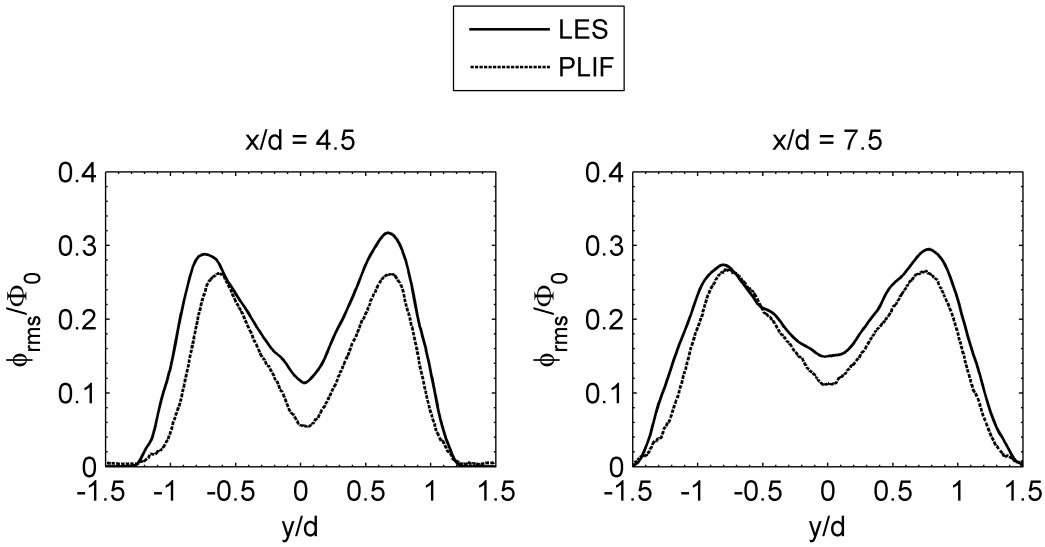

Figure 4.5: Concentration fluctuations.

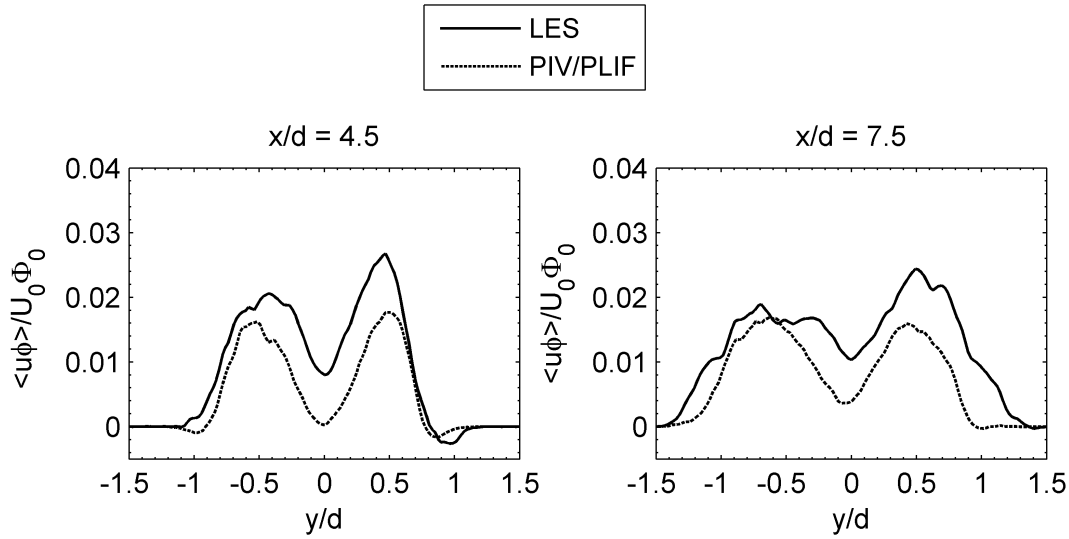

Figure 4.6: Streamwise turbulent flux.

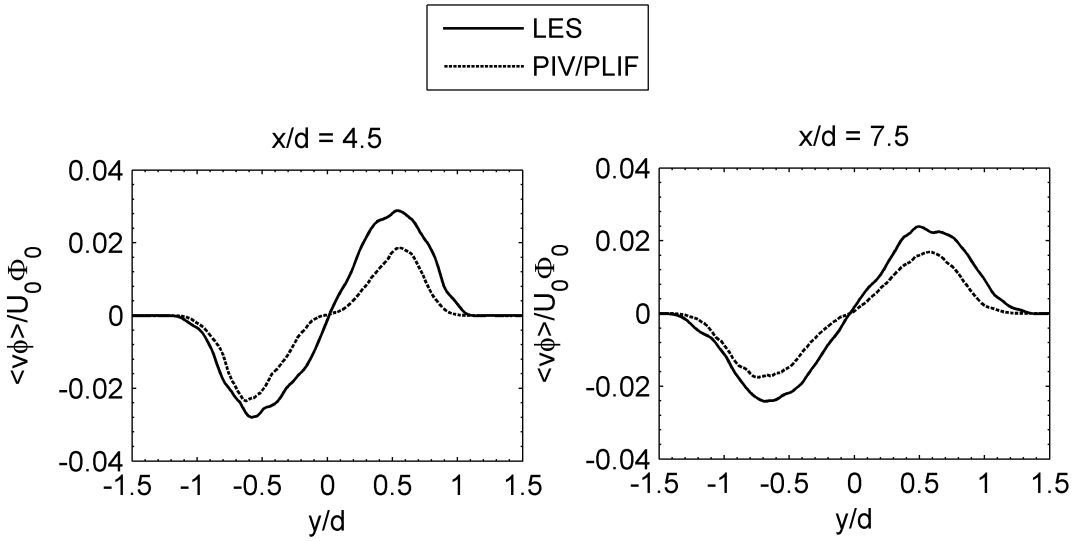

Figure 4.7: Cross-stream turbulent flux.

The turbulent diffusivity tensor, Γ_{ij} can be defined as:

$$\langle u_i' \phi' \rangle = -\Gamma_{ij} \frac{\partial \langle \phi \rangle}{\partial x_j} \tag{4.14}$$

Assuming the streamwise concentration gradient to be negligible, two components of the turbulent diffusivity tensor can be obtained from the planar data:

$$\Gamma_{12} = -\frac{\langle u' \phi' \rangle}{\frac{\partial \langle \phi \rangle}{\partial y}} \tag{4.15}$$

$$\Gamma_{22} = -\frac{\langle v' \phi' \rangle}{\frac{\partial \langle \phi \rangle}{\partial y}} \tag{4.16}$$

Figure 4.8 shows the two components of the turbulent diffusivity tensor, Γ_{12} and Γ_{22}, as computed from the simulation data and compared to the PIV/PLIF results. The profiles of Γ_{12} are anti-symmetric following the anti-symmetric property of the mean concentration gradient. This component of diffusivity takes values near zero close to the walls. Higher magnitudes are seen in the jet region. At the very center of the jet the mean concentration gradient changes sign and therefore Γ_{12} is a little noisy here. The simulation and the experimental data agree well with each other, except at the center of the channel and in the right part of the channel at location x/d=7.5 where

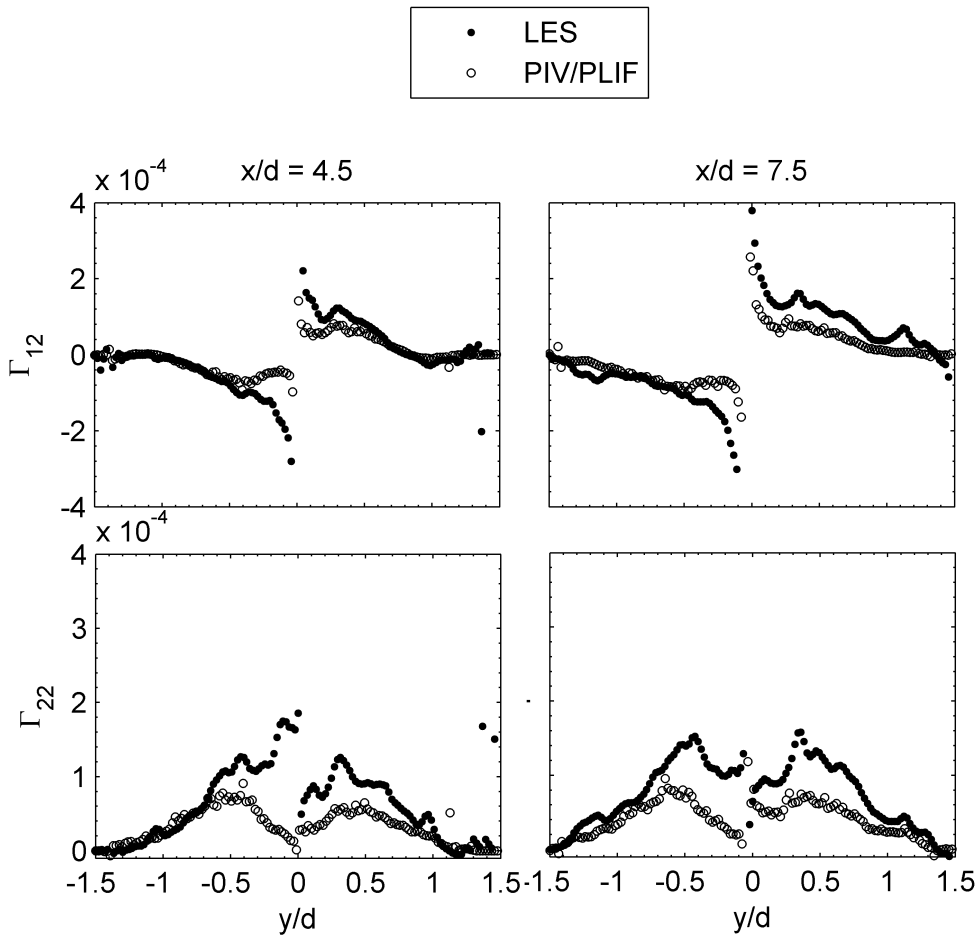

Figure 4.8: The off-diagonal and diagonal component of the turbulent diffusivity tensor, Γ_{12} and Γ_{22}

the simulation gives higher magnitudes than the experiment. The small discrepancy seen in the simulation results is consistent with the small over-prediction of streamwise turbulent flux. The turbulent diffusivity appears in RANS simulations when closing the scalar transport equation using the gradient diffusion hypothesis. Then the turbulent diffusivity is commonly assumed to be a constant scalar. For the turbulent diffusivity to be a scalar, Γ_{12} must be zero. Here it is seen that the off-diagonal component of the turbulent diffusivity tensor is non-zero and that this is predicted by the large-eddy simulation.

The diagonal component of the turbulent diffusivity tensor, Γ_{22} is the component

Tavoularis and Corrsin [91] refers to as the turbulent diffusivity and it corresponds to the turbulent diffusivity when scalar diffusivity is assumed. Γ_{22} is everywhere positive and peaks in the high shear regions of the jet, which is where the mixing mainly takes place, and takes values close to zero by the walls. This is seen both in experiment and simulation. The simulation does, however, predict higher diffusivity value in the center region and also here the discrepancy follows from the higher turbulent flux seen in the simulation results than in the experiment.

The turbulent Schmidt number, Sc_T (not to be confused with Sc_{sgs} in equation 4.13 used in the LES subgrid modeling), is defined as:

$$Sc_T = \frac{\nu_T}{\Gamma_{22}} \tag{4.17}$$

where ν_T is the turbulent viscosity and is here evaluated using:

$$\nu_T = -\frac{\langle u'v' \rangle}{\frac{\partial \langle u \rangle}{\partial y}} \tag{4.18}$$

Sc_T is commonly assumed constant. In figure 4.9 the turbulent Schmidt number is plotted across the channel. In the wall regions and at the center of the channel, the turbulent Schmidt number values are noisy because some or all of $\langle v'\phi' \rangle$, $\frac{\partial \langle \phi \rangle}{\partial y}$, $\langle u'v' \rangle$ and $\frac{\partial \langle u \rangle}{\partial y}$ are close to zero there. In the other parts of the channel the turbulent Schmidt number is indeed quite constant around 0.6-0.8, and this is seen both in the experimental and simulation results.

Knowing the turbulent fluxes and the rms values, the correlation coefficients between velocity and concentration fluctuations can be obtained. The correlation coefficients are defined as:

$$\rho_{u_i\phi} = \frac{\langle u_i'\phi' \rangle}{\sqrt{\langle u_i'^2 \rangle \langle \phi'^2 \rangle}} \tag{4.19}$$

where u_i' are fluctuating components of velocity and ϕ' are concentration fluctuations. These are shown in Figures 4.10 and 4.11 for streamwise and cross-stream velocity respectively. The correlation coefficients are zero by the wall. The correlation coefficient

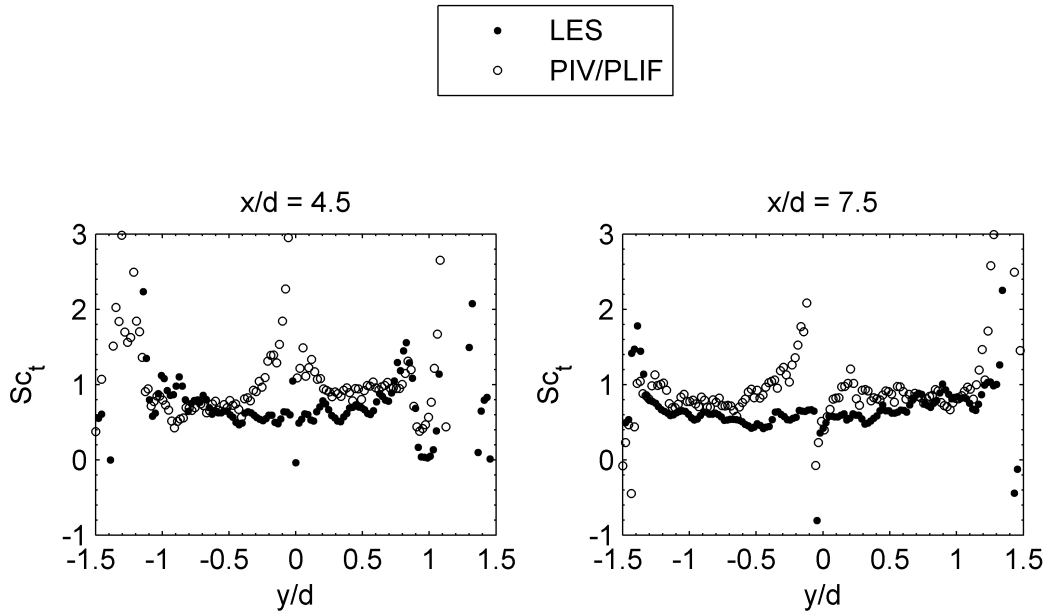

Figure 4.9: Turbulent Schmidt number

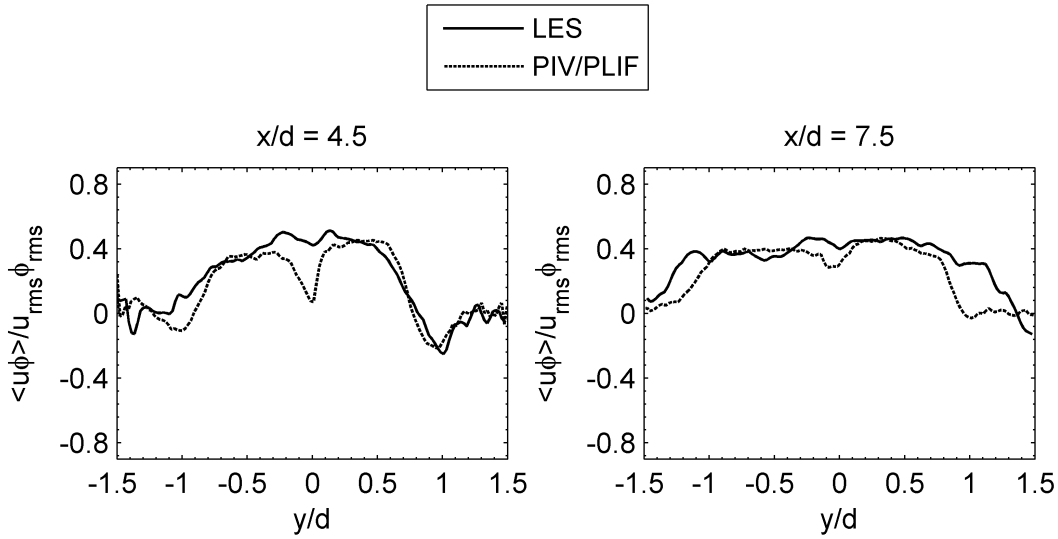

Figure 4.10: Correlation coefficient of streamwise velocity with concentration.

of streamwise velocity with concentration shows positive values across the channel and a profile that flattens out with downstream distance. At location x/d = 4.5 the experimental data show a dip at the center of the channel. This dip is not reproduced by the simulation. This difference could be because the simulation is not giving as low streamwise turbulent flux at the center of the jet as the experiment. Further downstream the profiles agree well with peak values around 0.5. The correlation coefficient for the cross-stream velocity with concentration is anti symmetric as the cross stream turbulent flux is. The peak values of this coefficient are also around 0.5. Here the agreement between simulation and experiment is very good. In a hot-wire experiment on a shear flow with uniform temperature gradient, Tavoularis and Corrsin [91] found the typical value of the correlation coefficient of streamwise velocity and scalar to be 0.59 and the corresponding magnitude of in the cross-stream direction 0.45. The magnitudes of the correlation coefficients measured by Tavoularis and Corrsin are comparable to those found here.

The correlation coefficient corresponding to the turbulent shear stress is shown in figure 4.12. These profiles are anti-symmetric with peak values of 0.5. The values at the wall are not zero in this case but close to 0.5. The simulation predicts the correlation

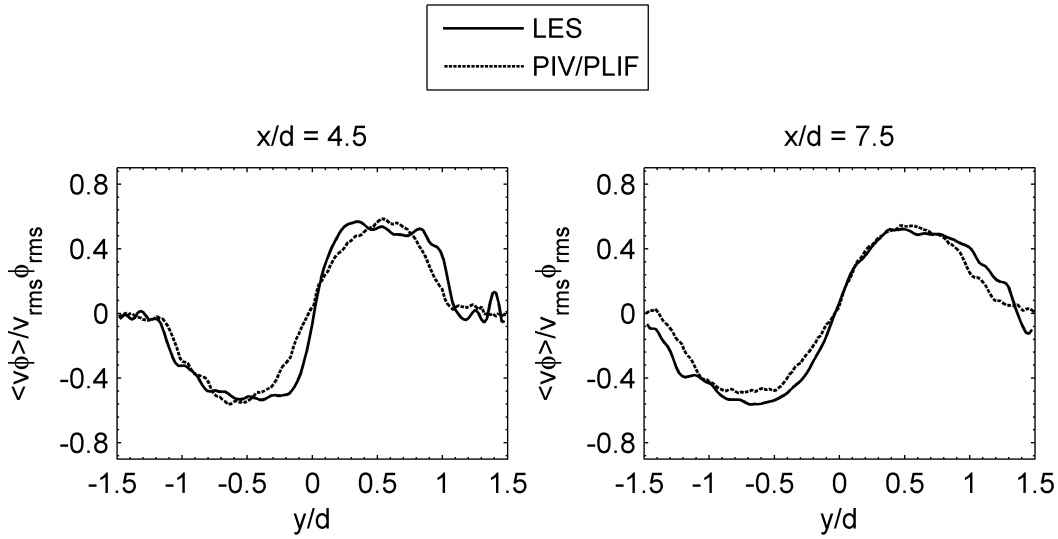

Figure 4.11: Correlation coefficient of cross-stream velocity with concentration.

coefficient accurately except for a dip in the coefficient for x/d=7.5 near y/d=1 that is observed in the experimental results but not in the simulations.

4.4.2 Two-point spatial correlations

One of the advantages of LES over RANS is that LES provides information about the turbulent coherent structures of the flow. It is therefore very beneficial to have spatial PIV and PLIF data to validate this structure information. This can be done through comparison of the two-point spatial correlations of velocity and concentration. The two-point auto correlation of concentration is described by:

$$R_{\phi\phi}\left(\boldsymbol{x},\boldsymbol{X}\right) = \frac{\left\langle \phi'\left(\boldsymbol{x}\right)\phi'\left(\boldsymbol{X}\right)\right\rangle}{\sqrt{\left\langle \phi'^2\left(\boldsymbol{x}\right)\right\rangle\left\langle \phi'^2\left(\boldsymbol{X}\right)\right\rangle}} \tag{4.20}$$

and the two-point spatial cross-correlation of velocity and concentration is described by:

$$R_{u_i\phi}\left(\boldsymbol{x},\boldsymbol{X}\right) = \frac{\left\langle u_i'\left(\boldsymbol{x}\right)\phi'\left(\boldsymbol{X}\right)\right\rangle}{\sqrt{\left\langle u_i'^2\left(\boldsymbol{x}\right)\right\rangle\left\langle \phi'^2\left(\boldsymbol{X}\right)\right\rangle}} \tag{4.21}$$

where $\boldsymbol{x}$ is the vector of spatial coordinates and $\boldsymbol{X}$ is the position vector of the basis point (the point about which the correlation is taken). The location of the basis point for correlation was determined based on the peaks of concentration fluctuation. In the

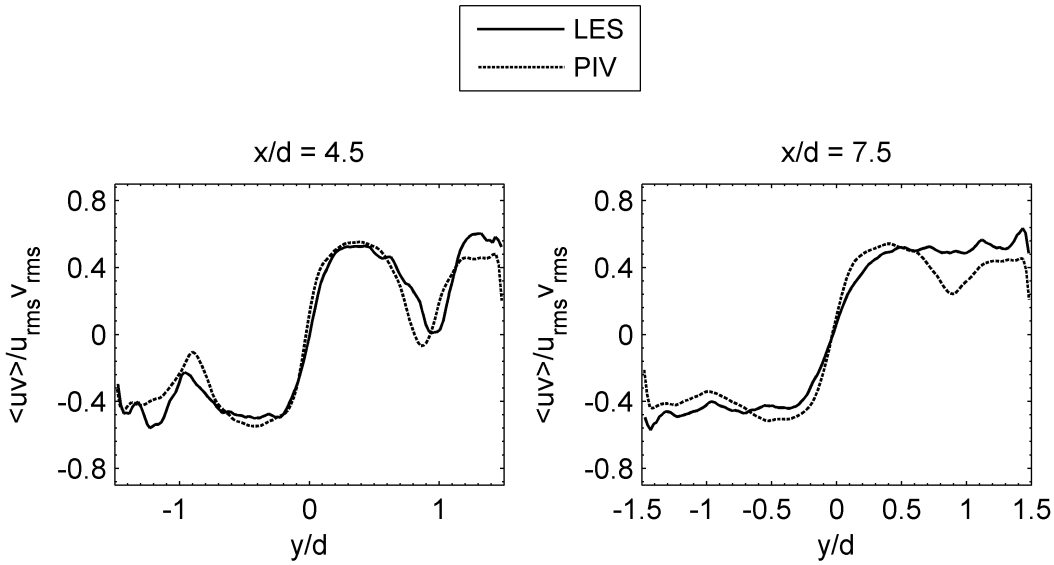

Figure 4.12: Correlation coefficient of streamwise velocity with cross-stream velocity.

following, results from the right side of the jet are shown. The basis point is marked by a white star and the color contours are simulation results while the black line contours are experimental data. Figure 4.13 shows the locations of the basis points in the flow field.

Figure 4.14 shows the two-point auto-correlation of concentration at two downstream locations. The normalized correlation value is one in the basis point and decays with distance from the basis point. The correlation contours are elliptic in shape with an inclined axis due to the shearing action of the mean velocity gradient. The size of the correlation area grows with downstream distance, an observation consistent with turbulent structures growing with downstream distance. The simulation reproduces the correlation shape and magnitude very accurately.

The two-point cross-correlation between concentration in the basis point and streamwise velocity is displayed in Figure 4.15. At location x/d = 4.5 a positively correlated region can be seen to the left and slightly downstream of the basis point stretching downstream of the correlation point and towards the side stream. Oppositely, a negatively correlated region is seen to the right and upstream of the basis point and this is stretch-

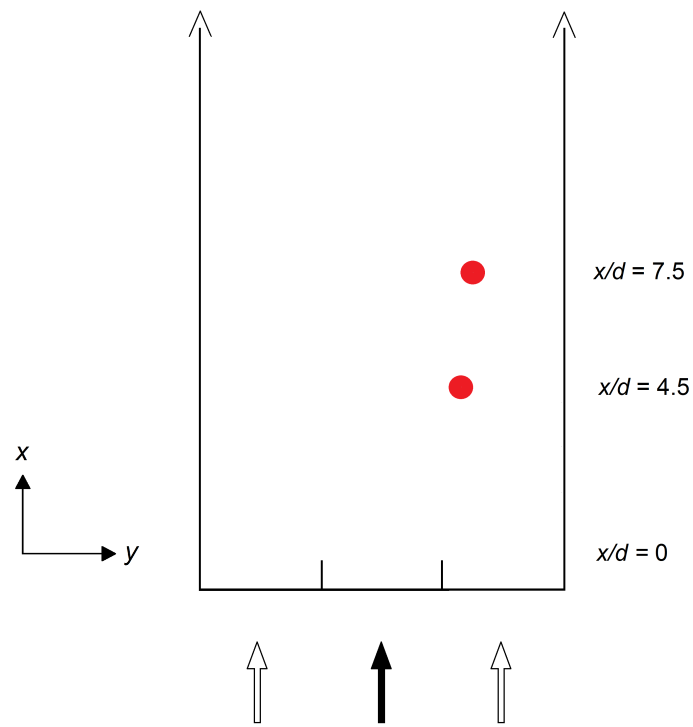

Figure 4.13: Basis points of the two-point correlations.

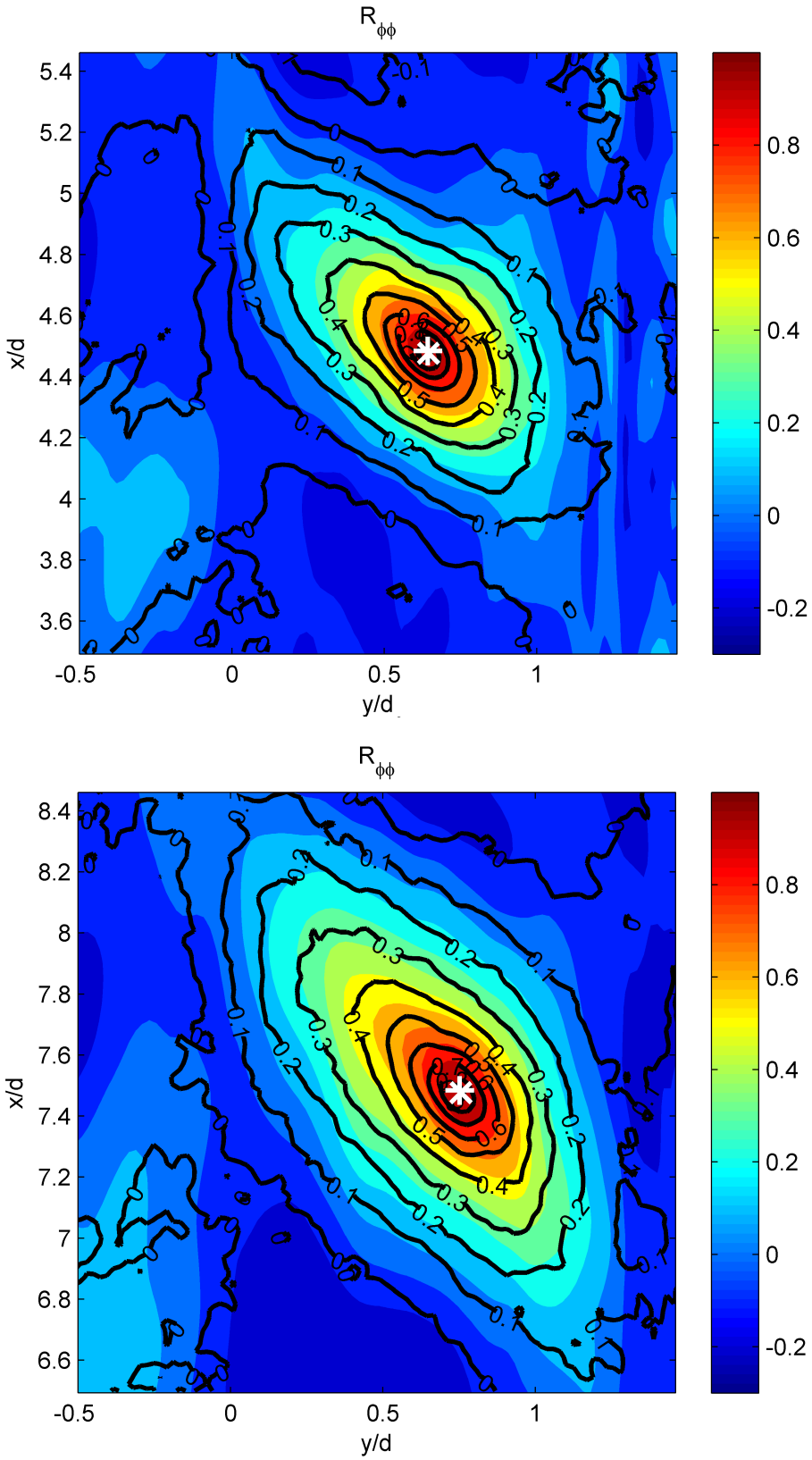

Figure 4.14: Two-point spatial auto-correlation of concentration.

ing upstream and towards the jet center. This cross-correlation field is characteristic of a vortex street. To understand the reason for the presence of a vortex street, one must recall that the turbulent jet is formed by bringing three fluid streams together downstream of the splitter plates. Boundary layers for on each surface of the splitter plate, and thus, just downstream of the splitter plate, a wake forms due to the merging of the boundary layers, resulting in a vortex street. This vortex street decays, but is still evident in the cross-correlation field at x/d=4.5. Indeed, the cross-correlation field observed at x/d=4.5 is reminiscent of similar cross-correlation results measured in simultaneous PIV/PLIF measurements in a pure wake flow in this reactor [24], the main difference being the positively correlated region due to the mean shear in the flow. In the pure wake flow, the positively and negatively correlated regions occurred at the same downstream location due to the absence of mean shear in the wake flow. The patterns are very well reproduced by the simulation, indicating that the turbulent coherent structures are predicted by the simulation. Further downstream, at x/d=7.5 the correlation region is larger, while the region of anti-correlation is weakened, due to the disappearance of the vortex street.

Correlating the concentration in the basis point with the cross-stream velocity gives the results shown in Fig. 4.16. Again we see a positive and a negative region, but this time upstream and downstream of the basis point. The positively correlated region shows how a positive cross-stream fluctuation brings high concentration fluid from the center stream to the side stream while a negative fluctuation brings low concentration from the side stream to the center stream. The anti-correlations support the idea of eddy motion. The magnitude of the anti-correlation is smaller than that of the positive correlation. These trends are seen both in the experiment and simulation.

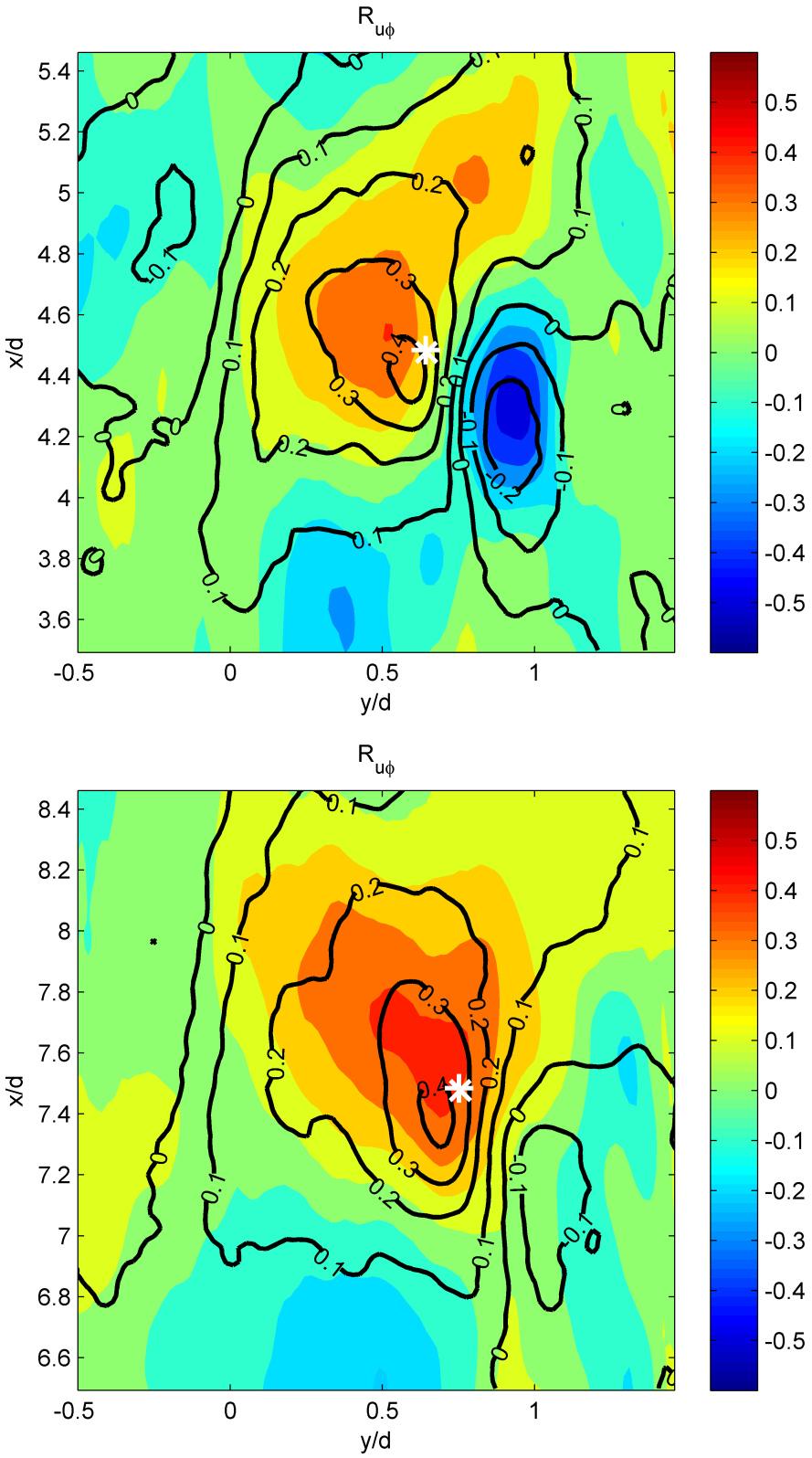

Figure 4.15: Two-point spatial cross-correlation of concentration in basis point with streamwise velocity.

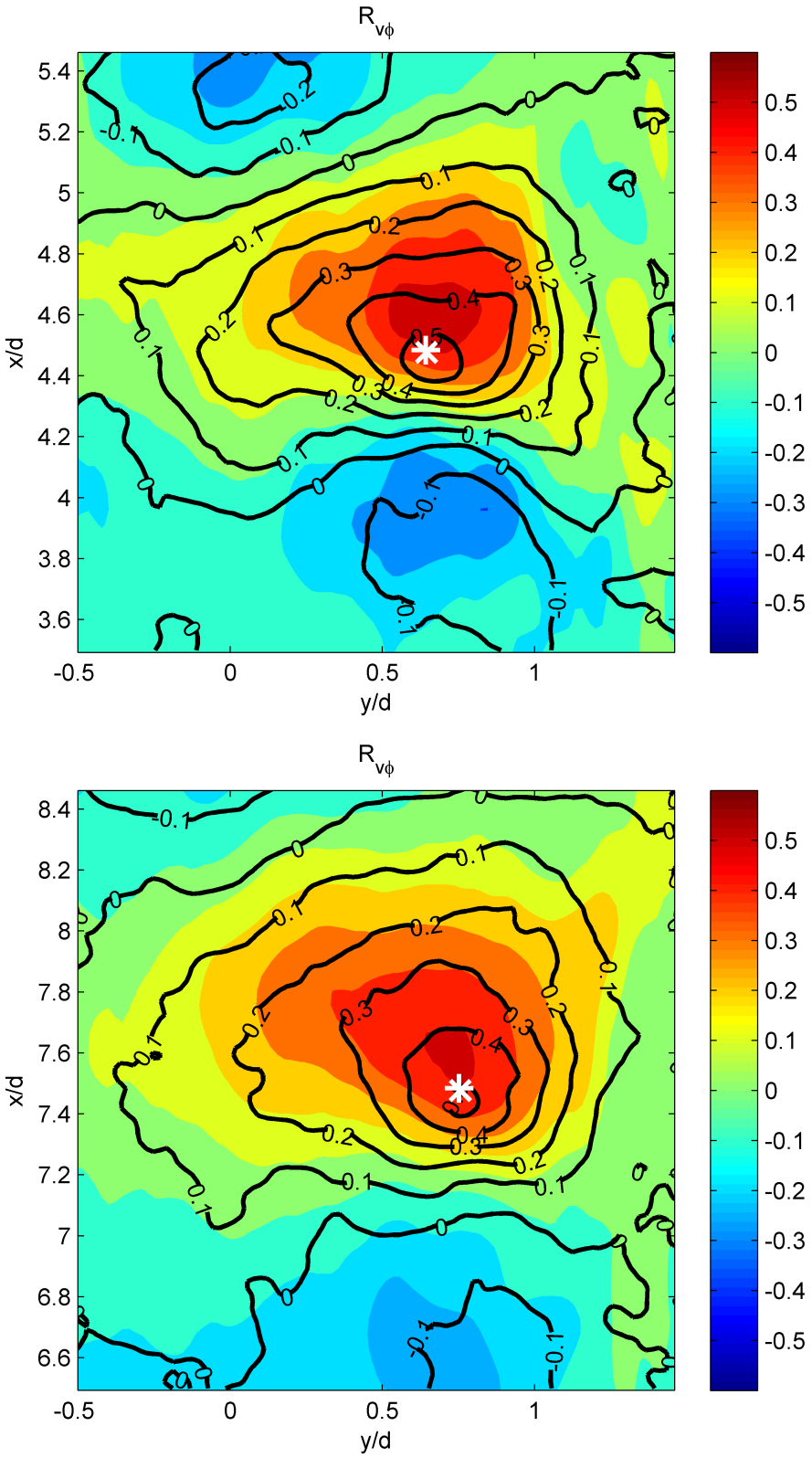

Figure 4.16: Two-point spatial cross-correlation of concentration in basis point with cross-stream velocity.

4.5 Summary and Conclusions

Transport of a passive scalar in a turbulent rectangular jet with co-flow was studied using LES. The results were validated with simultaneous PIV/PLIF measurements for the same flow.

The resolved velocity field was computed on a finite-difference, partially staggered grid. The dynamic Smagorinsky model was used to account for the effect of the unresolved scales. To generate turbulent inlet velocities, a digital filter method based on experimental data was used. The gradient-diffusion hypothesis was used to model the passive scalar transport. To guarantee conservation of the passive scalar, a finite volume approach with second order upwind numerical scheme was employed.

It was found that the simulation was able to predict the main features of the flow. One-point statistics like mean and fluctuating component of velocity and concentration showed good agreement between simulation and experiment. Also the transport related quantities turbulent diffusivity and turbulent Schmidt number were quite well predicted by the simulation. Small discrepancies between simulation and experimental data were attributed to a slightly higher mixing rate predicted by the simulation than what was measured in the experiments. This caused the simulated velocity and concentration fluctuations as well as the turbulent fluxes to be higher than the corresponding experimental values. A plausible explanation for the discrepancies seen is the higher uncertainty in the cross-stream velocity measurements combined with the fact that simulated mixing rate is highly dependent on the cross-stream velocity component. Another issue is the eddy Schmidt number Sc_{sgs}, which is assumed constant. The gradient-diffusion hypothesis also has some weaknesses and perhaps the mixing rate could be improved by using a more detailed turbulent diffusivity tensor.

The two-point spatial correlations of concentration and velocity revealed vortex motion in the free shear layer. The simulation contours showed very good agreement with

the experimental results. This indicates that the method very well can capture the coherent structures of the flow.

CHAPTER 5. CROSS-GRADIENT TURBULENT SCALAR TRANSPORT IN A RECTANGULAR JET WITH CO-FLOW

A paper in preparation

Katrine M. Nilsen[1], Bo Kong, Rodney O. Fox,
Michael G. Olsen and James C. Hill[2]

Abstract

A turbulent confined jet with co-flow and passive scalar transport at Reynolds numbers 20,000 and 50,000 was investigated. Simultaneous PIV/PLIF data and results of LES with passive scalar transport were studied with particular regards to cross-gradient transport. It was found that the turbulent flux was not aligned with the mean concentration gradient and that this was true for both Reynolds numbers. Turbulent diffusivities were also compared and found to vary little across Reynolds numbers. The simulation proved to be able to predict the mis-alignment of turbulent flux and concentration gradient very well.

5.1 Introduction

Turbulent mixing of a passive scalar is a phenomenon of importance for a wide range of areas, including meteorology, chemical process industry, combustion applications, en-

[1]Primary researcher and author
[2]Corresponding author

vironmental considerations and fundamental research. Therefore, this highly complex phenomenon has long been subject to extensive research. The topic has been comprehensively discussed in recent review articles such as [98] and [18], where it is made clear that the process of turbulent transport is not yet fully understood. Modeling of turbulent passive scalar transport suffers from this lack of understanding, and therefore further research is necessary in order to improve the models.

A passive scalar is a scalar, such as concentration of a contaminant or temperature in a weakly heated flow, that is transported with the flow but has no effect on the fluid motion, e.g. no buoyancy effects.

Transport of passive scalar in turbulent shear flows is relevant in many mixing situations such as jet flames and plumes. Turbulent jet flows have a long research tradition, both because of their canonical form but also because of their numerous applications [5, 78]. In the turbulent jet the turbulence contributes to transport of momentum, energy and the passive scalar. It is well established that large-scale turbulent coherent motion plays a major role in the jet mixing process, see for example [19, 16, 99, 33].

An important aid in the study of passive scalar transport in turbulent flows is the simultaneous measurement of velocity and concentration/temperature. One of the early such studies was reported by Tavoularis and Corrsin [91]. They studied a weakly heated homogeneous turbulent shear flow with constant and parallel mean velocity and temperature gradients. Using hot and cold wires they measured point-wise velocity and temperature instantaneously and were able to evaluate transport coefficients of the passive scalar (temperature). A slightly heated plane air jet was studied by Antonia et al. [4] who also used hot and cold wires to measure simultaneous velocity and temperature. They were able to evaluate the terms in the budget equation of the temperature variance. Non-intrusive methods for simultaneous velocity and passive scalar measurements were later developed. For example, Lemoine et al. [56] used combined laser-induced fluorescence (LIF) and laser Doppler anemometry (LDA) to measure simultaneous point-wise

velocity and temperature in a circular heated water jet with co-flow at a Reynolds number of 9000. Turbulent fluxes as well as turbulent Prandtl number and turbulent diffusivities in axial and radial directions were computed.

Although very informative, experiments measuring velocity and scalar *fields* simultaneously are less common. Borg et al. [6] employed particle image velocimetry (PIV) and planar laser-induced fluorescence (PLIF) simultaneously on a submerged circular water jet at Reynolds number 6000. They used the measurement data to compute axial and radial turbulent fluxes as well as turbulent transport coefficients for the scalar. Simultaneous PIV/PLIF was also performed by Feng et al. [23] on a liquid rectangular jet with co-flow at Reynolds number 50,000. Turbulent fluxes as well as turbulent viscosity, diffusivity and Schmidt number were evaluated.

Modeling of turbulent transport of a passive scalar is a challenging task, but nonetheless very attractive and many attempts have been made. Being able to predict the transport of a passive scalar in turbulent flows is beneficial both in industrial context for design, optimization and scale-up processes as well as for academic purposes of gaining fundamental understanding of the process. The prediction of turbulent transport of a passive scalar is also the first step towards being able to predict turbulent chemically reacting flows accurately. The transport of a passive scalar in fluid flows is governed by:

$$\frac{\partial \phi}{\partial t} + u_i \frac{\partial \phi}{\partial x_i} = D \frac{\partial}{\partial x_i} \left(\frac{\partial \phi}{\partial x_i} \right) \tag{5.1}$$

where ϕ is the passive scalar, t is time, u_i are components of velocity and x_i are the spatial coordinates. D is the diffusivity of the passive scalar. Although the governing equation is known, its solution is difficult to obtain in high Reynolds number cases because of the wide range of scales present in the flow. Solving the equation directly is therefore only possible for simple geometries and limited range of Reynolds numbers.

The Reynolds-averaging approach to modeling the transport of a passive scalar is to solve for the Reynolds averaged passive scalar and to model the turbulent flux terms,

$\langle \phi u_i \rangle$, that appear when averaging equation 5.1.

$$\frac{\partial \langle \phi \rangle}{\partial t} + \langle u_i \rangle \frac{\partial \langle \phi \rangle}{\partial x_i} = D \frac{\partial}{\partial x_i} \left(\frac{\partial \langle \phi \rangle}{\partial x_i} \right) - \frac{\partial \langle u_i' \phi' \rangle}{\partial x_i} \tag{5.2}$$

Here and in the following $\langle * \rangle$ represents ensemble averaged quantities. A commonly used assumption is the gradient-diffusion hypothesis which assumes that turbulent mixing is analogous to molecular mixing and gives:

$$\langle u_i' \phi' \rangle = -\Gamma_{ij} \frac{\partial \langle \phi \rangle}{\partial x_j} \tag{5.3}$$

where u_i' and ϕ' are the fluctuating components of velocity and concentration, respectively, and are given by $u_i' = u_i - \langle u_i \rangle$ and $\phi' = \phi - \langle \phi \rangle$. Γ_{ij} is the turbulent diffusivity tensor, but it is usually assumed to be a constant scalar; the turbulent diffusivity Γ. This assumption is, however, in several studies found to be invalid. For example, Tavoularis and Corrsin [91] found that the turbulent diffusivity was not a scalar and also not a diagonal tensor in their shear flow. In the turbulent heated round jet of Lemoine et al. [56], it was found that the streamwise, cross-gradient flux was actually larger than the transverse turbulent flux. In the submerged round jet investigated by Borg et al [6], the turbulent diffusivity was found to vary with position and direction. Feng et al. [23] found an off-diagonal component of the turbulent diffusivity tensor in the confined rectangular jet with co-flow to be non-zero and that the turbulent flux vector was not aligned with the mean concentration gradient, as it would be in the case of scalar turbulent diffusivity. Also in that flow, the streamwise turbulent flux was found to be larger than the cross-stream turbulent flux.

An approach to modeling of passive scalar turbulent transport which has potential to overcome the issue of non-scalar turbulent diffusivity is large eddy simulation (LES). This method solves for the larger scales of the flow while modeling the effect of the small scales. The separation of scales is achieved through filtering of the governing equations. The resulting governing equation for the resolved scales of the passive scalar is:

$$\frac{\partial \bar{\phi}}{\partial t} + \bar{u}_i \frac{\partial \bar{\phi}}{\partial x_i} = D \frac{\partial}{\partial x_i} \left(\frac{\partial \bar{\phi}}{\partial x_i} \right) - \frac{\partial \lambda_i}{\partial x_i} \tag{5.4}$$

where $(\bar{*})$ represents filtered values and λ_i is the turbulent subgrid scalar flux vector.

$$\lambda_i = \overline{u_i\phi} - \bar{u}_i\bar{\phi} \tag{5.5}$$

The subgrid scalar flux vector is based on unresolved scales and must be modeled. Assuming the effect of the subgrid scales is an enhanced diffusivity gives:

$$\lambda_i = -\frac{\nu_{sgs}}{Sc_t}\frac{\partial\bar{\phi}}{\partial x_i} \tag{5.6}$$

Here Sc_t is the eddy Schmidt number which is usually assumed constant. This is essentially also a way of employing the gradient diffusion hypothesis, however in a different framework. The question is whether this model can reproduce the turbulent diffusivity tensor, Γ_{ij}, as measured in experiments.

In this work, the turbulent transport of a passive scalar in a jet with co-flow is investigated using simultaneous PIV/PLIF data at two Reynolds numbers as well as LES results. The aim is to use the simultaneously measured velocity/scalar data to gain understanding of the transport process in the jet. Quantities important in turbulent scalar transport, such as turbulent diffusivity and orientation of turbulent fluxes are computed. The predictive quality of LES with regards to turbulent transport is evaluated.

5.2 Methodology

The experimental and the numerical method of the jet at Reynolds number 20,000 have previously been described in Chapter 4. A brief description of the procedures is included here for reference. For details on the experimental data of the jet at Reynolds number 50,000, refer to [23].

5.2.1 Simultaneous PIV/PLIF

The confined jet is produced in a rectangular channel of cross section 6x10 cm and overall length 1 m. The channel has three inlets, separated by two thin splitter plates so

that the width of each inlet is 2 cm. The flow rate of the inlet streams can be controlled separately. The flow rate of the center stream is set to twice the flow rate of each of the co-flowing side streams.

Further details about the experimental method and facility can be found in [23].

5.2.1.1 Particle Image Velocimetry

The PIV measurements of instantaneous velocity fields were made in a planar cross section of the channel at its spanwise center. All three inflowing streams were seeded with hollow glass spheres with a nominal diameter of 11.7 μm and a density of 1.1 g/cm^3. A pulsating light sheet was produced at the spanwise center plane of the channel by a double-pulsed Nd:YAG New Wave Research Gemini PIV laser. The laser lightwave length is 532 nm, the maximum pulse energy is 120 mJ and the pulse duration is about 5 ns. The particle images were captured using a 12-bit LaVision Flowmaster 3S CCD camera with a resolution of 1280x1024 pixels. The image magnification was 0.12 and the numerical aperture was 8. A time delay of 600 μs between two laser pulses was used. A cross-correlation technique with multi-pass interrogation scheme and decreasingly smaller window sizes was applied to obtain velocity fields. Using a 50% overlap between adjacent interrogation windows the final interrogation window size measured 16 pixels by 16 pixels.

5.2.1.2 Planar Laser-Induced Fluorescence

The PLIF measurements were obtained using the fluorescent dye Rhodamine 6G which in water has a Schmidt number of 1250 [15]. The dye was added to the center stream giving a concentration of 45 μg/l. When illuminated by the 532 nm laser light, Rhodamine 6G fluoresces with a peak emission wavelength of 555 nm. A second Flowmaster 3S CCD camera was used to capture the fluorescent light. The image magnification of the PLIF measurements was 0.12, and the numerical aperture was 5.6. The images were corrected for spatial illumination intensity variation and gray offset values.

A dichroic mirror was placed between the channel and the cameras in order to direct the PIV and PLIF lights to their respective cameras. The two cameras were aligned so that the coordinates from the PIV and the PLIF measurements were identical. 2500 instantaneous data sets were captured at two downstream locations using a frame rate of 1 Hz.

5.2.2 Large eddy simulation

The LES approach is to solve a filtered set of Navier-Stokes equations where the resolved scales are solved for while the effect of the unresolved scales are modeled. The equations take the form:

$$\frac{\partial \bar{u}_i}{\partial t} + \frac{\partial}{\partial x_j}(\bar{u}_i\bar{u}_j) = -\frac{1}{\rho}\frac{\partial \bar{p}}{\partial x_i} + \nu\frac{\partial}{\partial x_j}(\frac{\partial \bar{u}_i}{\partial x_j} + \frac{\partial \bar{u}_j}{\partial x_i}) - \frac{\partial \tau_{ij}}{\partial x_j} \tag{5.7}$$

$$\frac{\partial \bar{u}_i}{\partial x_i} = 0 \tag{5.8}$$

$\bar{u}_i$ are the components of resolved velocity, ρ is density and p pressure. τ_{ij} is the subgrid tensor given by:

$$\tau_{ij} = (\overline{u_i u_j}) - \bar{u}_i\bar{u}_j \tag{5.9}$$

It is through τ_{ij} that the effect of the subgrid scales enter into the governing equations. τ_{ij} therefore needs to be modeled. The subgrid model employed in this work was the dynamic Smagorinsky model. It gives:

$$\tau_{ij} - \frac{1}{3}\tau_{kk}\delta_{ij} = -\nu_{sgs}(\frac{\partial \bar{u}_i}{\partial x_j} + \frac{\partial \bar{u}_j}{\partial x_i}) = -2\nu_{sgs}\bar{S}_{ij} \tag{5.10}$$

[29] $\bar{S}_{ij}$ is the rate of strain tensor of the resolved scales. ν_{sgs} is the eddy viscosity or the subgrid viscosity which is computed using:

$$\nu_{sgs} = (C_s\bar{\Delta})^2\sqrt{(2\left|\bar{S}\right|^2)} \tag{5.11}$$

C_s is a dynamic constant evaluated through the dynamic procedure of Germano and Lilly [30, 59] where a second filter of larger size than the original filter is applied to the

governing equations. This gives the subgrid tensor corresponding to the second filtering, τ^*_{ij}.

$$\tau^*_{ij} = \widetilde{\overline{u_i u_j}} - \tilde{\bar{u}}_i \tilde{\bar{u}}_j \tag{5.12}$$

$(\tilde{*})$ represents values from the second filtering. The subgrid tensors from the first and the second filtering operations can then be related to each other. By assuming that the same value of the model constant is valid for both subgrid tensors locally, an equation that can be solved for C_s, is obtained.

5.2.3 Implementation

The finite-difference method and a partial-staggered grid arrangement was used to solve the filtered Navier-Stokes equations, equation 5.7, with the dynamic Smagorinsky model. Pressure was decoupled from the momentum equation giving an elliptic pressure Poisson equation. Velocity was defined at grid nodes and pressure at cell centers. The time scheme employed was a compact third-order Runge-Kutta scheme. Further details on the implementation of the numerical formulation can be found in [32]. The evolution of the passive scalar was predicted by solving the transport equation for the passive scalar, equation 5.4 with 5.6. In order to conserve the scalar, a finite volume approach was used.

At the walls a no-slip boundary condition was used and at the exit a convective outflow boundary condition [27] was used. Turbulent inlet conditions were generated using the digital filter method of Klein et al. [50] based on experimental values at the inlet. The boundary conditions for the pressure were zero normal gradient at the inlet and at the walls, and zero gauge pressure at the outlet. For the passive scalar, the boundary conditions were zero flux through the walls and convective outlet. At the inlet the passive scalar is set to zero in the two outer streams and one in the jet stream.

5.3 Results and discussion

The data from the experiment and simulation of the jet at Reynolds number 20,000 are analyzed and compared. The results are also compared to the experimental data at Reynolds number 50,000 from Feng et al. [23].

The data are normalized using the difference in bulk velocity between the jet and the co-flow, U_0, the jet width, d, and the jet inlet concentration, C_0.

The coordinate system used has x increasing in the streamwise direction, y in the cross-stream direction with zero in the center of the channel, and z being the spanwise direction. The data are taken at the spanwise center of the channel at two downstream locations; $x/d = 4.5$ and $x/d = 7.5$.

5.3.1 Mean velocity and concentration profiles

The mean and variance of velocity and concentration data have been presented separately in [25, 51] and in Chapter 4. Here, the profiles are compared.

The mean velocity profiles are shown in figure 5.1. The jet bulk velocity at the inlet is set to be two times the inlet bulk velocity of the co-flowing stream. It is seen from the figure that the center stream at locations $x/d = 4.5$ and $x/d = 7.5$ has higher velocity than the side streams, but that the profile is evening out as the flow develops downstream and momentum is transported. The results from the two different Reynolds numbers almost collapse when normalized by their respective U_0 value. The agreement between simulation and experiment is also seen to be very good.

The root-mean-square (RMS) of velocity is a measure of how much the velocity is fluctuating. Comparisons of RMS of streamwise and cross-stream velocity are shown in figure 5.2 and 5.3, respectively. Both peak in the high shear regions between the jet and the co-flowing streams. Smaller peaks are also visible in the shear region close to the walls. The peakvalues decrease rapidly with downstream distance. It is apparent that

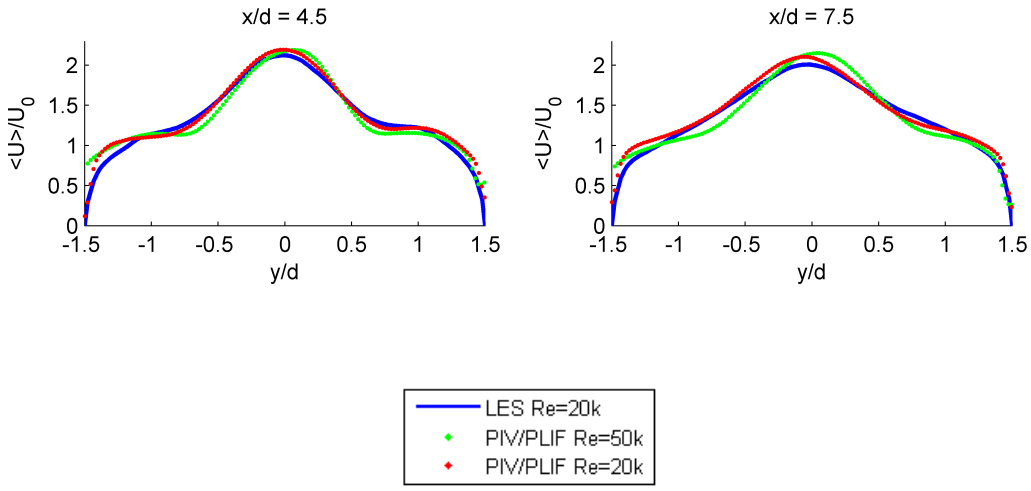

Figure 5.1: Mean velocity profiles at two downstream locations.

the higher Reynolds number case gives relatively lower velocity RMS, especially in the cross-stream case. It is here important to note that the normalizing velocity, U_0, is larger for the higher Reynolds number case; in absolute value, the high Reynolds number gives higher fluctuations than the lower Reynolds number.

The mean concentration is a top hat profile at the inlet since the co-flowing streams do not contain dye and the incoming jet stream has a uniform concentration of dye. As the flow develops and dye is transported, the top hat profile flattens out. This is seen in figure 5.4. One could imagine that the higher Reynolds number jet would be less developed at the given locations, considering that the location is based on jet width, which is the same for the two jets. This is indeed seen in the figure, the profile for Reynolds number 50,000 is steeper and narrower than for the Reynolds number of 20,000 case. The agreement between simulation and experiment is good.

Figure 5.5 displays RMS of concentration. Also the concentration has the most fluctuations in the shear regions between jet and co-flowing streams. This is also where the concentration gradient is at its largest. The higher Reynolds number jet gives lower RMS of concentration and the RMS peaks more centered than for the lower Reynolds

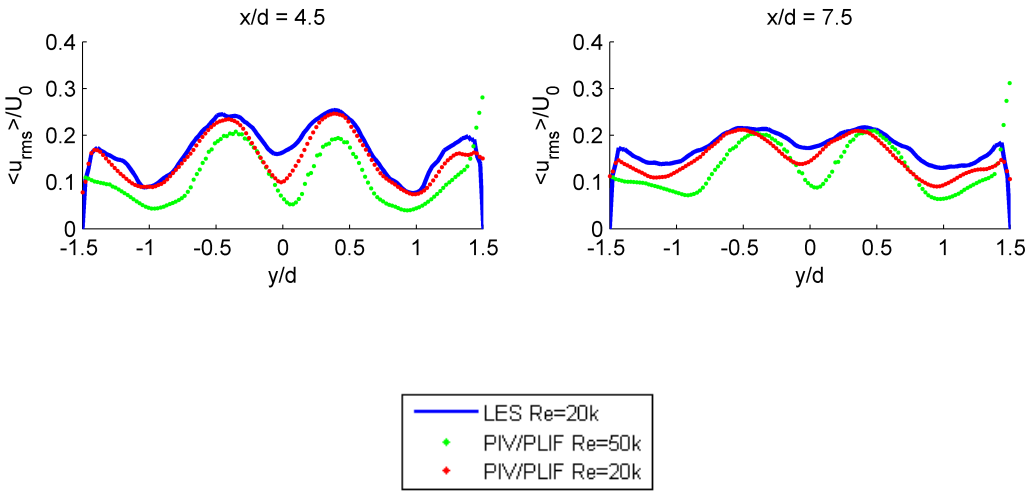

Figure 5.2: RMS of streamwise velocity.

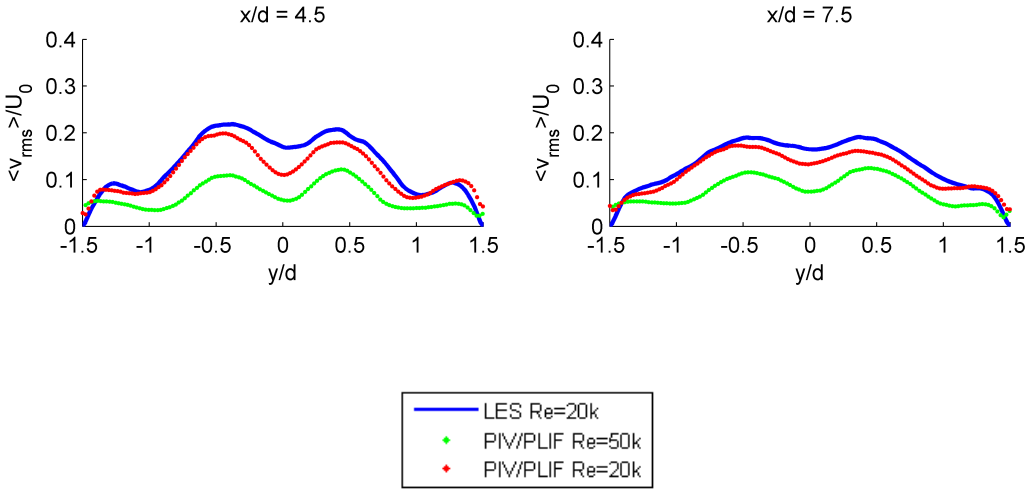

Figure 5.3: RMS of cross-stream velocity.

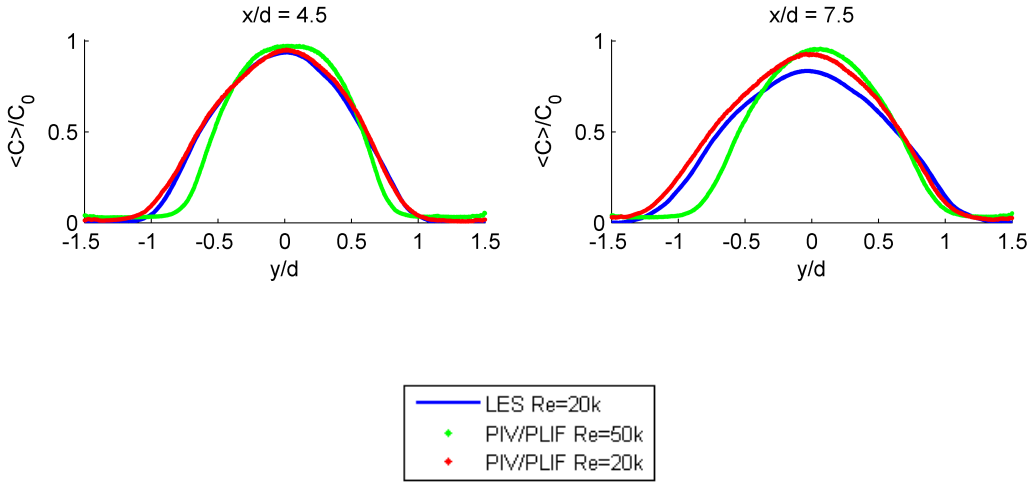

Figure 5.4: Mean concentration profiles

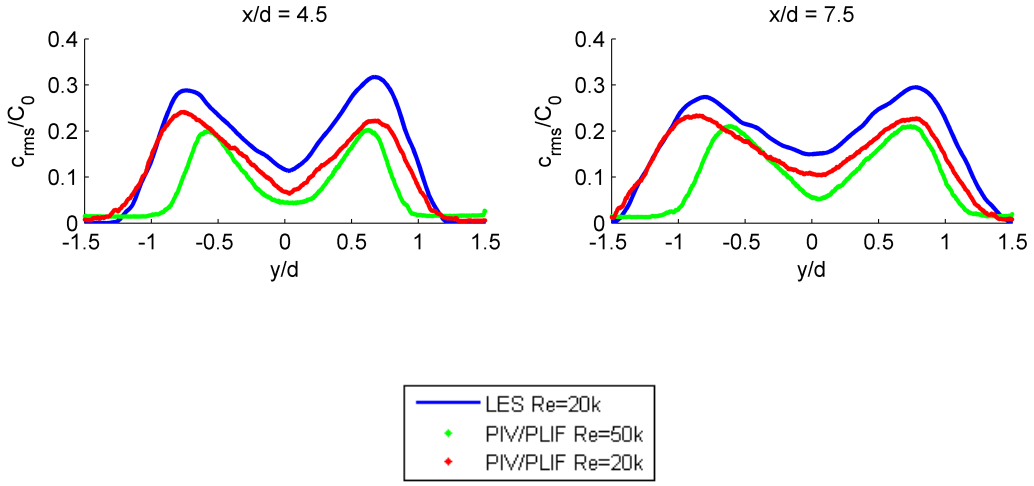

Figure 5.5: RMS of concentration

number case. This agrees with the idea of slower development respective to downstream distance of the higher Reynolds number jet. It must here be noted that as opposed to what is the case with the velocity values, there is here no difference in the normalizing value, C_0, between the different Reynolds number cases. The simulation produces higher concentration RMS than what is seen in the experimental data.

Using the definition of the turbulent diffusivity tensor as in equation 5.3 and assuming the streamwise concentration gradient to be negligible compared to the cross-stream gradient, two components of the turbulent diffusivity tensor can be computed:

$$\Gamma_{12} = -\frac{\langle u'\phi' \rangle}{\frac{\partial \langle \phi \rangle}{\partial y}} \tag{5.13}$$

$$\Gamma_{22} = -\frac{\langle v'\phi' \rangle}{\frac{\partial \langle \phi \rangle}{\partial y}} \tag{5.14}$$

The off-diagonal component of the turbulent diffusivity tensor, Γ_{12}, takes values near zero close to the walls and increases in magnitude towards the center of the channel, as can be seen in figure 5.6. The non-zero values seen for all three data sets means that the assumption of scalar turbulent diffusivity not appropriate in this jet, neither at Reynolds number 20,000 nor at 50,000. As a consequence, the turbulent flux will not be aligned with the mean concentration gradient. The off-diagonal component of the turbulent diffusivity tensor is seen to be anti-symmetric. This is due to the anti-symmetric property of the mean concentration gradient. At the very center of the jet the mean concentration gradient changes sign. Dividing by values close to zero causes the computed Γ_{12} to be noisy here. The two experimental data sets give very similar Γ_{12} profiles. A Γ_{12} that is constant over a range of Reynolds numbers is a great advantage if one wishes to implement tensorial turbulent diffusivity in RANS. The fact that the large eddy simulation predicts the non-zero Γ_{12} and also captures the main features of its profile is in itself a demonstration of the superiority of the LES method over RANS in predicting turbulent transport.

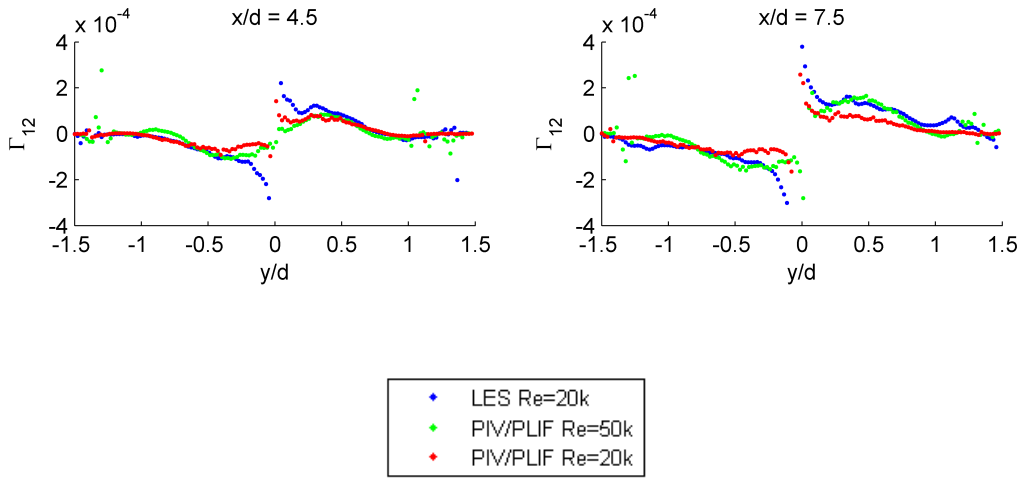

Figure 5.6: The off-diagonal component of the turbulent diffusivity tensor, Γ_{12}

If the turbulent diffusivity is assumed to be a scalar, it will be equal to Γ_{22}, which is the component Tavoularis and Corrsin [91] refers to as the turbulent diffusivity. It can be seen in figure 5.7 that Γ_{22} peaks in the high shear regions of the jet, which is where the mixing mainly occurs. The value increases from location $x/d = 4.5$ to 7.5. Both the diffusivity peaks in the high shear regions and the increase in diffusivity with downstream distance were also reported by Lemoine et al. [56] for the turbulent round jet at Reynolds number 9000 and by Borg et al. [6] in the round liquid jet at Reynolds number 6000. The peak values reported there are of the same order of magnitude as the ones reported in this work. Close to the walls, Γ_{22} goes to zero. While the simulation profile shows too high diffusivity values, the profiles from the two Reynolds numbers agree remarkably well. The fact that the turbulent diffusivity seems to be constant over a range of Reynolds numbers, and even shows consistency between different types of jets, is promising for the implementation of a tensorial, spatially varying turbulent diffusivity in RANS. The LES simulation captures the behavior of Γ_{22}, however, it predicts too high diffusivity values in the center region. This follows from the higher turbulent flux predicted by the simulation as reported in Chapter 4.

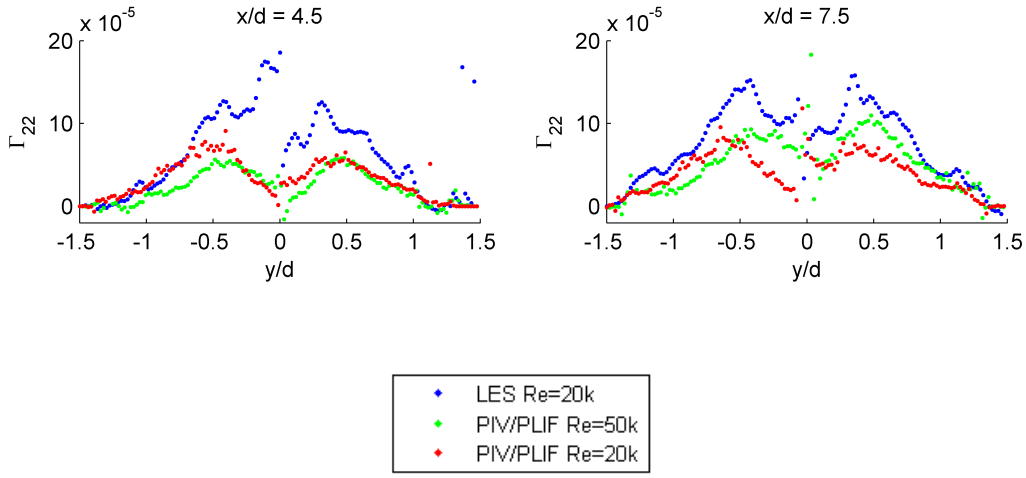

Figure 5.7: Turbulent diffusivity. Γ_{22}

The ratio of the two obtainable diffusivity components were reported to be a little over two in the shear flow of Tavoularis and Corrsin [91]. The corresponding ratios in the current jet flow are displayed in figure 5.8. The ratio is anti symmetric as follows from the anti-symmetry of the Γ_{12}. Close to the walls the values are noisy because the denominator of the ratio is close to zero. At location *x/d=4.5* the ratio is sloped and its magnitude goes between zero and two. The slope is seen for both Reynolds numbers and seems to be steeper in the highest Reynolds number case. At the next downstream location the profiles show a tendency to flatten out, in agreement with [23] and [91]. The value of the ratio tends towards one in the Reynolds number 20,000 case and a little higher in the 50,000 case. The agreement between simulation and experiment is remarkable and indicates that the large eddy simulation can predict the right tensorial behavior of the turbulent diffusivity. It is thus superior to methods using an assumption of scalar turbulent diffusivity.

The turbulent Schmidt number, Sc_T, is defined as:

$$Sc_T = \frac{\nu_T}{\Gamma_{22}} \tag{5.15}$$

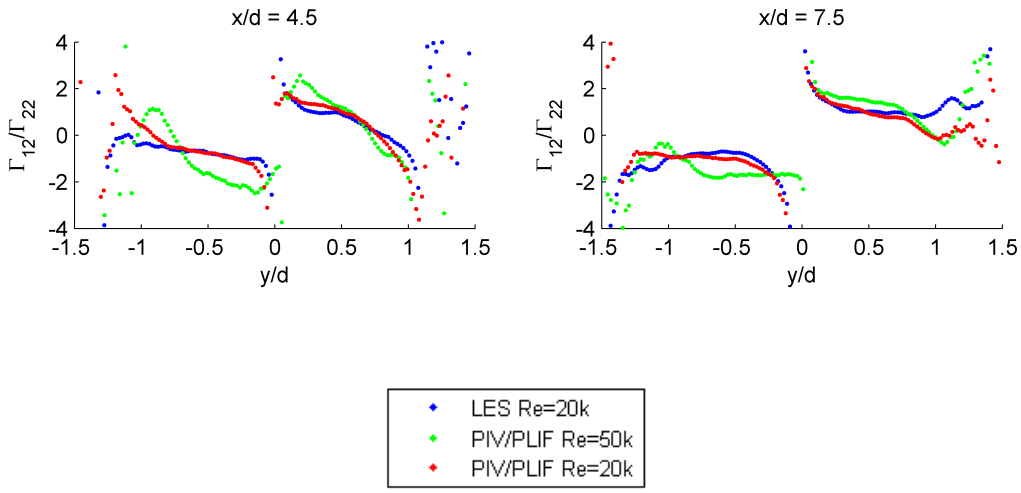

Figure 5.8: Ratio of Γ_{12} to Γ_{22}

where ν_T is the turbulent viscosity and is evaluated using:

$$\nu_T = -\frac{\langle u'v' \rangle}{\frac{\partial \langle u \rangle}{\partial y}} \tag{5.16}$$

Sc_T is computed from all three data sets and compared. Profiles across the channel are shown in figure 5.9. In large parts of the channel, the turbulent Schmidt number is constant and takes a value around 0.8-0.9. No Reynolds number dependency of Sc_T can be detected. It is seen that the Sc_T values are noisy close to the walls and at the center of the channel. This is because one or more of the terms $\langle v'\phi' \rangle$, $\frac{\partial \langle \phi \rangle}{\partial y}$, $\langle u'v' \rangle$ and $\frac{\partial \langle u \rangle}{\partial y}$ are close to zero there. Also in this respect, the simulation agrees well with the experiments.

With regard to turbulent diffusivity and alignment of the turbulent fluxes with the mean concentration gradient, it is of interest to look at their actual orientations. Figure 5.10 shows the orientation of the mean concentration gradient, given as the angle between the vector and the positive x-axis, positive towards positive y-direction and negative towards negative y-direction. The profiles are quite expected anti-symmetric with a magnitude close to 90 degrees in most of the channel. This agrees with the assumption of negligible streamwise mean concentration gradient. The values become noisy close to

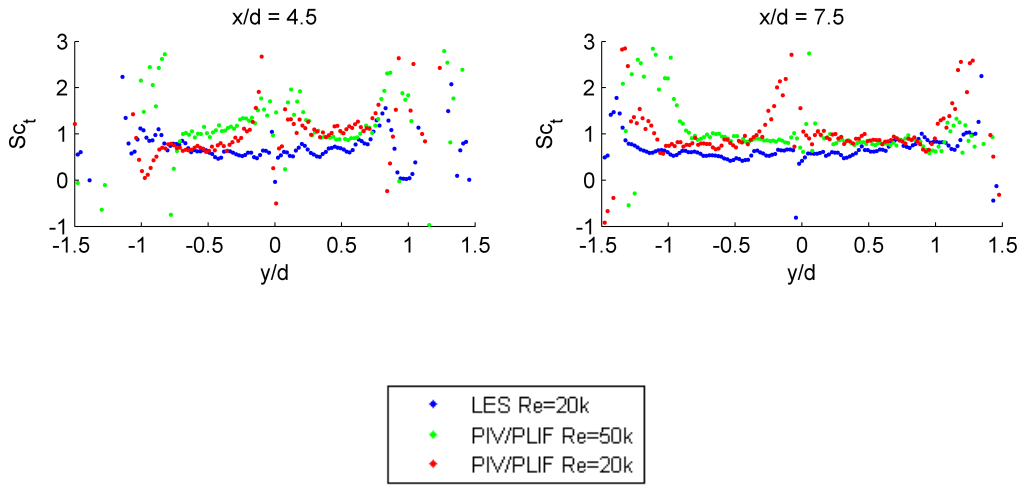

Figure 5.9: Turbulent Schmidt number

the walls and in the channel center because here the concentration gradient is close to zero.

In a similar manner, the orientation of the turbulent flux is displayed in figure 5.11. Also these profiles are anti-symmetric. The orientation profiles show a slope at location $x/d = 4.5$ and are approximately flat at location $x/d = 7.5$ where the angle is about ± 45 degrees. The two Reynolds number cases give very similar turbulent flux orientations, but the highest Reynolds number case gives somewhat smaller angles, i.e. the turbulent flux is pointing slightly more in the streamwise direction. The simulation captures the orientation of the turbulent fluxes very well. This is important, since the turbulent fluxes play a major role in the transport of momentum and mass in the flow. For the assumption of gradient diffusion with scalar diffusivity to be valid, the direction of mean concentration gradient and turbulent flux must be parallel and oppositely oriented. This implies a 180 degrees angle between them. In figure 5.12 the angle between the two vectors is plotted and it can be seen that it is close to 120 degrees and not 180. This is seen for both Reynolds numbers. The simulation also reproduced this feature.

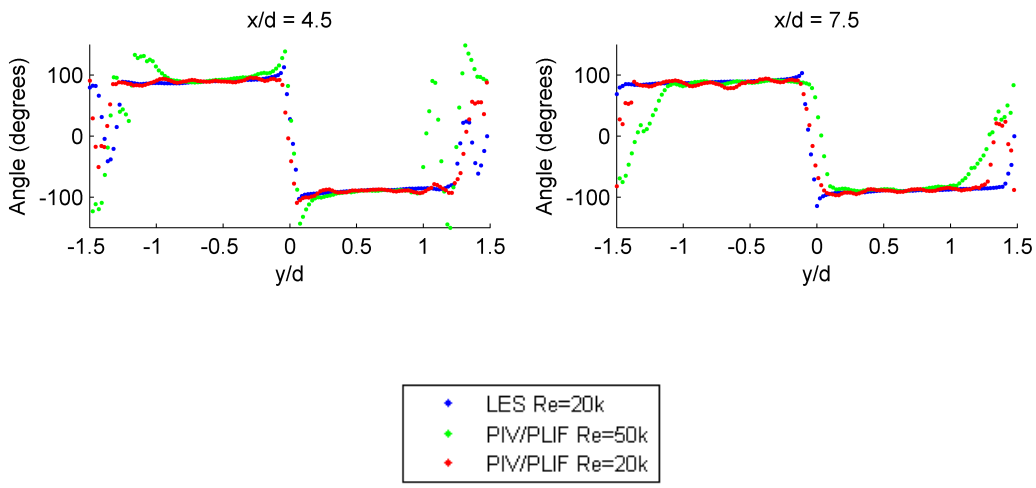

Figure 5.10: Orientation of mean concentration gradient. Angle with positive x-axis.

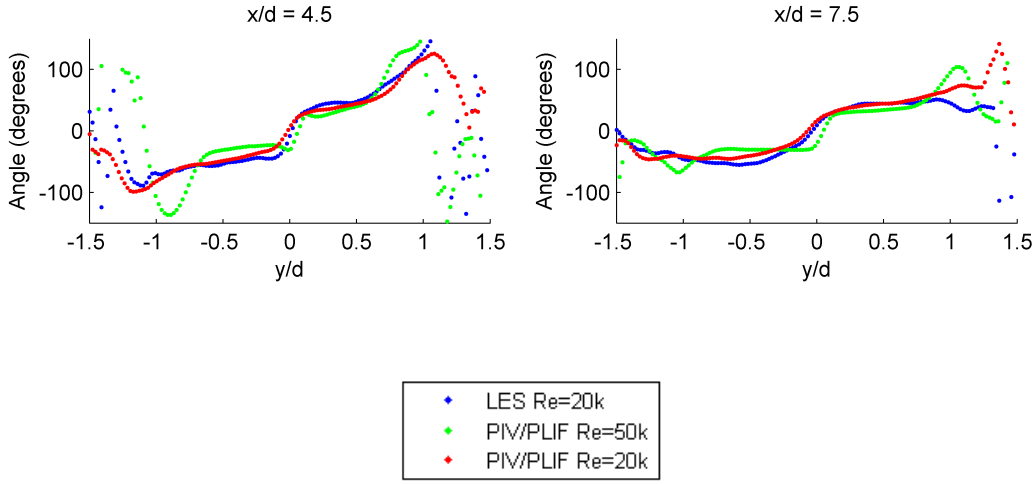

Figure 5.11: Orientation of the turbulent flux. Angle with positive x-axis.

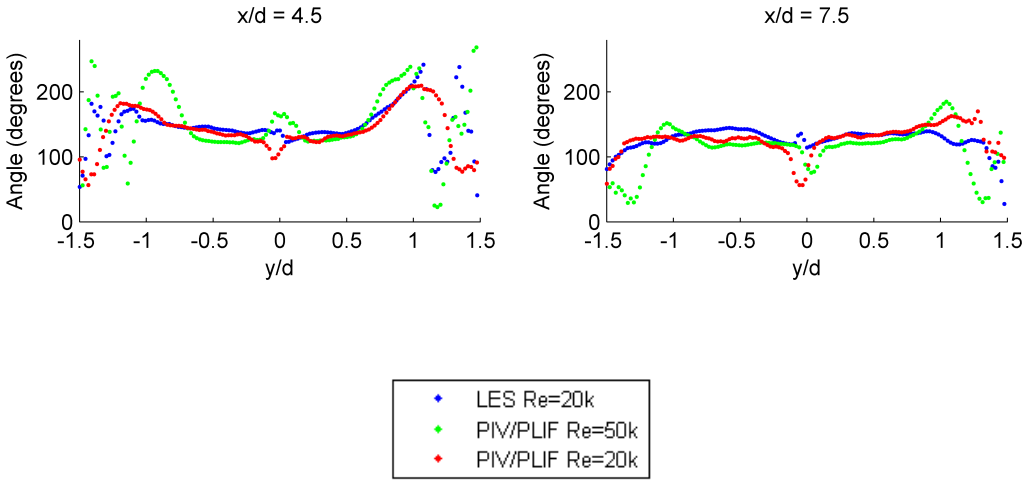

Figure 5.12: Angle between mean concentration gradient and turbulent flux.

5.4 Summary

This work has shown that the turbulent flux of a passive scalar in a confined jet with co-flow is not aligned with the mean concentration gradient and that LES of the flow was able to predict the mis-alignment.

Simultaneous PIV/PLIF data at Reynolds numbers 20,000 and 50,000 have been studied with regards to turbulent transport and the validity of the gradient diffusion hypothesis with constant scalar turbulent diffusivity. It was found that the turbulent diffusivity is neither a scalar nor a diagonal tensor in this confined rectangular jet, neither at Reynolds number 20,000 nor at 50,000. The off-diagonal component of turbulent diffusivity tensor that could be evaluated from the simultaneous velocity/concentration data was shown to be non-zero. Both turbulent diffusivity components estimated vary with position. The orientation of turbulent flux and mean concentration gradient and the angle between them were evaluated. The angle of the turbulent flux to the mean concentration gradient is non-zero. This is further evidence that the assumption of scalar turbulent diffusivity is invalid.

The turbulent diffusivities and the angle between turbulent flux and concentration

gradient were found to be consistent across the two Reynolds numbers. This indicates that implementing tensorial, spatially varying turbulent diffusivity in RANS could be feasible.

The simulation reproduces the studied turbulent transport features well. The profiles of the two components of turbulent diffusivity show the same trends as the experimental profiles, although the diffusivity components are somewhat overpredicted by the simulation. The ratio of the diffusivity components is in agreement with what was found from the experimental data. Furthermore, the simulation excellently predicts the orientation of the turbulent flux and its angle to the mean concentration gradient. The agreement indicates that the large eddy simulation is successful in simulating the main turbulent transport mechanisms and thus has a great advantage over RANS simulations that employ gradient diffusion modeling.

CHAPTER 6. FLOW IN A FOUR-INLET VORTEX REACTOR -EVALUATION OF RANS PREDICTIONS BY COMPARISON TO PIV DATA

Katrine M. Nilsen[1], Zhenping Liu[2], Rodney O. Fox,
James C. Hill and Michael G. Olsen

Abstract

The four-inlet reactor was designed at micro-scale with the purpose of mixing fluids to produce functional nano-particles through the flash nano-precipitation (FNP) process, a process where rapid mixing is necessary. A scale-up of the micro reactor is motivated by a higher through-put than what is possible in the micro reactor. This work presents initial studies of the flow in a scaled-up reactor and is a first step towards developing numerical methods to predict the reactor's mixing performance.

The four-inlet vortex reactor has been studied by Reynolds-averaged Navier-Stokes (RANS) simulation and the results have been evaluated by comparison to particle image velocimetry (PIV) data and stereo-PIV data. Simulation parameters such as geometry, grid, numerical schemes, solver and boundary conditions are assessed, and recommendations for further work are given.

The flow in the reactor is found to include a main vortex in the center extending up into the outlet pipe. The investigations revealed that the vortex core "dances" around

[1]Primary researcher and author
[2]Experimental researcher

a central position. Since the flow is not steady-state, unsteady-RANS is required. It has been demonstrated that the grid in the center region of the reactor needs to be fine in order to capture the vortex behavior appropriately. It was found that the Reynolds stress model and the v2f model with curvature correction were able to predict the flow quite well.

6.1 Introduction

Mixing of fluids is important in many engineering situations, and especially in chemically reacting flows. Turbulence enhances mixing rates and is therefore often used to speed up mixing processes. Knowledge of turbulent mixing is therefore of great importance, not only to improve the general understanding of turbulence and turbulent transport but also for design and optimization of turbulent mixing configurations. Turbulent transport is, however, a very complex phenomenon and there is still much to be learned.

The four-inlet vortex reactor [60] was designed at micro-scale for the production of nano-particles by the flash nano-precipitation (FNP) process [46] where rapid mixing is crucial. The advantages of the reactor design are many. Firstly, the four tangential inlets give flexibility of flow rates and one is not dependent on equal momentum as one is in impinging jet reactors. Secondly, the reactor can produce continuously. Furthermore, the design does not include moving parts and is therefore robust and requires little maintenance.

Investigations of the micro reactor were performed using both experimental methods and computational fluid dynamics (CFD). Its mixing performance was studied experimentally using competitive fast reactions[60] and by combining confocal laser scanning microscopy (CLSM) and laser induced fluorescence (LIF) [86]. The competitive fast reaction results, obtained by Liu et al., were used to evaluate CFD-predictions of the

mixing in the reactor. Different flow configurations (inlet concentrations and inlet flow rate ratios) and different Reynolds numbers were investigated. It was found that the mixing performance was relatively stable for different flow configurations and that an overall Reynolds number as in equation 6.1, taking into account the bulk velocity, U and kinematic viscosity, ν, of all the four inlet streams i, can be used to describe the mixing performance.

$$Re_o = \sum \frac{U_i D}{\nu_i} \tag{6.1}$$

D is the reactor diameter. For Re_o above 1600 homogeneous mixing was obtained for reactions with time constants longer than 50 ms. CLSM and LIF was employed by Shi et al. [86] to measure concentrations in the micro reactor and thereby evaluate the mixing performance. Measurements were made at inlet-Reynolds numbers up to 240. It was found that even at the highest Reynolds number the mixing was not completed inside the reactor, and suggested that higher Reynolds numbers are needed.

Cheng and Fox [8] developed a promising model for predicting the FNP process in the reactor. Since the FNP process is closely connected to mixing, the model relies on coupling with CFD. Thus reliable CFD methods are desired.

Micro particle image velocimetry (μPIV) was performed on the micro reactor for inlet-Reynolds numbers 53, 93 and 240, and velocity fields at three locations in the reactor were obtained [9, 85]. The investigations showed that at inlet Reynolds number 53 the flow was laminar and strong wall effects could be seen. With increasing Reynolds numbers, the wall effects were less dominant and the ratio of tangential velocity to radial velocity increased. At the highest Reynolds number, indications of a recirculation zone in the vortex center were seen and the vortex core was found to move a little. CFD predictions of the in-reactor flow were also obtained, using large eddy simulation (LES) and Reynolds-averaged Navier-Stokes (RANS), and the results were compared to the experimental data. The LES results compared quite well, although some discrepancies were seen in the radial velocity component. This could, however, be attributed to the

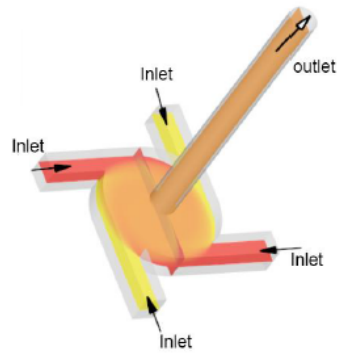

Figure 6.1: The four-inlet vortex reactor.

higher measurement error in this relatively small velocity component. The moving vortex core was also not predicted by the LES. The RANS was not able to reproduce the velocity field properly and it was suggested that the flow was not turbulent enough for RANS with the employed parameters to be appropriate.

A scale-up of the reactor is motivated by a higher trough-put. The hope is that the higher Reynolds numbers that can be obtained in the scaled-up geometry will contribute to rapid mixing of the liquids and that this will outweigh the effect of larger geometrical scales on the mixing times. In this work, a prototype model has been build and set up for measurements of velocity fields by stereo particle image velocimetry (SPIV). These data are excellent for evaluating CFD results. The aim of the current work is to evaluate the use of RANS numerical simulation for predicting the flow field in this reactor and to give recommendations for its use in optimization and process design. This represents an important first step towards obtaining reliable numerical methods to predict the FNP process in the reactor.

Although the current flow configuration has not been studied before, at least not to our knowledge, some characteristics of the flow are similar to other types of flows and knowledge of these will enhance understanding of this flow. Swirling flows are found in cyclone separators which is a more commonly studied type of flow. Hreiz et al. [43] gives an overview of the main flow features of a liquid cyclone flow. They divide the

flow field in different regimes in the radial direction. The core is characterized by solid body rotation and the mean tangential velocity is proportional to the distance from the center. There, the centrifugal action is stabilizing the turbulence. Further away from the core the forced vortex transitions into a free vortex and the tangential velocity profile is inversely proportional to the distance from the center. In this annular region, the centrifugal action is destabilizing the turbulence and the flow is characterized by high skewness and strong anisotropy. Close to the wall, the velocity goes to zero, but because of the streamline curvature, the law of the wall can not be expected to be valid in all cases. CFD studies of swirling flows include the work of Hoekstra et al. [41] on a gas cyclone separator. They performed axisymmetric RANS and compared the results to laser Doppler velocimetry (LDV) data. Different turbulence models were tested and also the effect of outlet diameter was investigated. It was found that the Reynolds stress turbulence model performed best of all the tested turbulence models, although it still gave some discrepancy with the experimental data. The LDV data revealed that the vortex core is moving.

6.2 Experimental Setup

In particle image velocimetry (PIV) [1], the flow to be measured is seeded with tracer particles that are small enough to follow the flow accurately. The flow is illuminated by a pulsating laser sheet and the tracer particles scatter the laser light so that a camera can capture the particle positions at the time of the laser pulse. The particle displacement between two successive images with a known time interval can be found using a correlation technique. From the displacement and the time interval the local velocity is found. Thus PIV provides field velocity data. In stereo-PIV (SPIV) two angled cameras are used and by combining the information from the two cameras the third out-of-plane component of velocity can be obtained.

The scaled-up four-inlet vortex reactor has a diameter, D, of 101.6 mm and a height, H, of 25.4 mm. The outlet pipe has a diameter of 25.4 mm and the inlet ducts are 25.4 mm square. Before entering the inlet ducts, the flow goes through flow condition sections to even out the profiles and help the turbulence develop. In addition, the inlet ducts are made long to give the flow time to develop before it reaches the reactor. The flow rate in each inlet is controlled separately by four control valves and flow meters. The flow rate is set to 0.16 L/s in each inlet and this corresponds to an inlet duct Reynolds number of about 6275. The flow is seeded with glass particles. The geometry is built in acrylic. Clear acrylic is used on the side walls and the reactor bottom to ensure optical access to the flow while the top is black to limit disturbing light reflections. A pulsating horizontal laser sheet enters the reactor through the side walls and the cameras are placed below the reactor as shown in figure 6.2. One camera is used for PIV while two cameras are used for SPIV. PIV measurements are made at three locations inside the reactor, in the mid-plane and at one quarter height to the top and to the bottom, as indicated in figure 6.2. PIV measurements are made of the whole field while SPIV measurements are zoomed in on the center of the reactor where the out-of-plane component of velocity is expected to be significant. The SPIV is done in the mid plane.

6.3 Numerical Method

The flow in the four-inlet reactor is simulated using RANS. This simulation method is based on a Reynolds-averaging of the governing equations for the fluid flow. The averaged equations take the form

$$\frac{\partial \bar{u}_i}{\partial t} + \bar{u}_j \frac{\partial \bar{u}_i}{\partial x_j} = -\frac{1}{\rho}\frac{\partial \bar{p}}{\partial x_i} + \nu \frac{\partial^2 \bar{u}_i}{\partial x_j x_j} - \frac{\partial \overline{u'_j u'_i}}{\partial x_j} \tag{6.2}$$

$$\frac{\partial \bar{u}_i}{\partial x_i} = 0 \tag{6.3}$$

where u_i are components of velocity, t is time, x_i are spatial coordinates, ρ is density of the fluid, p is pressure and ν is kinematic viscosity. Overbar indicates Reynolds averaged

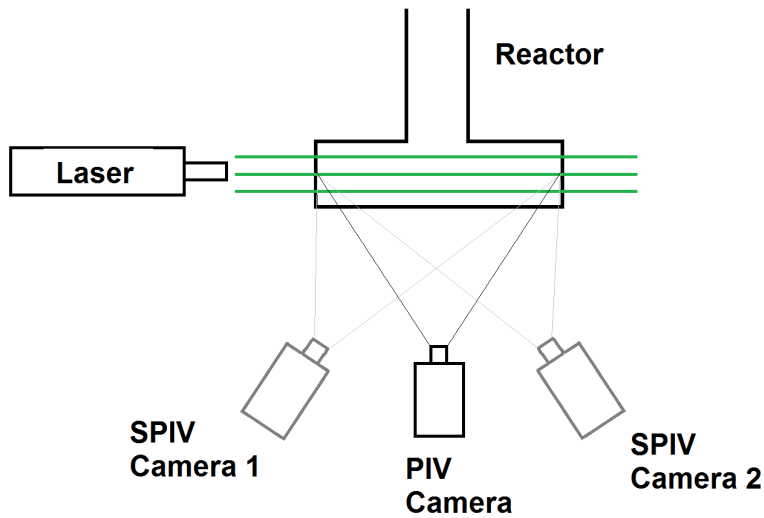

Figure 6.2: Schematic of the experimental setup.

values and $u_i' = u_i - \bar{u}_i$. The last term of equation 6.2 is a derivative of the Reynolds stress tensor, $\overline{u_j' u_i'}$, which is unknown and must be modeled. This term represents the effect of turbulence on the mean field. A common approach is to assume that the effect of turbulence is enhanced diffusion and to model the turbulence by introducing an eddy viscosity, ν_T:

$$-\overline{u_j' u_i'} = \nu_T \left(\frac{\partial \bar{u}_i}{\partial x_j} + \frac{\partial \bar{u}_j}{\partial x_i} \right) - \frac{2}{3} k \delta_{ij} \tag{6.4}$$

where k is the turbulent kinetic energy defined as $k = \frac{1}{2}\overline{u_i' u_i'}$. The system of equations can then be closed by a model for ν_T. The k-ϵ model [47] is one of the earliest and the most widely used eddy viscosity models.

$$\nu_T = C_\mu \frac{k^2}{\epsilon} \tag{6.5}$$

C_μ is a model constant and ϵ is turbulent energy dissipation rate given by $\epsilon = \nu \overline{\frac{\partial u_i'}{\partial x_j} \frac{\partial u_i'}{\partial x_j}}$. k and ϵ are determined by solving their respective model transport equation given by

$$\frac{\partial k}{\partial t} + \bar{u}_j \frac{\partial k}{\partial x_j} = P - \epsilon + \frac{\partial}{\partial x_j} \left((\nu + \nu_T) \frac{\partial k}{\partial x_j} \right) \tag{6.6}$$

and

$$\frac{\partial \epsilon}{\partial t} + \bar{u}_j \frac{\partial \epsilon}{\partial x_j} = \frac{C_{\epsilon 1} P - C_{\epsilon 2} \epsilon}{T} + \frac{\partial}{\partial x_j} \left((\nu + \frac{\nu_T}{\sigma_\epsilon}) \frac{\partial \epsilon}{\partial x_j} \right) \tag{6.7}$$

where $P = -\overline{u_i' u_j'}\frac{\partial \bar{u}_i}{\partial x_j}$, $T = \frac{k}{\epsilon}$ and $C_{\epsilon 1}$, $C_{\epsilon 2}$ and σ_ϵ are model constants. The popularity of the $k - \epsilon$ model may stem from the fact that it was the first two-equation model adopted. It is relatively simple to implement and also relatively robust. However, the model cannot reproduce the right near-wall behavior. Therefore, some modification to the model is necessary close to solid boundaries. A common approach is to introduce wall functions that make use of the universality of near-wall turbulence to prescribe the near-wall profiles. Another drawback to the model is that the turbulence is represented by scalar values, k and ϵ, and therefore cannot correctly account for anisotropy.

A promising eddy viscosity model is the $v^2 - f$ model (v2f) [21, 74] which is an extension to the k-ϵ model that accounts for near-wall turbulence anisotropy and non-local pressure-strain effects. The model can be used down to solid boundaries without the need of wall functions. Two extra equations are solved, one transport equation for a velocity scale, $\overline{v^2}$:

$$\frac{\partial \overline{v^2}}{\partial t} + \bar{u}_j \frac{\partial \overline{v^2}}{\partial x_j} + \epsilon \frac{\overline{v^2}}{k} = kf + \frac{\partial}{\partial x_j}\left((\nu + \nu_T)\frac{\partial \overline{v^2}}{\partial x_j}\right) \tag{6.8}$$

and one elliptic equation for the function f:

$$L^2 \nabla^2 f - f = -c_2 \frac{P}{k} + \frac{c_1}{T}\left(\frac{\overline{v^2}}{k} - \frac{2}{3}\right) \tag{6.9}$$

where the length and time scales are defined as $L = C_L \max\left(\frac{k^{3/2}}{\epsilon}, C_\eta \left(\frac{\nu^3}{\epsilon}\right)^{1/4}\right)$ and $T = \max\left(\frac{k}{\epsilon}, 6\left(\frac{\nu}{\epsilon}\right)^{1/2}\right)$, and c_1 and c_2 are model constants. The eddy viscosity is then calculated as

$$\nu_T = C_\mu \overline{v^2} T \tag{6.10}$$

C_μ is a model constant.

The eddy viscosity models using equation 6.4 do not take rotation or streamline curvature effects into account. A solution to this problem is to sensitize the eddy viscosity constant to such effects [75]. Duraisamy and Iaccarino [20] suggested a curvature correction to the v2f model that is a modification of the model constant C_μ. The work is an

extension of the work of Petterson Reif et al. [75] where curvature effects are accounted for by making C_μ a function of dimensionless velocity gradient invariants, η_1 and η_2:

$$C_\mu* = C_\mu \frac{1+\alpha_2\left|\eta_3\right|+\alpha_3\eta_3}{1+\alpha_4\left|\eta_3\right|}\left[\sqrt{\frac{1+\alpha_5\eta_1}{1+\alpha_5\eta_2}}+\alpha_1\sqrt{\eta_2\left(\left|\eta_3\right|-\eta_3\right)}\right]^{-1} \tag{6.11}$$

where $\eta_3 = \eta_1 - \eta_2$ and $\{\alpha_1, \alpha_2, \alpha_3, \alpha_4, \alpha_5\} = \{0.055, 0.5, 0.25, 0.2, 0.025\}$. Duraisamy and Iaccarino define η_1 and η_2 as:

$$\eta_1 = \frac{k^2}{\epsilon^2}\left|\left(\frac{1}{2}\left[\frac{\partial\bar{u}_i}{\partial x_j}+\frac{\partial\bar{u}_j}{\partial x_i}\right]\right)\right|^2 \tag{6.12}$$

$$\eta_2 = \frac{k^2}{\epsilon^2}\left|\left(\frac{1}{2}\left[\frac{\partial\bar{u}_i}{\partial x_j}-\frac{\partial\bar{u}_j}{\partial x_i}\right]\right)+C_\omega\bar{\Omega}_{ij}\right|^2 \tag{6.13}$$

where C_ω is a constant. $\bar{\Omega}_{ij} = \varepsilon_{ijk}\bar{\omega}_k$ works as a measure of the local rotation rate and is where the curvature is accounted for. There are different ways of obtaining $\bar{\omega}_k$. The one adopted here is:

$$\bar{\omega}_i = \frac{\Pi_1^2\delta_{ij}+12\Pi_2 S_{ij}+6\Pi_1 S_{ik}S_{kj}}{2\Pi_1^3-12\Pi_2^2}S_{pl}S'_{lq}\varepsilon_{pqj} \tag{6.14}$$

where $S_{ij} = \frac{1}{2}\left(\frac{\partial\bar{u}_i}{\partial x_j}+\frac{\partial\bar{u}_j}{\partial x_i}\right)$, $\Pi_1 = trace(S^2)$ and $\Pi_2 = trace(S^3)$ and S' is the material derivative of S.

Another approach to turbulence modeling is the Reynolds stress models in which the transport of the full Reynolds stress tensor is modeled. The transport equation for the Reynolds stress is

$$\frac{\partial\overline{u'_iu'_j}}{\partial t}+\bar{u}_k\frac{\partial\overline{u'_iu'_j}}{\partial x_k} = -\frac{1}{\rho}\left(\overline{u'_j\frac{\partial p}{\partial x_i}}+\overline{u'_i\frac{\partial p}{\partial x_j}}\right)-2\nu\overline{\frac{\partial u'_i}{\partial x_k}\frac{\partial u'_j}{\partial x_k}}-\frac{\partial\overline{u'_ku'_iu'_j}}{\partial x_k}-\overline{u'_ju'_k}\frac{\partial\bar{u}_i}{\partial x_k}-\overline{u'_iu'_k}\frac{\partial\bar{u}_j}{\partial x_k}+\nu\nabla^2\overline{u'_iu'_j} \tag{6.15}$$

where the first three terms on the right side are unclosed. The Launder-Reece-Rodi (LRR) basic model [53] gives the following model equation for the Reynolds stress transport:

$$\frac{\partial\overline{u'_iu'_j}}{\partial t}+\bar{u}_k\frac{\partial\overline{u'_iu'_j}}{\partial x_k} = P_{ij}-\frac{2}{3}\delta_{ij}\epsilon-c_1\frac{\epsilon}{k}\left(\overline{u'_iu'_j}-\frac{2}{3}\delta_{ij}k\right)-c_2\left(P_{ij}-\frac{2}{3}P\delta_{ij}\right)+c_s\frac{\partial}{\partial x_l}\left(\frac{\epsilon}{k}\overline{u'_lu'_k}\frac{\partial\overline{u'_iu'_j}}{\partial x_k}\right) \tag{6.16}$$

where $P_{ij} = -\overline{u'_j u'_k}\frac{\partial \bar{u}_i}{\partial x_k} - \overline{u'_i u'_k}\frac{\partial \bar{u}_j}{\partial x_k}$. Commonly, in the presence of solid boundaries another term is added to equation 6.16 to account for wall effects. The model is developed for high Reynolds number flows and therefore the diffusion term $\nu\nabla^2\overline{u'_i u'_j}$ is assumed small and omitted in the above equation. It is, however, a closed term and can be included without further modeling. ϵ is found from a model transport equation, as in equation 6.7. The Reynolds stress models have the advantage that they can account for anisotropy and do not assume a linear relation between the mean rate of strain and the stresses; however, this comes at the cost of more computer power and less robust equations.

The governing equations are discretized and solved in the domain shown in figure 6.3 using the open source CFD library OpenFOAM [63]. Several attempts to solve the equations using the steady solver SIMPLE were made. However, only at coarse grids a convergent solution could be obtained. For higher grid resolutions the numerical residuals would oscillate and a steady state solution could not be found. From literature on similar flows it is seen that the vortex core is "dancing" around a central position, also called precessing vortex core phenomenon [43]. Also in the micro reactor, signs of precessing vortex core was found. Therefore, the experimental data were investigated for signs of "dancing" vortex. It was found that the location of the vortex center varies from realization to realization and is randomly distributed within a radius of about 2.5 mm from the reactor center. This explains why a steady state solution can not be found. Unsteady RANS (URANS) is then the appropriate choice. The simulation result was averaged over time in order to obtain mean values that can be compared to the PIV data. The use of URANS has the advantage that the simulation can potentially capture the vortex motion. However, the approach is more computationally expensive than the initially attempted steady RANS. The unsteady solver used was PIMPLE (merged PISO-SIMPLE) with the Euler time scheme. A first order upwind spatial scheme was used. Other schemes were tested, but could not produce a convergent solution. Standard wall functions were used.

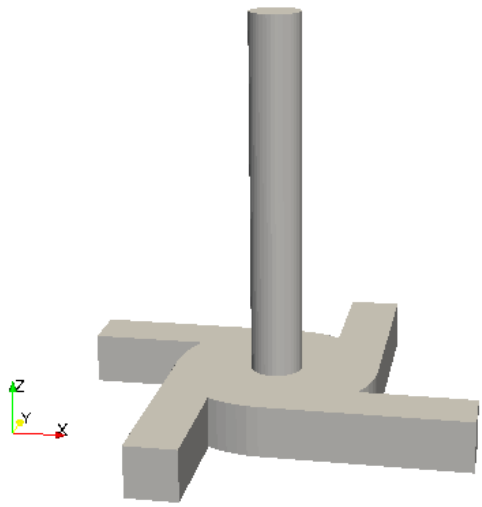

Figure 6.3: The simulation domain. z-direction is upwards along the outlet axis.

As inlet conditions, fully developed turbulent flow in square duct is assumed. A precursor simulation is performed on a piece of square duct where the outflow is recycled as inflow. In this way fully developed conditions can be reached quickly. A cross-sectional plane of the precursor simulation is mapped to each of the four inlets of the reactor in the main simulation. It was seen that close to the reactor chamber, the flow in the reactor is affecting the inlet duct velocity, so that the inlet duct flow is not symmetrical there. Several simulation runs of the flow in the reactor were performed where different lengths of the inlet ducts were included in the domain. The examination revealed that the main domain should cover at least $2.5H$ of the inlet ducts for the assumption of fully developed turbulence at the inlet to be valid.

The outlet pipe has to be made long enough to cover any recirculation zones that may exist in the flow, to make sure there is no back-flow through the outlet face. Long outlet pipe also makes the assumption of negligible gradients in the streamwise direction valid, so that zero gradient outlet conditions can be used. Commonly, the pressure outlet condition is a fixed value condition. In this case, because the flow features swirl, the pressure varies with radial position in the outlet pipe. A zero gradient pressure

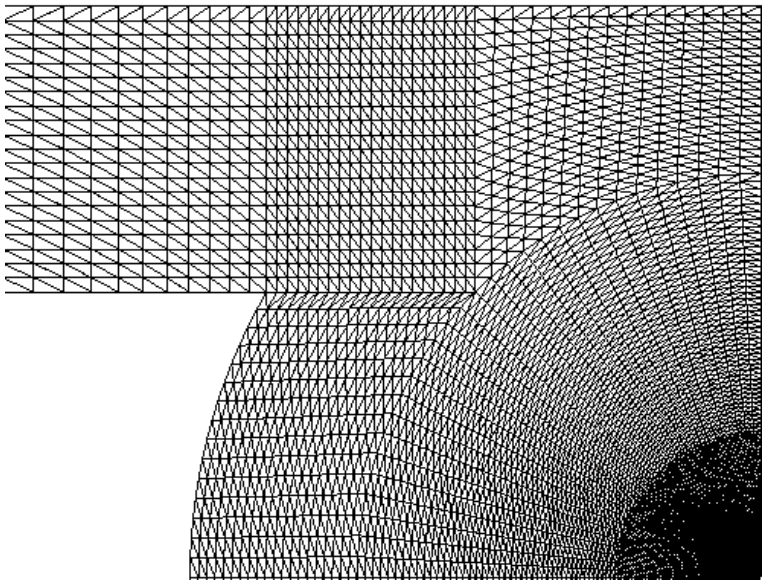

Figure 6.4: Section of the grid.

condition enabled the simulation to capture this pressure variation properly.

The grid is made out of mainly hexahedra cells. Figure 6.4 shows a section of the grid. The final grid has 2.6 million cells. Initial simulations showed that the grid must be fine in the center part of the reactor in order for the simulation to capture the flow features there. This is evident when looking at the axial velocity. At low grid resolution, there is a recirculation zone inside the outlet pipe, recognized by negative axial velocity values. With increasing grid resolution the recirculation zone moves down into the reactor. This is seen in figure 6.5 where the axial velocity in a vertical, center plane of the domain is plotted for increasing grid resolutions. From the second finest grid to the finest grid, the main structures of the flow are not changing, indicating that the grid is fine enough.

The turbulence models tested were LRR, v2f and v2f with curvature correction, here called v2fr. LRR and v2f are available in OpenFOAM, but v2fr was not. Therefore, the curvature correction to v2f had to be implemented in OpenFOAM. The implementation builds on that of the v2f model and includes the curvature correction following equations 6.11 to 6.14. It was seen that the simulations predicted low turbulence levels in most of

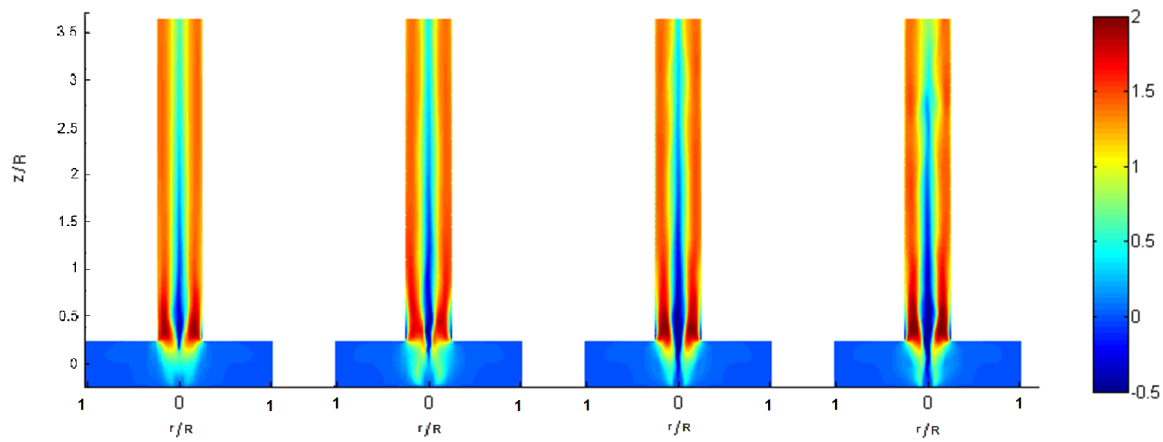

Figure 6.5: Axial velocity in vertical center plane. Grid resolution increases from left to right.

the reactor. Therefore, an additional simulation was run completely without turbulence modeling, i.e. $\nu_T = 0$. This is here called the laminar case.

6.4 Results

Because of the swirling nature of the flow in the reactor, the velocity is presented as tangential, radial and axial components. Coordinates are normalized by the reactor radius, R. $z = 0$ is defined to be at the center plane of the reactor.

Simulation results from the four runs using different turbulence models are compared to PIV data. Tangential velocities along a line through the reactor center in the $z = 0$ plane are displayed in figure 6.6. The tangential velocity has its highest magnitude at $r/R \approx 0.1$ and is zero in the center. For r/R close to one, the tangential velocity is close to the inlet bulk velocity of 0.248 m/s. The tangential velocity profiles are seen to agree well with the expected forced vortex in the center, where the velocity is proportional to r, and the free vortex in the outer part, where the profile goes as $1/r$. Intuitively, a solid body rotation is not expected to have positive effect on mixing. However, the flow field is complex and more investigations are necessary in order to draw conclusions regarding the mixing performance of the reactor. It can be seen that

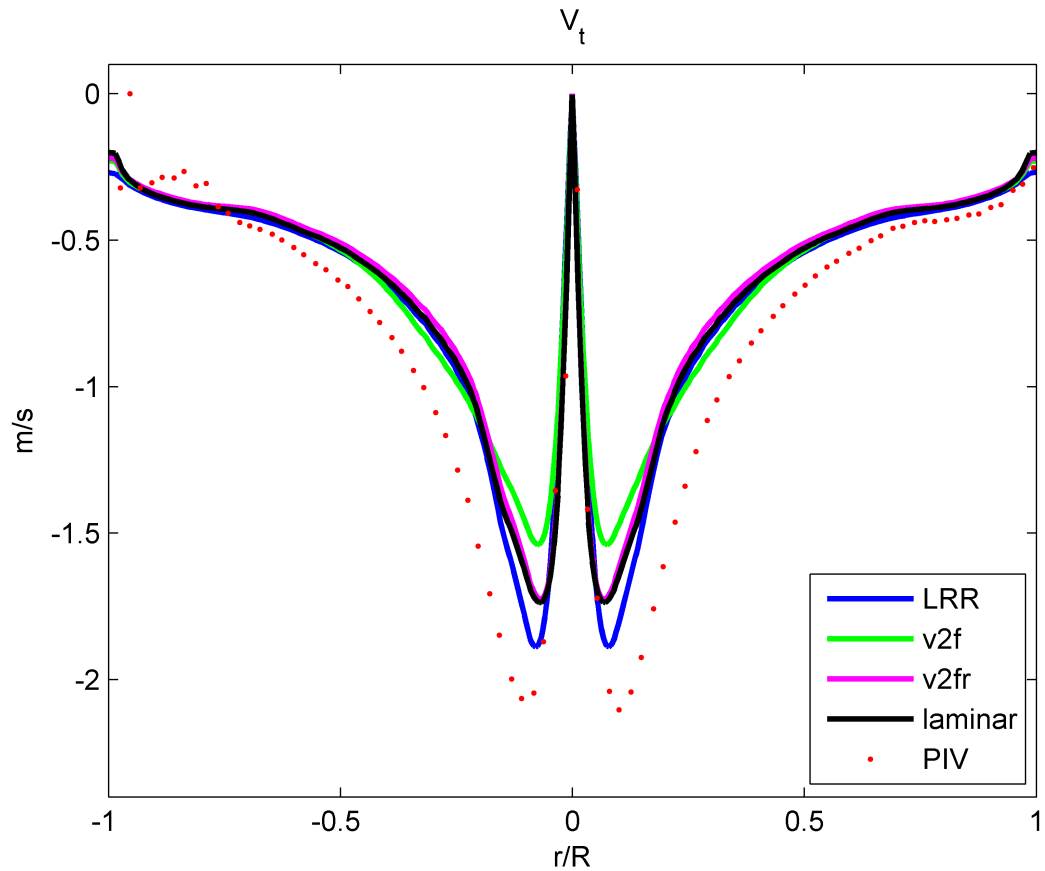

Figure 6.6: Tangential velocity profile across the reactor in the center plane.

the simulations can predict the shape of the profile, but that none of the turbulence models can reproduce the high magnitude peaks. The LRR model performs the best and the peak tangential velocity value using LRR is 10% lower than the experimental peak. The v2f model has the poorest performance of the tested turbulence models and the maximum tangential velocity magnitude is 25% below the PIV data. The curvature correction to the v2f model improves the prediction quite significantly. Interestingly, the laminar case performs similar to the v2fr. This may indicate that the strong swirl in the center of the reactor is stabilizing the turbulence and that the curvature correction is able to capture this.

In figure 6.7 the radial velocity component in the center plane is compared. It is seen that the radial velocity is mostly negative (flow towards the center), and peaks

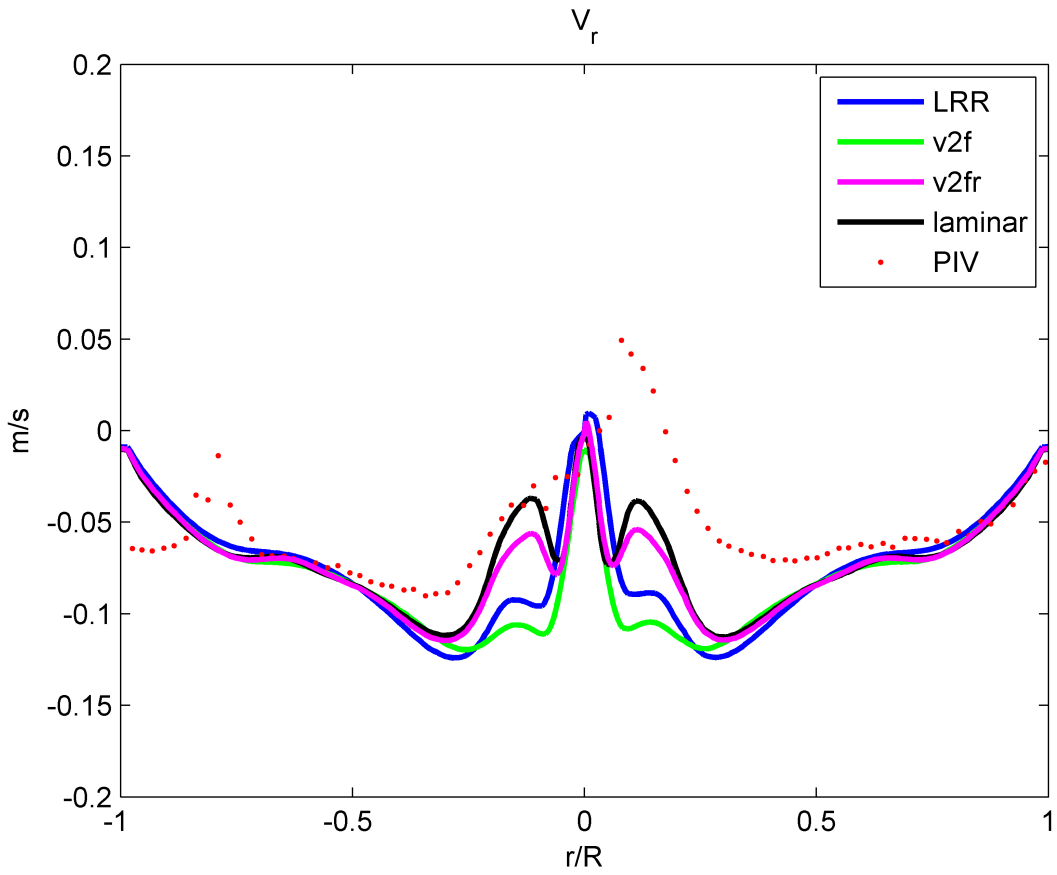

Figure 6.7: Radial velocity profile across the reactor in the center plane.

near the center. This is captured by all the turbulence models. The experiment gives asymmetrical profile, while the simulation profiles are symmetrical. It is in the center part of the reactor that differences are seen between the turbulence models. The simulation profiles are in general lower than the experimental profile. It is the laminar and the v2fr cases that give profiles most similar in shape to the experimental profile. As opposed to what was seen in the tangential velocity, some difference between the laminar and the v2fr profiles is seen here, and overall the laminar seems to give the best prediction. The experiment gives positive radial velocity values close to the center, meaning fluid is flowing away from the center here. It is only the LRR and the v2fr turbulence models that predict this, although the predicted radial velocity is smaller in magnitude than the experimental velocity.

The axial velocity component was measured by SPIV in the center section of the reactor in the $z = 0$ plane. The axial component of velocity from the simulations are compared to the SPIV results. Because of the axissymmetrical nature of the axial velocity in the center section, the values are averaged around the center. It is seen in figure 6.8 that the axial velocity is measured to be negative in the center. Negative axial velocity means fluid is flowing downwards and indicates that a recirculation zone exists in the center. The measured negative velocity magnitude is surprisingly high; 0.3 m/s, which is 1.2 times the bulk inlet velocity. The LRR and the laminar also predict negative axial velocity in the very center, but only 0.06 m/s and 0.01 m/s, respectively. Although not negative, the v2fr predicts axial velocity close to zero in the center, while the v2fr predicts relatively high center axial velocity. Away from the center, the axial velocity peaks positive; SPIV data gives maximum axial velocity of 1.06 m/s. The peak location coincides with the location of the peak in tangential velocity, at $r/R \approx 0.1$. At higher r/R the axial velocity decays to zero. It can be seen that the laminar and the v2fr best can predict the axial velocity peak, although the velocity is a little too low. The LRR and the v2f also predict peaks, but the velocity magnitude is much lower than the experimental result. An explanation for the different axial velocity behavior is found by studying where the fluid exiting the reactor is coming from. In all cases, the fluid has the highest inwards radial velocity close to the reactor floor and ceiling. For the laminar case and the v2fr case, the radial velocity at the floor is stronger than in the other cases. This indicates more fluid is extracted from the bottom in the laminar and v2fr case than in the other cases, and this causes the axial velocity in the center plane to be higher in order to transport out the extracted fluid. Following this argumentation, the high axial velocity magnitude measured by SPIV can be seen as an indication that also in the experiment much of the fluid is extracted from the bottom. In the case of v2f it is clear that the underprediction of tangential velocity causes the pressure to be overpredicted in the center and thus the axial velocity is too high in the center. Fluid can then flow

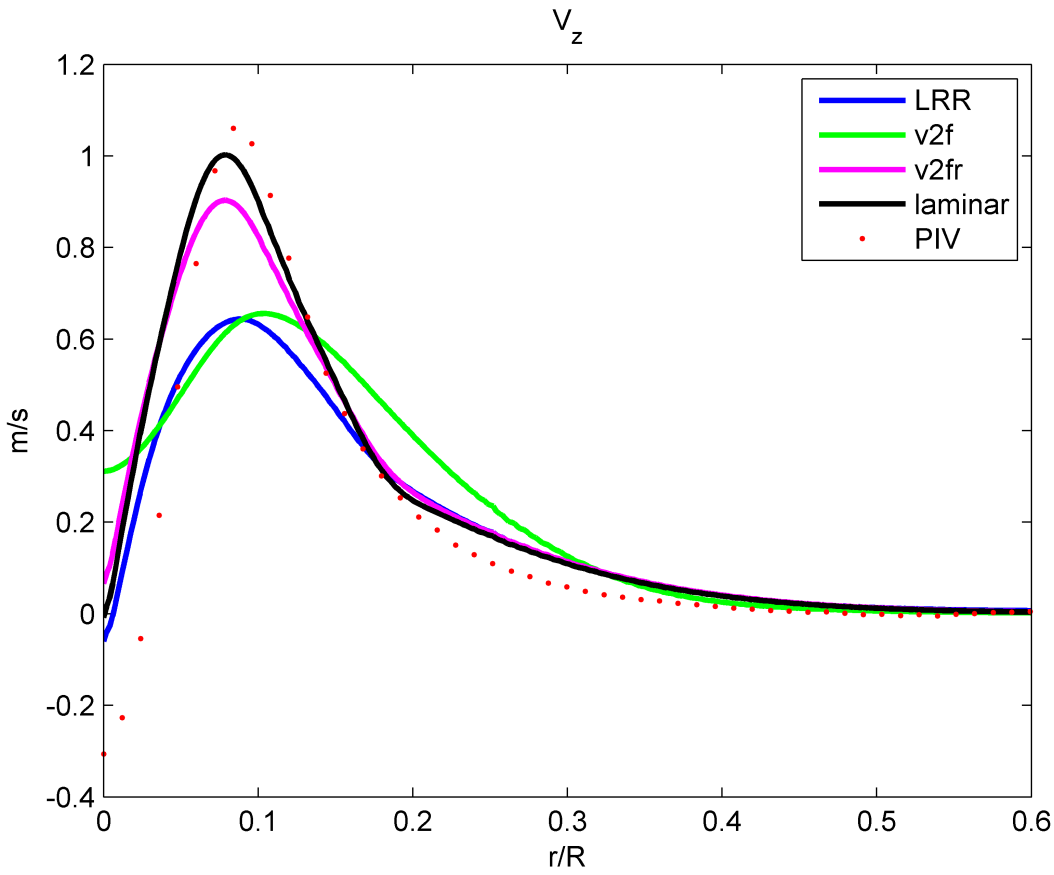

Figure 6.8: Axial velocity profile in the center plane.

upwards in the whole center region of the reactor, and thus the axial velocity peak is not as high as in the cases where fluid is only flowing upwards in an annular region around the center.

The fact that the laminar model does so well indicates that in regions of the reactor, the flow shows laminar behavior. As a consequence, turbulence models that can handle low turbulence levels are preferred. Unfortunately, most turbulence models are based on the assumption of high Reynolds number. Of the tested models, LRR and v2fr seem to give the best low turbulence behavior. Based on the ability of the LRR to predict the high tangential velocity and the recirculation zone, the LRR results were chosen for the following closer examination.

Monitoring the simulation results over time unveiled that the URANS did predict a

moving vortex core. Figure 6.9 displays how the tangential velocity in a given point varies with time. The probe location is in the center plane at $r/R = 0.07$, which, as was seen in figure 6.7, is within the forced vortex region and a location where the mean tangential velocity gradient is high. The fluctuations are seen to be quite regular and consist of large-scale fluctuations of low frequency and high amplitude with small-scale fluctuations of higher frequency and lower amplitude superimposed. Two main frequencies are found, 11.5 Hz and 67 Hz. The fluctuations in velocity are likely originating in a moving vortex core. Sampling center plane velocity fields over the same time interval as for the fluctuations and plotting the vortex center location for each sample gives the distribution showed in figure 6.10. It can be seen that the vortex core is in fact "dancing" around, and that the center locations are within a radius of r/R of 0.004 from the reactor center. The corresponding result from the PIV data shows a similar pattern, but here the core is moving more, and the corresponding radius is $r/R = 0.05$. It is quite expected that the unsteadiness of the vortex core is not fully captured by the simulation, because the inlet conditions used in the simulation are constant in time. Therefore, at any given time, all four inlets have the same values in the simulation. In the experiment, on the other hand, even though the time averaged flow in each inlet is constant and equal for all inlets, the instantaneous velocities are not. The chaotic motion transfers to the reactor center causing more vortex core movement than what is seen in the simulation. In a mixing perspective, the movement of the core may be important as it stirs the fluid in the reactor and enhances velocity fluctuations. A numerical method that is not able to capture the right amount of vortex "dancing" may therefore not be an optimal basis for the prediction of the mixing performance and the FNP process in the reactor.

Profiles from the three measurement planes are compared between simulation and experimental results. Figure 6.11 shows the mean tangential velocity component and figure 6.12 displays the mean radial velocity. It is seen that the tangential velocity does not vary much between the planes. This is true both for simulation and experiment,

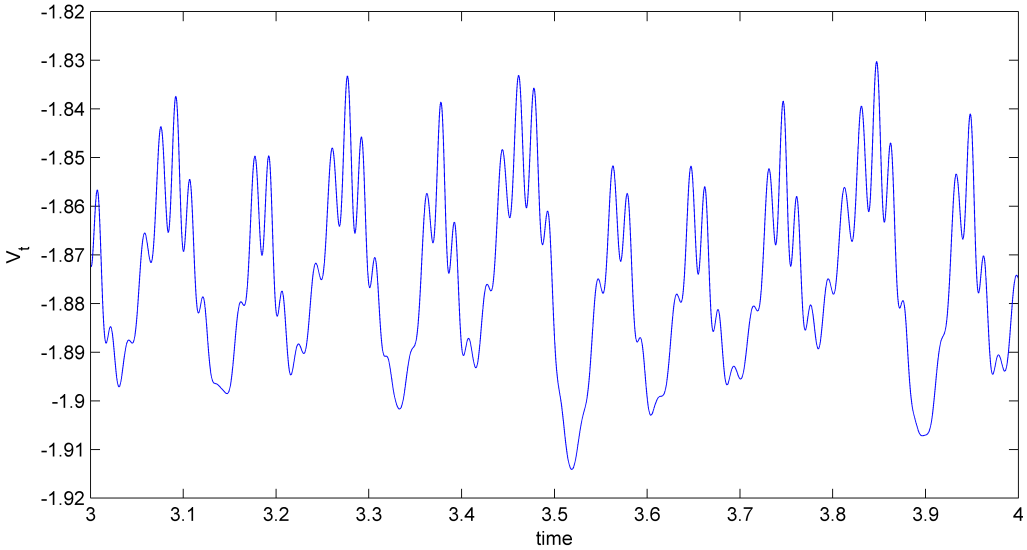

Figure 6.9: Time variations of tangential velocity in a fixed point at $r/R = 0.07$.

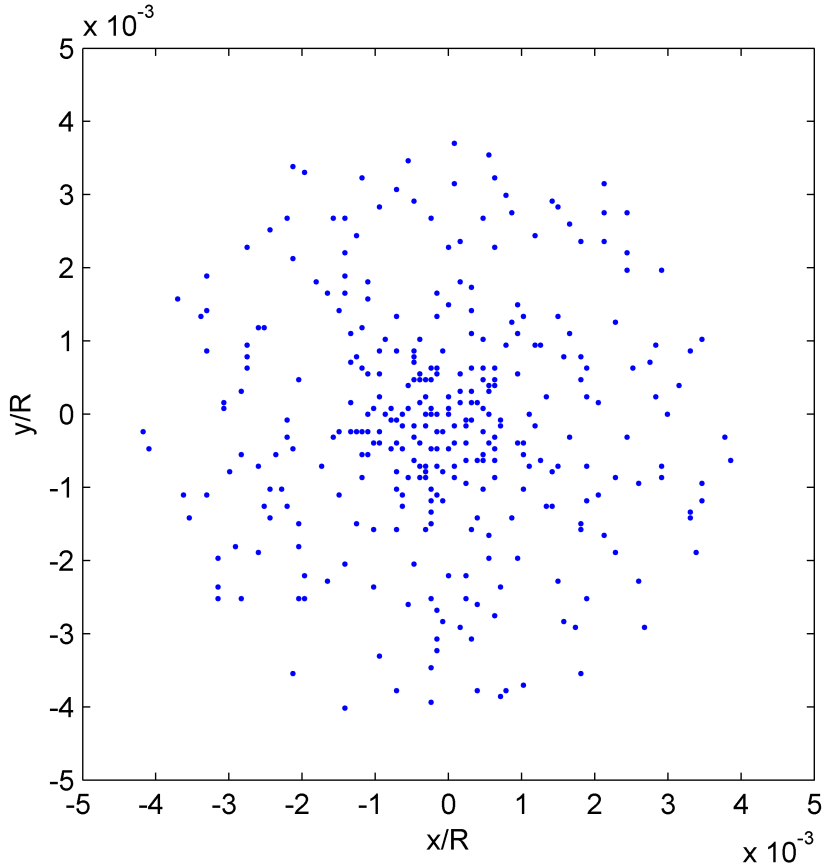

Figure 6.10: Instantaneous vortex core locations in center plane of reactor.

but the experiment shows some more difference in peak velocity magnitude between the planes than the simulation does. In addition, at the lowest plane the mean tangential velocity measured by PIV goes towards zero as r/R approaches one. This is not seen in the simulation results, nor in the other two planes. The radial velocity component varies much more between the planes. Common for the radial velocity profiles are that they are negative in most of the reactor and peak in the center. The highest radial velocity value in the three planes is found in the center of the bottom plane, where the radial velocity is 0.15 m/s. The high positive radial velocity is likely an effect of the recirculation zone transporting fluid downwards that eventually must move out from the center. In the experiment, the highest radial velocity magnitudes are seen in the lower plane, and this agrees with what was suggested previously, namely that fluid is extracted from the bottom. The center plane is both in the simulation and in the experiment the plane where the axial velocities have the lowest magnitude, indicating that little fluid is extracted here. In the simulation, the highest radial velocity magnitudes are found in the top plane and this profile actually agrees quite well with the bottom plane experimental profile. This is because, as described earlier, more fluid is extracted from the top part of the reactor in the LRR simulation. This is visible in figure 6.17. Fluid escaping out of the reactor from the top rather than being pulled into the vortex from the bottom is likely to affect the predicted mixing performance inside the reactor.

The LRR simulation mean field of the tangential, radial and axial velocity, respectively, in the horizontal center plane of the reactor are displayed in figures 6.13 to 6.15. The tangential velocity is seen to be axisymmetrical in large parts of the reactor. Its magnitude increases towards the center of the reactor, but in the very center the tangential velocity drops to zero. Due to the direction of rotation, the tangential velocity is nowhere larger than zero. The radial velocity is not axissymmetrical. The magnitude of the radial velocity is much smaller than that of the tangential velocity, suggesting the swirling motion is dominant. The axial velocity is close to zero in most of the outer parts

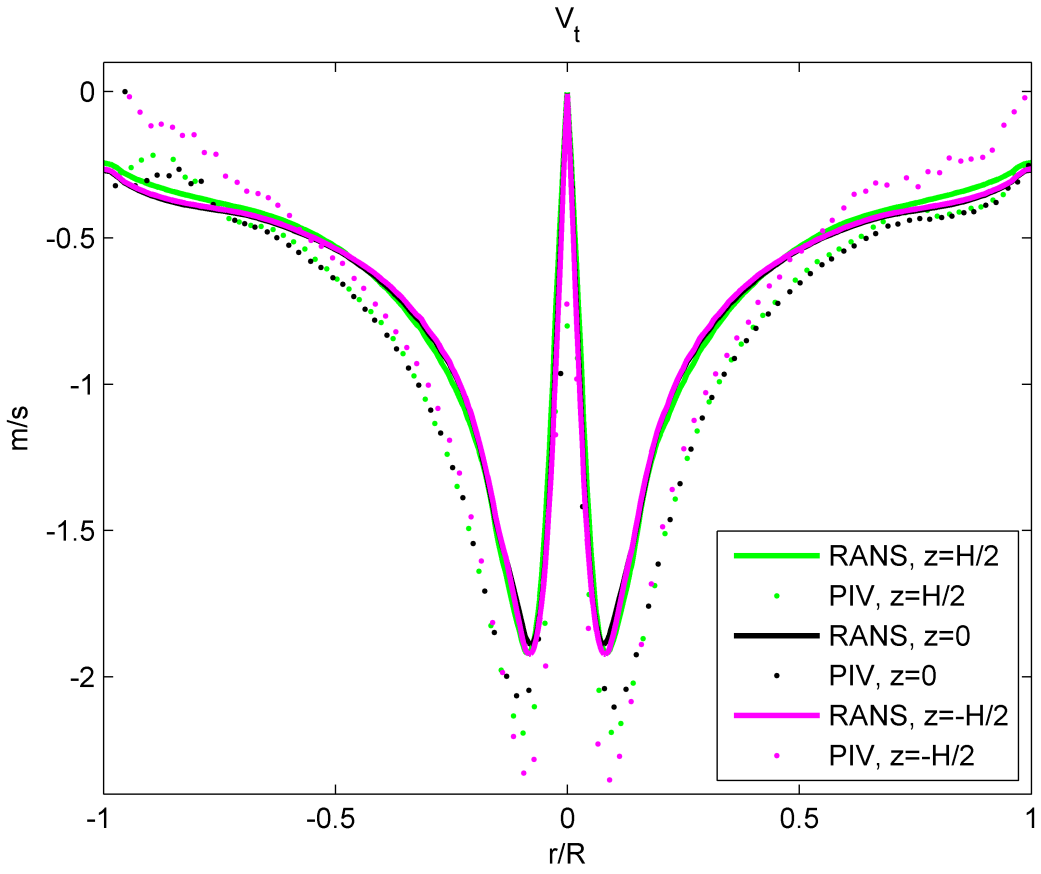

Figure 6.11: Mean tangential velocity profiles across reactor in three planes, z=H/2, z=0 and z=-H/2. RANS results (lines) compared to PIV data (symbols).

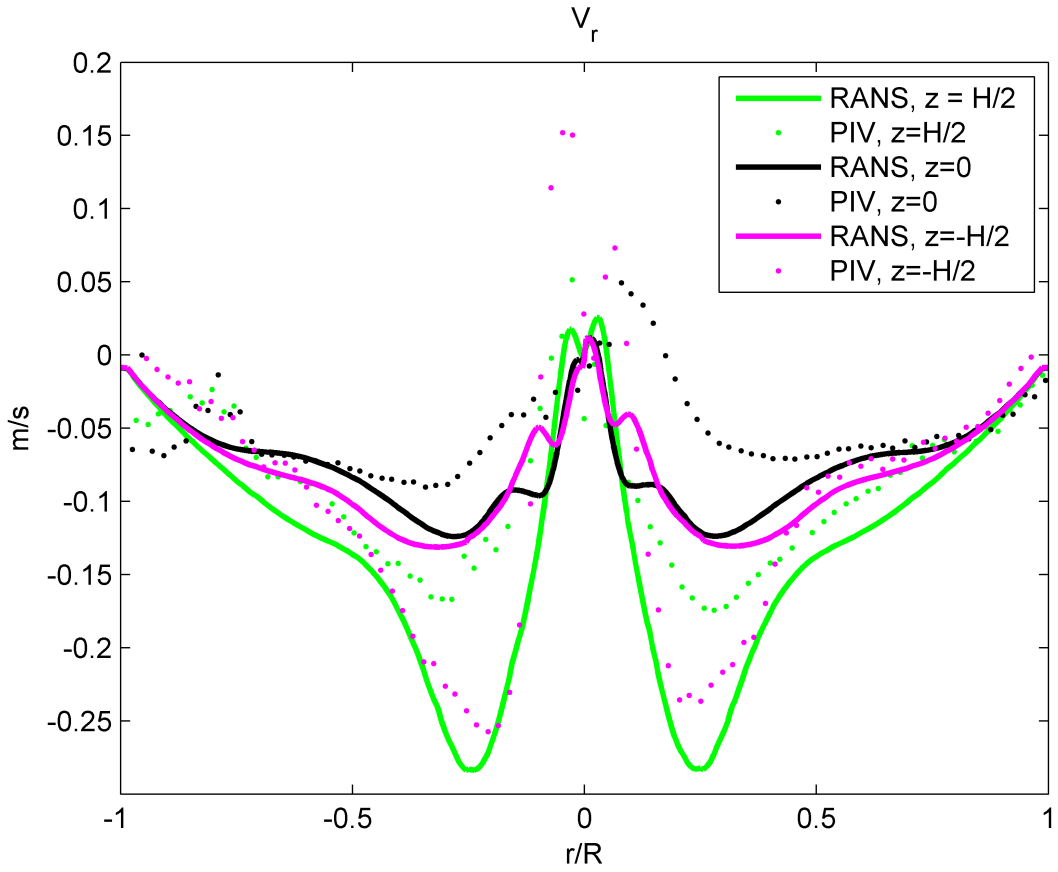

Figure 6.12: Mean radial velocity profiles across reactor in three planes, z=H/2, z=0 and z=-H/2. RANS results (lines) compared to PIV data (symbols).

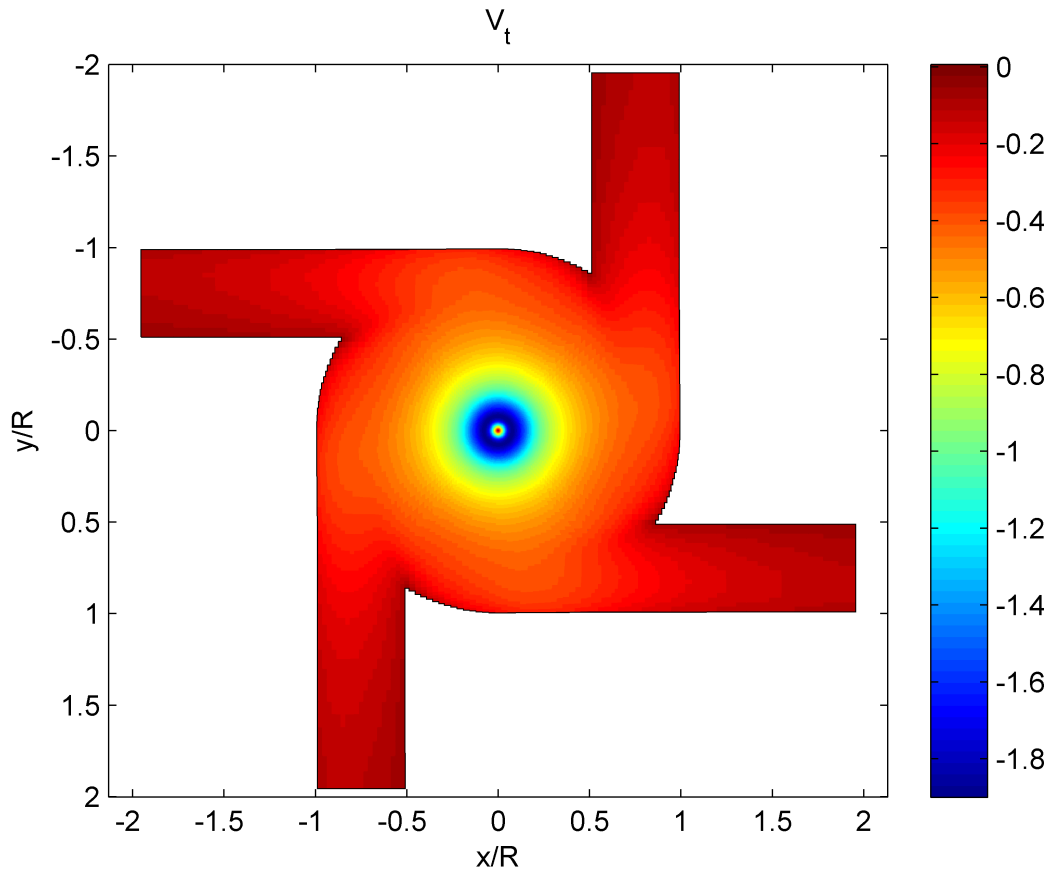

Figure 6.13: Tangential velocity in center plane of reactor. Results using LRR turbulence model. Velocity in m/s.

of the reactor, and increases rapidly towards the center. The region of high axial velocity corresponds quite accurately to the size of the outlet pipe which has a radius 1/4 of the reactor radius, R. It is reasonable to assume that a different outlet pipe diameter would give a different size of the high-magnitude region of axial velocity. In the very center of the reactor, the mean axial velocity actually takes a negative value, meaning fluid is flowing downwards. This is evidence of a recirculation zone in the center of the reactor.

The mean tangential, radial and axial velocity in a vertical center plane of the domain, normal to the y-axis, are shown in figures 6.16 to 6.18. It is seen that the tangential velocity does not change much with height inside the reactor. The tangential velocity has highest magnitude in the center part of the reactor and decays with downstream

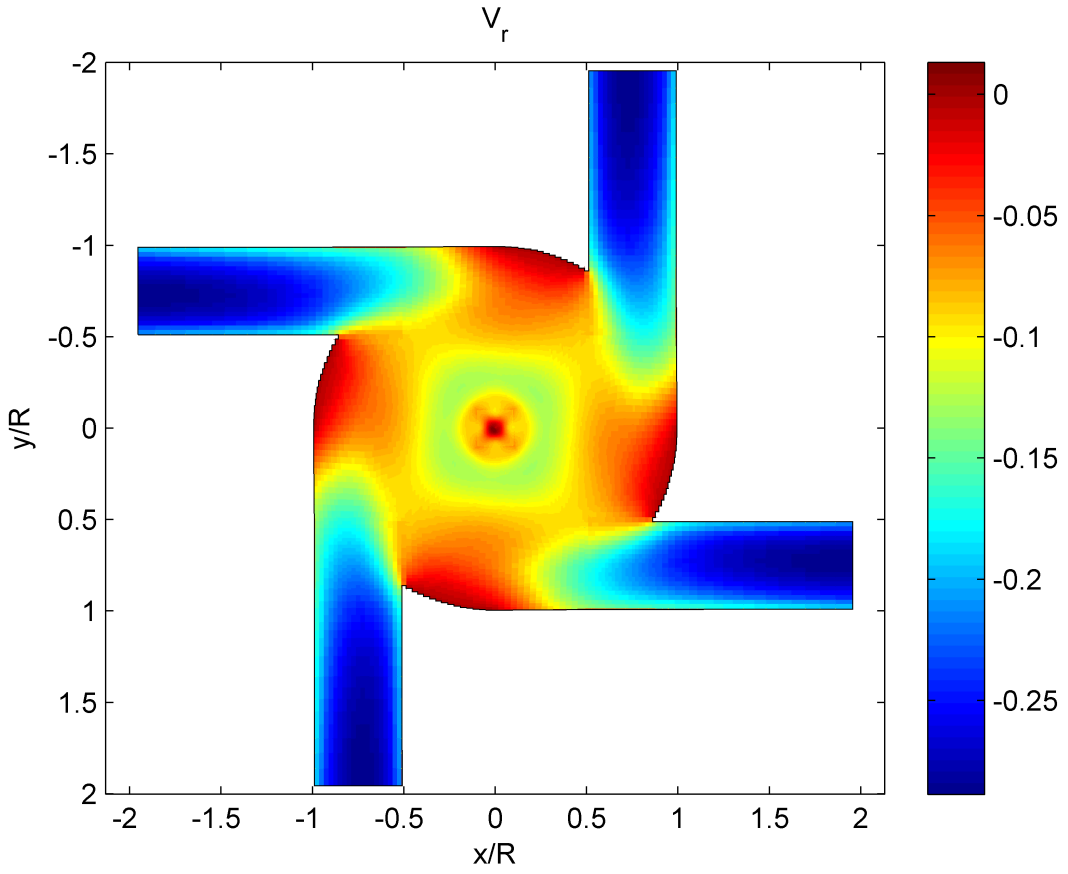

Figure 6.14: Radial velocity in center plane of reactor. Results using LRR turbulence model. Velocity in m/s.

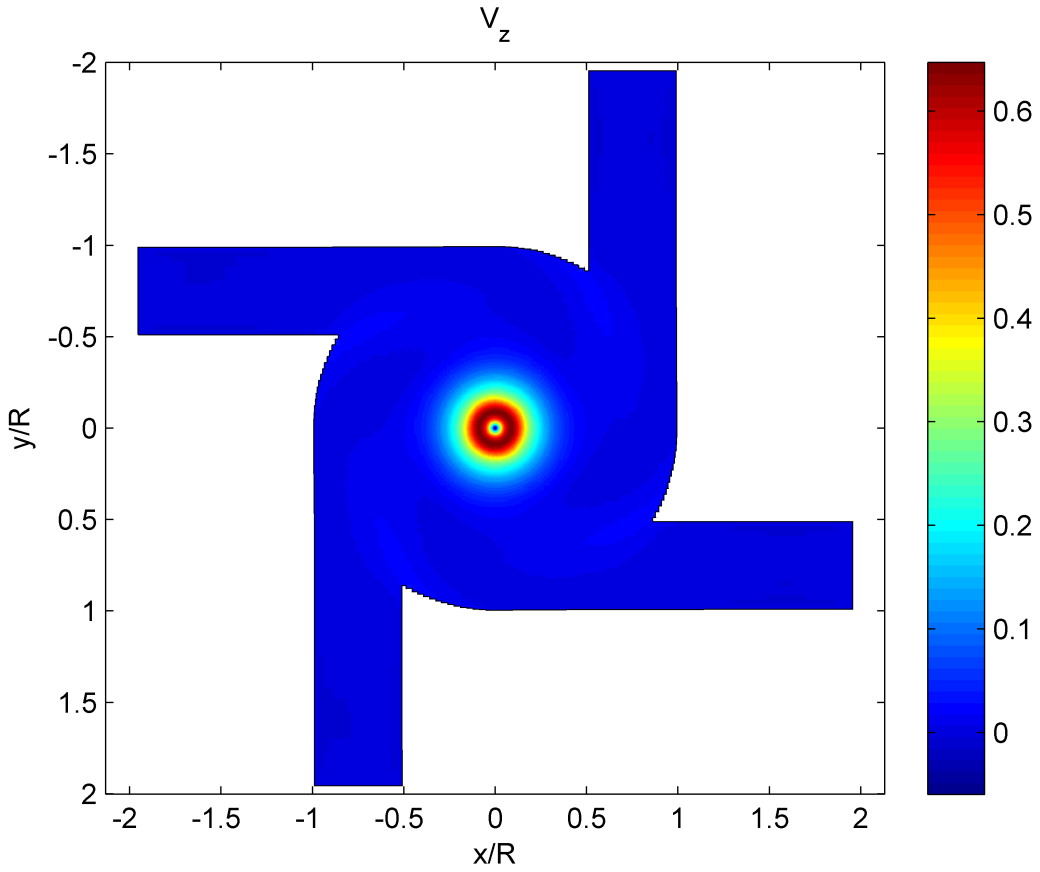

Figure 6.15: Axial velocity in center plane of reactor. Results using LRR turbulence model. Velocity in m/s.

distance in the outlet pipe. The non-zero tangential velocity in the outlet, also at the most downstream location, shows that the fluid is swirling also here. This means that flow quite far downstream of the reactor can be expected to affect the flow inside the reactor and thus affect the mixing performance. Therefore, care must be taken when designing the outlet, both for simulation and for the actual reactor. The strong swirl in the outlet pipe means that streamline curvature effects by the wall could be influential. The use of standard wall functions may therefore not be a good choice here. The effect of this type of curvature would be increased turbulence near the wall compared to standard boundary layers. However, as was seen in figure 6.6, the swirl is rather underpredicted than overpredicted. One could imagine that if the turbulence level at the wall in the outlet pipe is in fact too low because of the standard wall functions, the skin friction is underpredicted and thus there will be less resistance to the rotating motion, causing the swirl to be overpredicted. This would likely have been reflected in the swirling motion also inside the reactor. Following this reasoning, the use of standard wall functions in the outlet is not a problem. Nonetheless, further research on this matter is recommended. Inside the reactor itself, the standard wall functions do not pose a problem because the area of curved walls is very small here.

Negative radial velocity means flow towards the center. This is found mainly close to the reactor ceiling and reactor floor, as can be seen in figure 6.17. Near the opening to the outlet pipe, the radial velocity is at its maximum. This can be seen as an indication that the main vortex is fed from the bottom and top and that little fluid is entrained in between. The radial velocity is slightly positive in the beginning of the outlet pipe. This is likely due to recirculation zones at the outlet pipe wall. These are clearly visible as negative axial velocity in figure 6.18 where one main recirculation zone is found in the center, extending from near the bottom of the reactor and into the outlet pipe, and two minor recirculation zones are seen at the outlet pipe wall close to the reactor.

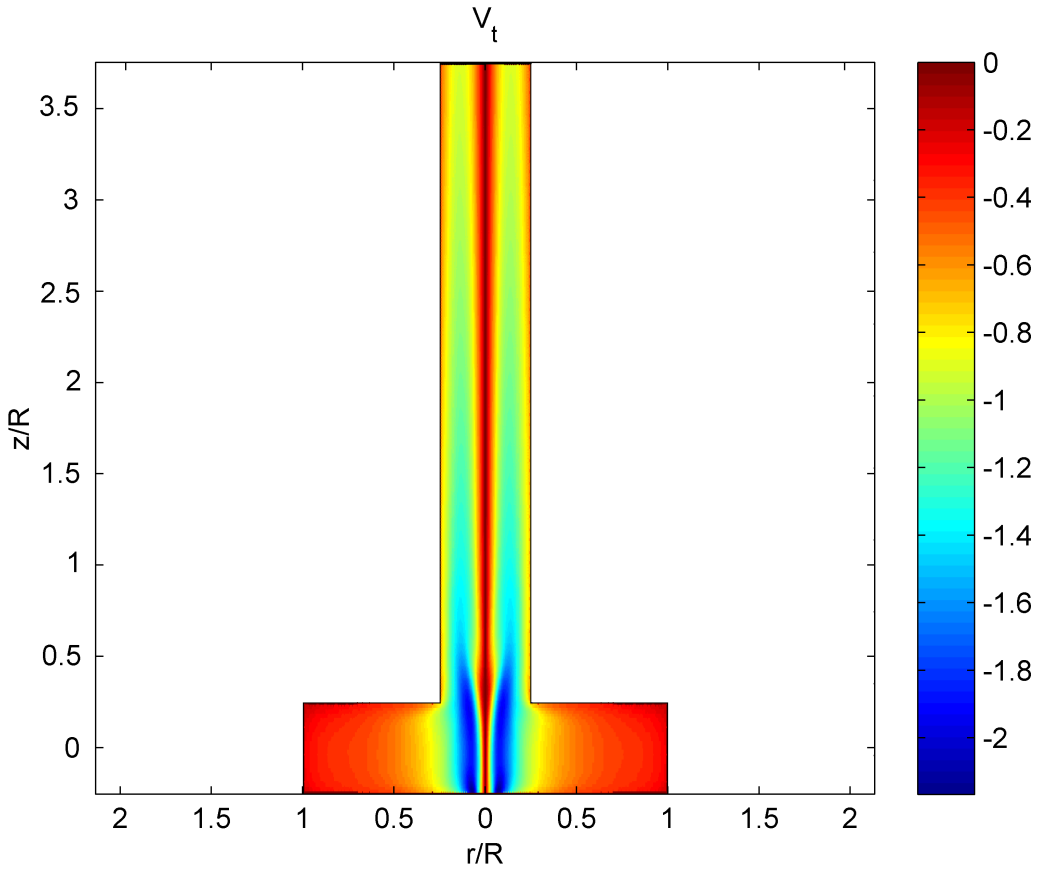

Figure 6.16: Tangential velocity in vertical center plane of reactor. Results using LRR turbulence model. Velocity in m/s.

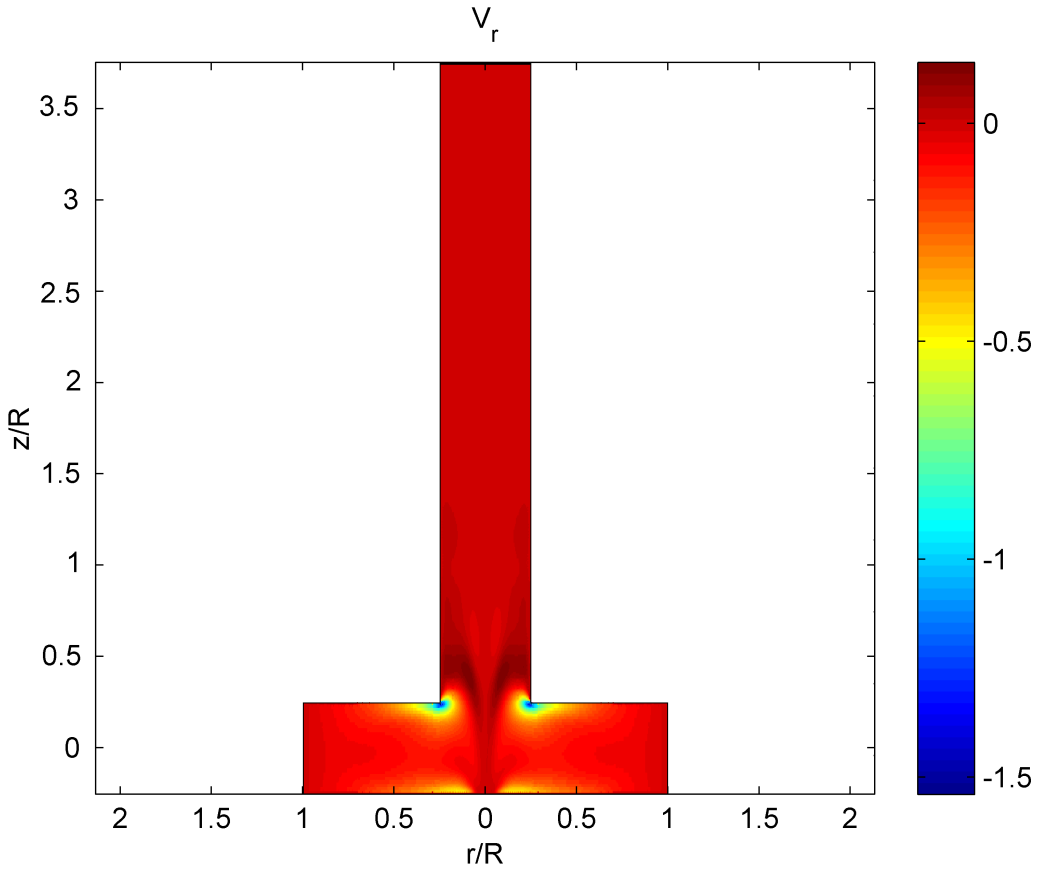

Figure 6.17: Radial velocity in vertical center plane of reactor. Results using LRR turbulence model. Velocity in m/s.

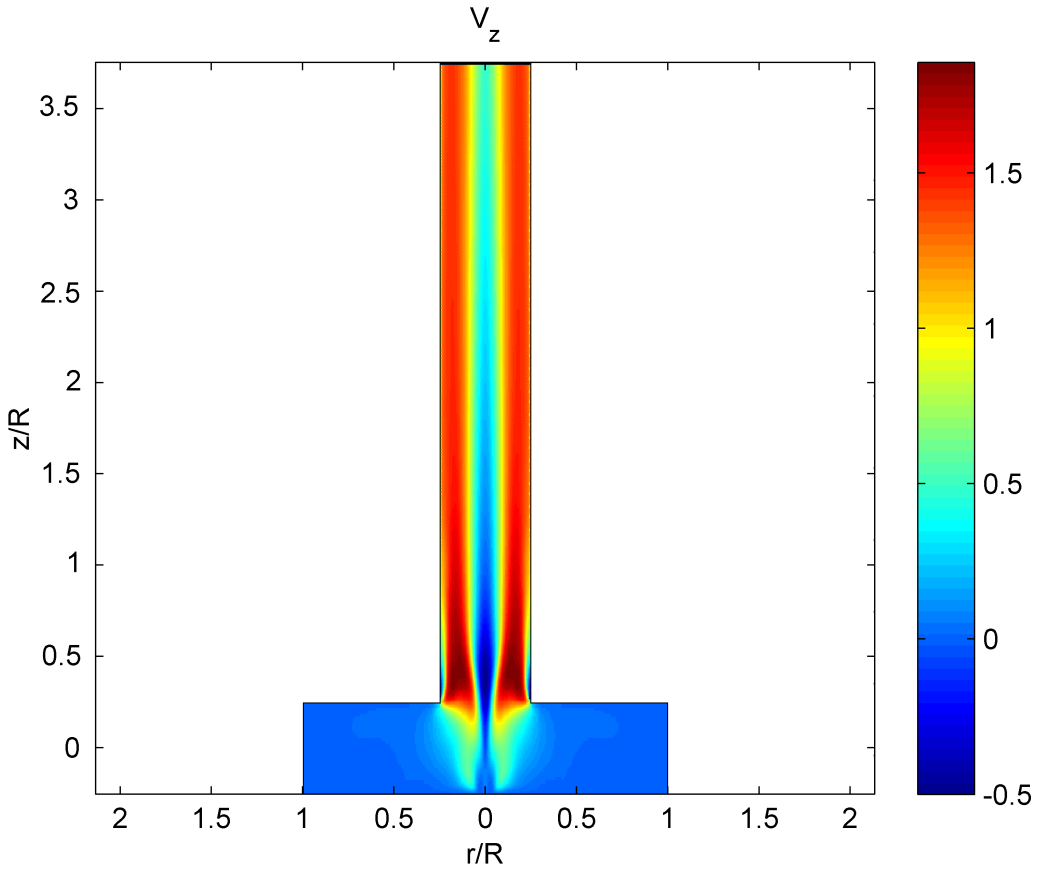

Figure 6.18: Axial velocity in vertical center plane of reactor. Results using LRR turbulence model. Velocity in m/s.

6.5 Summary and Conclusions

The flow in the four-inlet reactor at inlet Reynolds number of 6275 has been studied. The reactor flow features a main vortex in the center that extends far into the outlet pipe. The motion corresponds to solid body rotation in the inner part, and free vortex in the outer part. The vortex core is found to be "dancing" around a central position. The study shows that fluid is extracted from the reactor chamber into the outlet pipe, mainly from the top and bottom of the reactor and not much from in between.

RANS simulations of the flow in the reactor were performed and the simulation parameters were assessed. The unsteadiness of the flow makes URANS necessary. It was found that the grid must be fine in the central parts of the reactor in order to capture the flow dynamics properly. Using the LRR or v2fr turbulence models, the simulations were able to capture the main features of the flow. However, some discrepancies between simulation and experimental results were found, and peak velocity values were not accurately predicted by the simulations. The swirling motion does seem to stabilize the turbulence, making it possible for the laminar model to perform better than the v2f model. The simulation predicted the "dancing" vortex core, but the movement was much less than what was found in the experiment.

Both the stabilization of turbulence and the solid body rotation are phenomena that can be expected to have negative effect on the reactor's mixing performance. The "dancing" vortex core, on the other hand, is likely affecting the mixing in a positive way. Further examinations will be necessary in order to investigate these effects. Future work should include concentration measurements in the reactor and scalar transport simulations of the flow in the reactor in order to assess the mixing performance and aid the development of reliable numerical methods for predicting mixing in the reactor. In addition, further Reynolds numbers and inlet flow rate configurations should be investigated, both experimentally and numerically.

A recommended step to be taken in the further attempt of improving the CFD predictions is comparing the Reynolds stresses between the different turbulence models and to the experimental data. This can give very valuable insight into the strengths and weaknesses of the turbulence models. The high grid requirements and unsteady nature of the flow cause the computer costs in this work to be quite high. It is therefore appropriate to consider using large eddy simulation (LES) instead of RANS. This could potentially improve the fit with the experimental data and better capture the vortex core movement.

CHAPTER 7. SUMMARY AND FUTURE WORK

7.1 Summary

Turbulent mixing processes in three different flow configurations have been studied using a combination of experimental data and CFD. A turbulent wake and turbulent jet with co-flow in a rectangular reactor have been studied through LES and PIV, PLIF as well as simultaneous PIV/PLIF, while RANS simulations and stereo-PIV were used to study the vortex flow in a four-inlet vortex reactor. The investigations not only gave insight into the flow features and mixing mechanisms of the flows, but also provided information on the effect of simulation parameters and the applicability of the numerical methods.

The turbulent confined wake at Reynolds number 37,500 was simulated by LES and the results were compared to PIV data of the same flow. Through a series of pre-simulations the effects of simulation parameters were investigated and it was established that the accuracy of the predictions greatly depends on the inlet condition in this flow. A digital filter method based on PIV data at the inlet was used to generate turbulent inflow velocities. With appropriate filter length scales the simulation was able to predict the mean and fluctuating velocity fields in the wake. Taking advantage of the detailed nature of PIV data, closer examination of the simulation results was possible. The study revealed that the simulation also was able to reproduce the turbulent energy dissipation in the wake appropriately. Through comparison of two-point velocity correlations it was shown that the main coherent structures of the flow were well predicted by the

simulation, suggesting that the dominant mixing mechanisms in the wake are captured in the simulation.

LES predictions of the transport of a passive scalar in the same wake flow was validated using simultaneous PIV/PLIF data. The numerical schemes used to discretize the transport equation for the passive scalar proved to be influential on the quality of the predictions. Second order time scheme was found to be necessary. Of the spatial schemes, a linear scheme with limiter was found to keep the solution bounded and at the same time predict appropriate mixing rates. Simultaneous PIV/PLIF data made it possible to obtain turbulent fluxes and compare the simulation and experiment profiles. The agreement was found to be good. Furthermore, the turbulent diffusivities were computed and compared. The agreement between simulation and experiment was very good and is a strong indication that the simulation method is able to capture the mixing mechanisms of the flow. This was further confirmed by comparing two-point spatial correlations of scalar and velocity. The simulation correlations matched those of the experiment well, showing that not only are the coherent turbulent structures of the flow well predicted, also their effect on the transport of the passive scalar is captured.

These two studies showed that LES can be an excellent tool in studying turbulent transport in the confined wake but that care must be taken when choosing inlet velocity condition and numerical schemes for the passive scalar.

Transport of passive scalar in the turbulent jet with co-flow in a rectangular channel was simulated using LES. Also here the digital filter method was used to generate inflow velocities and the passive scalar transport was modeled using the gradient diffusion hypothesis. Although finite difference method was used to compute the velocity field, a finite volume approach was used for the passive scalar in order to ensure conservation of the passive scalar. The results were compared to simultaneous PIV/PLIF data. The flow was well predicted by the simulation; however, the simulation did predict a mixing rate somewhat higher than the experimental one. This caused turbulent fluxes to be higher

in the simulation than in the experiment. Two-point spatial correlations of velocity and concentration were computed both for simulation and experiment. Coherent structures were found in the free shear layers, and the simulation correlations compared well to the experimental ones.

The transport mechanisms in the turbulent jet were studied in more detail in Chapter 5. It was shown that both at Reynolds number 20,000 and 50,000, the assumption of constant, scalar diffusivity is not appropriate. One off-diagonal component of the turbulent diffusivity tensor was shown to be non-zero, and the turbulent diffusivity was found to vary with position, for both Reynolds numbers. Furthermore, it was shown that the turbulent flux does not align with the mean concentration gradient, for any of the Reynolds numbers. The LES proved to be able to capture these features. The values of turbulent diffusivity components as well as the angle between turbulent fluxes and mean concentration gradient were found to be consistent across the two Reynolds numbers.

LES seemed to perform a little better in the wake case than in the jet case. Differences in the simulation procedure can be an explanation. For the wake, OpenFOAM with finite volume procedure was used, while in the jet case, a finite difference code was used. It might also be that the difference in performance comes from the different flow characteristics. For example, the turbulent fluxes in the wake have, relatively, much lower magnitude than the fluxes in the jet.

The flow in a four-inlet vortex reactor was studied by means of RANS simulation and PIV. The investigation showed that a vortex is present in the center of the reactor, extending up into the outlet pipe. The vortex core is found to be moving around the reactor center. This was seen both in the experimental data and in the simulation, although the movement was much smaller in the simulation. The tangential velocity profiles agrees with that of a forced vortex in the central region and a free vortex in the outer region. A recirculation zone is found in the reactor center. Numerical investigations showed that only when the grid was fine enough would the simulation predict

the recirculation zone. The Reynolds stress turbulence model and the v2f model with curvature correction gave the overall best predictions of the flow. However, there were some discrepancies between simulation and experimental velocity profiles, particularly in peak values. The simulation results revealed that the fluid that exits the reactor either is extracted from the top or the bottom of the reactor and not much in between. Based on the findings, recommendations for future work were given.

The work presented in this thesis has shown that CFD in combination with PIV/PLIF data is a very good tool to study mixing in the current flow configurations. This work has additionally demonstrated the value of detailed evaluation of CFD methods and that PIV/PLIF data provides excellent basis for such assessment in complex flow configurations.

7.2 Recommendations for future work

The wake and jet datasets, including passive scalar transport by LES as well as simultaneous PIV/PLIF of each flow, offer the opportunity to compare the two flows with regards to the simulations requirements. This could give interesting insight into how different flow features affect the choice of simulation parameters.

For the four-inlet vortex reactor, the next step is to evaluate more closely the RANS results, including comparisons of turbulent kinetic energy, energy dissipation rates and Reynolds stresses, between simulation and experiment. The lessons learned from such investigations will be helpful in detecting where the weaknesses of the RANS in predicting the vortex flow lies. This may help to find the right measures to be taken in order to improve the simulation results. An advice for future work is to consider LES. Once the velocity field is well predicted, the following step will be to simulate the mixing in the reactor and, ultimately, predict the FNP process.

BIBLIOGRAPHY

[1] R. J. Adrian. Particle-imaging techniques for experimental fluid-mechanics. *Annual Review of Fluid Mechanics*, 23:261–304, 1991.

[2] R. J. Adrian, K. T. Christensen, and Z. C. Liu. Analysis and interpretation of instantaneous turbulent velocity fields. *Experiments in Fluids*, 29:275–290, 2000.

[3] A. Agrawal and A. K. Prasad. Organizational modes of large-scale vortices in an axisymmetric turbulent jet. *Flow, Turbulence and Combustion*, 68:359–377, 2002.

[4] R. A. Antonia, L. W. B. Browne, A. J. Chambers, and S.B. Rajagopalan. Budget of the temperature variance in a turbulent plane jet. *International Journal of Heat and Mass Transfer*, 26(1):41–48, 1983.

[5] G. K. Batchelor and A. E. Gill. Analysis of the stability of axisymmetric jets. *Journal of Fluid Mechanics*, 14(04):529–551, 1962.

[6] A. Borg, J. Bolinder, and L. Fuchs. Simultaneous velocity and concentration measurements in the near field of a turbulent low-pressure jet by digital particle image velocimetry-planar laser-induced fluorescence. *Experiments in Fluids*, 31(2):140–152, August 2001.

[7] I. Boxx, C. Heeger, R. Gordon, B. Böhm, M. Aigner, A. Dreizler, and W. Meier. Simultaneous three-component PIV/OH-PLIF measurements of a turbulent lifted, C3H8-Argon jet diffusion flame at 1.5 kHz repetition rate. *Proceedings of the Combustion Institute*, 32:905–912, 2009.

[8] J. C. Cheng and R. O. Fox. Kinetic modeling of nanoprecipitation using CFD coupled with a population balance. *Ind. Eng. Chem. Res*, 49:10651–10662, 2010.

[9] J. C. Cheng, M. G. Olsen, and R. O. Fox. A microscale multi-inlet vortex nanoprecipitation reactor : Turbulence measurement and simulation. *Applied Physics Letters*, 94:204104, 2009.

[10] Y. Cheng, M. M. Torregrosa, A. Villegas, and F. J. Diez. Time Resolved Scanning PIV measurements at fine scales in a turbulent jet. *International Journal of Heat and Fluid Flow*, 32:708–718, 2011.

[11] J. P. Chollet and M. Lesieur. Parameterization of small scales of three-dimensional isotropic turbulence utilizing spectral closures. *Journal of the Atmospheric Sciences*, 38:2747–2757, 1981.

[12] A. Chorny and V. Zhdanov. Turbulent mixing and fast chemical reaction in the confined jet flow at large Schmidt number. *Chemical Engineering Science*, 68:541–554, 2012.

[13] K. T. Christensen. The influence of peak-locking errors on turbulence statistics computed from PIV ensembles. *Experiments in Fluids*, 36:484–497, 2004.

[14] G. S. Constantinescu and K. D. Squires. LES and DES investigations of turbulent flow over a sphere at Re = 10,000. *Flow, Turbulence and Combustion (formerly Applied Scientific Research)*, 70:267–298, 2003.

[15] J. P. Crimaldi and J. R. Koseff. High-resolution measurements of the spatial and temporal scalar structure of a turbulent plume. *Experiments in Fluids*, 31:90–102, 2001.

[16] W. J. A. Dahm and P. E. Dimotakis. Measurements of entrainment and mixing in turbulent jets. *AIAA journal*, 25(9):1216–1223, 1987.

[17] A. Darisse, J. Lemay, and A. Benaïssa. LDV measurements of well converged third order moments in the far field of a free turbulent round jet. *Experimental Thermal and Fluid Science*, 44:825–833, 2013.

[18] P. E. Dimotakis. Turbulent mixing. *Annual Review of Fluid Mechanics*, 37:329–356, 2005.

[19] P. E. Dimotakis, R. C. Miake-Lye, and D. A. Papantoniou. Structure and dynamics of round turbulent jets. *Physics of Fluids*, 26(11):3185–3192, 1983.

[20] K. Duraisamy and G. Iaccarino. Curvature correction and application of the v2-f turbulence model to tip vortex flows. *Center forTurbulence Research Annual Research Briefs*, pages 157–168, 2005.

[21] P. A. Durbin. Separated flow computations with the k-epsilon-v-squared model. *AIAA journal*, 33(4):659–664, 1995.

[22] K. W. Everitt and A. G. Robins. The development and structure of turbulent plane jets. *Journal of Fluid Mechanics*, 88(03):563–583, 1978.

[23] H. Feng, M. G. Olsen, J. C. Hill, and R. O. Fox. Simultaneous velocity and concentration field measurements of passive-scalar mixing in a confined rectangular jet. *Experiments in Fluids*, 42:847–862, 2007.

[24] H. Feng, M. G. Olsen, J. C. Hill, and R. O. Fox. Investigation of passive scalar mixing in a confined rectangular wake using simultaneous PIV and PLIF. *Chemical Engineering Science*, 65:3372–3383, 2010.

[25] H. Feng, M. G. Olsen, Y. Liu, R. O. Fox, and J. C. Hill. Investigation of turbulent mixing in a confined planar-jet reactor. *AIChE Journal*, 51(10):2649–2664, 2005.

[26] J. A. Ferre, J. C. Mumford, A. M. Savill, and F. Giralt. Three-dimensional large-eddy motions and fine-scale activity in a plane turbulent wake. *Journal of Fluid Mechanics*, 210:371–414, 1990.

[27] J. H. Ferziger and M. Peric. *Computational Methods for Fluid Dynamics*. Springer, 3 edition, 2002.

[28] C. Fureby, G. Tabor, H. G. Weller, and A. D. Gosman. A comparative study of subgrid scale models in homogeneous isotropic turbulence. *Physics of Fluids*, 9(5):1416–1429, 1997.

[29] T. B. Gatski, M. Y. Hussaini, and J. L. Lumley. *Simulation and Modeling of Turbulent Flows*. Oxford University Press, 1996.

[30] M. Germano, U. Piomelli, P. Moin, and W. H. Cabot. A dynamic subgrid-scale eddy viscosity model. *Physics of Fluids A: Fluid Dynamics*, 3:1760–1765, 1991.

[31] S. Ghosal and M. M. Rogers. A numerical study of self-similarity in a turbulent plane wake using large-eddy simulation. *Physics of Fluids*, 9(6):1729, 1997.

[32] A. Gokarn, F. Battaglia, R. O. Fox, J. C. Hill, and J. Reveillon. Large eddy simulations of incompressible turbulent flows using parallel computing techniques. *International Journal for Numerical Methods in Fluids*, 56:1819–1843, 2008.

[33] S. V. Gordeyev and F. O. Thomas. Coherent structure in the turbulent planar jet. Part 1. Extraction of proper orthogonal decomposition eigenmodes and their self-similarity. *Journal of Fluid Mechanics*, 414:145–194, July 2000.

[34] S. V. Gordeyev and F. O. Thomas. Coherent structure in the turbulent planar jet. Part 2. Structural topology via POD eigenmode projection. *Journal of Fluid Mechanics*, 460:349–380, June 2002.

[35] P. Gousseau, B. Blocken, and G. J. F. van Heijst. Large-Eddy Simulation of pollutant dispersion around a cubical building: Analysis of the turbulent mass transport mechanism by unsteady concentration and velocity statistics. *Environmental Pollution*, 167:47–57, 2012.

[36] H. L. Grant. The large eddies of turbulent motion. *Journal of Fluid Mechanics*, 4(2):149–190, 1958.

[37] C. Gromke, R. Buccolieri, S. Di Sabatino, and B. Ruck. Dispersion study in a street canyon with tree planting by means of wind tunnel and numerical investigations - Evaluation of CFD data with experimental data. *Atmospheric Environment*, 42:8640–8650, 2008.

[38] F. Guillard, R. Fritzon, J. Revstedt, C. Trägårdh, M. Alden, and L. Fuchs. Mixing in a confined turbulent impinging jet using planar laser-induced fluorescence. *Experiments in Fluids*, 25:143–150, 1998.

[39] D. Han and M.G. Mungal. Simultaneous measurements of velocity and CH distributions. Part 1: jet flames in co-flow. *Combustion and Flame*, 132:565–590, 2003.

[40] F. H. Harlow and J. E. Welch. Numerical calculation of time-dependent viscous incompressible flow of fluid with free surface. *Physics of Fluids*, 8:2182, 1965.

[41] A. J. Hoekstra, J. J. Derksen, and H. E. A. Van Den Akker. An experimental and numerical study of turbulent swirling flow in gas cyclones. *Chemical Engineering Science*, 54:2055–2065, 1999.

[42] K. Horiuti. Large eddy simulation of turbulent channel flow by one-equation modeling. *Journal of the Physical Society of Japan*, 54(8):2855–2865, 1985.

[43] R. Hreiz, C. Gentric, and N. Midoux. Numerical investigation of swirling flow in cylindrical cyclones. *Chemical Engineering Research and Design*, 89:2521–2539, 2011.

[44] H. Hu, T. Saga, T. Kobayashi, and N. Taniguchi. Simultaneous velocity and concentration measurements of a turbulent jet mixing flow. *Annals of the New York Academy of Sciences*, 972:254–259, 2002.

[45] H. Jasak, H. G. Weller, and A. D. Gosman. High resolution NVD differencing scheme for arbitrarily unstructured meshes. *International Journal for Numerical Methods in Fluids*, 31:431–449, 1999.

[46] B. K. Johnson and R. K. Prud'homme. Flash nano-precipitation of organic actives and block copolymers using a confined impinging jets mixer. *Australian Journal of Chemistry*, 56:1021–1024, 2003.

[47] W. P. Jones and B. E. Launder. The prediction of laminarization with a two-equation model of turbulence. *International journal of heat and mass transfer*, 15:301–314, 1972.

[48] R. D. Keane and R. J. Adrian. Optimization of particle image velocimeters. I. Double pulsed systems. *Measurement Science and Technology*, 1:1202–1215, 1990.

[49] A. M. Kempf. LES validation from experiments. *Flow, Turbulence and Combustion*, 80:351–373, 2008.

[50] M. Klein, A. Sadiki, and J. Janicka. A digital filter based generation of inflow data for spatially developing direct numerical or large eddy simulations. *Journal of Computational Physics*, 186:652–665, 2003.

[51] B. Kong, M.G. Olsen, R.O. Fox, and J.C. Hill. Predictive capability of Large Eddy Simulation for point-wise and spatial turbulence statistics in a confined rectangular jet. *Chemical Engineering Science*, 69:240–256, 2012.

[52] A. G. Kravchenko and P. Moin. Numerical studies of flow over a circular cylinder at Re_D=3900. *Physics of Fluids*, 12(2):403, 2000.

[53] B. E. Launder, G. J. Reece, and W. Rodi. Progress in the development of a Reynolds-stress turbulence closure. *Journal of fluid mechanics*, 68:537–566, 1975.

[54] C. Le Ribault. Large Eddy simulation of passive scalar in compressible mixing layers. *International Journal of Heat and Mass Transfer*, 51:3514–3524, 2008.

[55] S. K. Lele. Compact finite difference schemes with spectral-like resolution. *Journal of Computational Physics*, 103:16–42, 1992.

[56] F. Lemoine, Y. Antoine, M. Wolff, and M. Lebouche. Simultaneous temperature and 2D velocity measurements in a turbulent heated jet using combined laser-induced fluorescence and LDA. *Experiments in Fluids*, 26:315–323, 1999.

[57] M. Lesieur and O. Metais. New trends in large-eddy simulations of turbulence. *Annual Review of Fluid Mechanics*, 28:45–82, 1996.

[58] N. Li, E. Balaras, and U. Piomelli. Brief communications: Inflow conditions for large-eddy simulations of mixing layers. *Physics of Fluids*, 12:935–938, 2000.

[59] D. K. Lilly. A proposed modification of the Germano subgrid-scale closure method. *Physics of Fluids A: Fluid Dynamics*, 4(3):633–635, 1992.

[60] Y. Liu, J. C. Cheng, Y. Liu, R. Prud'homme, and R. O. Fox. Mixing in a multi-inlet vortex mixer (MIVM) for flash nano-precipitation. *Chemical Engineering Science*, 63:2829–2842, 2008.

[61] Y. Liu, H. Feng, M. G. Olsen, R. O. Fox, and J. C. Hill. Turbulent mixing in a confined rectangular wake. *Chemical Engineering Science*, 61:6946–6962, 2006.

[62] P. Lovaraju and E. Rathakrishnan. Experimental studies on co-flowing subsonic and sonic jets. *Flow, Turbulence and Combustion*, 87:115–132, 2011.

[63] OpenCFD Ltd. OpenFOAM. *http://www.openfoam.com/*.

[64] T. S. Lund. Generation of turbulent inflow data for spatially-developing boundary layer simulations. *Journal of Computational Physics*, 140:233–258, 1998.

[65] N. N. Mansour, J. Kim, and P. Moin. Reynolds-stress and dissipation-rate budgets in a turbulent channel flow. *Journal of Fluid Mechanics*, 194:15–44, 1988.

[66] M. Meinke, W. Schröder, E. Krause, and Th. Rister. A comparison of second- and sixth-order methods for large-eddy simulations. *Computers and Fluids*, 31:695–718, 2002.

[67] O. Metais and M. Lesieur. Spectral large-eddy simulation of isotropic and stably stratified turbulence. *Journal of Fluid Mechanics*, 239:157–194, 1992.

[68] R. Mittal and P. Moin. Suitability of upwind-biased finite difference schemes for large-eddy simulation of turbulent flows. *AIAA Journal*, 35(8):1415–1417, 1997.

[69] C. H. Moeng. A large-eddy-simulation model for the study of planetary boundary-layer turbulence. *Journal of the Atmospheric Sciences*, 41(13):2052–2062, 1984.

[70] P. Moin and J. Kim. Numerical investigation of turbulent channel flow. *Journal of Fluid Mechanics*, 118:341–377, 1982.

[71] J. C. Mumford. The structure of the large eddies in fully developed turbulent shear flows. Part 1. The plane jet. *Journal of Fluid Mechanics*, 118:241–268, 1982.

[72] J. C. Mumford. The structure of large eddies in fully developed turbulent shear flows. Part 2. The plane wake. *Journal of Fluid Mechanics*, 137:447–456, 1983.

[73] V. D. Narasimhamurthy and H. I. Andersson. Numerical simulation of the turbulent wake behind a normal flat plate. *International Journal of Heat and Fluid Flow*, 30:1037–1043, 2009.

[74] S. Parneix, P. A. Durbin, and M. Behnia. Computation of 3-D turbulent boundary layers using the V2F model. *Flow, Turbulence and Combustion*, 60:19–46, 1998.

[75] B. A. Pettersson Reif, P. A. Durbin, and A. Ooi. Modeling rotational effects in eddy-viscosity closures. *International journal of heat and fluid flow*, 20:563–573, 1999.

[76] A. J. Prasad, R. J. Adrian, C. C. Landreth, and P. W. Offutt. Effect of resolution on the speed and accuracy of particle image velocimetry interrogation. *Expt. Fluids*, 13:105–116, 1992.

[77] A. K. Prasad. Particle image velocimetry. *Current Science*, 79(1):51–60, 2000.

[78] N. Rajaratnam. *Turbulent jets*. Elsevier Scientific Publishing Company, Amsterdam, 1976.

[79] S. K. Robinson. Coherent motions in the turbulent boundary layer. *Annual Review of Fluid Mechanics*, 23:601–639, 1991.

[80] R. S. Rogallo and P. Moin. Numerical simulation of turbulent flows. *Annual Review of Fluid Mechanics*, 16:99–137, 1984.

[81] R. Rossi and G. Iaccarino. Numerical simulation of scalar dispersion downstream of a square obstacle using gradient-transport type models. *Atmospheric Environment*, 43:2518–2531, 2009.

[82] P. Sagaut. *Large Eddy Simulation for Incompressible Flows*. Springer, 3rd edition, 2006.

[83] K. V. Sharp and R. J. Adrian. PIV study of small-scale flow structure around a Rushton turbine. *AIChE Journal*, 47(4):766–778, 2001.

[84] J. Sheng, H. Meng, and R. O. Fox. A large eddy PIV method for turbulence dissipation rate estimation. *Chemical Engineering Science*, 55:4423–4434, 2000.

[85] Y. Shi, J. C. Cheng, R. O. Fox, and M. G. Olsen. Measurements of turbulence in a microscale multi-inlet vortex nanoprecipitation reactor. *Journal of Micromechanics and Microengineering*, 23, 2013.

[86] Y. Shi, R. O. Fox, and M. G. Olsen. Confocal imaging of laminar and turbulent mixing in a microscale multi-inlet vortex nanoprecipitation reactor. *Applied Physics Letters*, 99:204103, 2011.

[87] J. Smagorinsky. General circulation experiments with the primitive equations, I. The basic experiment. *Monthly Weather Review*, 91(3):99–164, 1963.

[88] M. Stanislas, K. Okamoto, C. J. Kähler, and J. Westerweel. Main results of the Second International PIV Challenge. *Experiments in Fluids*, 39:170–191, 2005.

[89] P. K. Sweby. High resolution schemes using flux limiters for hyperbolic conservation laws. *SIAM Journal on Numerical Analysis*, 21(5):995–1011, 1984.

[90] J. C. Tannehill, D. A. Anderson, and R. H. Pletcher. *Computational Fluid Mechanics and Heat Transfer*. Taylor and Francis, 2nd edition, 1997.

[91] S. Tavoularis and S. Corrsin. Experiments in nearly homogenous turbulent shear flow with a uniform mean temperature gradient. Part 1. *Journal of Fluid Mechanics*, 104:311–347, 1981.

[92] O. Terashima, Y. Sakai, and K.i Nagata. Simultaneous measurement of velocity and pressure in a plane jet. *Experiments in Fluids*, 53:1149–1164, 2012.

[93] A. A. Townsend. Flow patterns of large eddies in a wake and a boundary layer. *Journal of Fluid Mechanics*, 95(3):515–537, 1979.

[94] I. Veloudis, Z. Yang, J. J. McGuirk, G. J. Page, and A. Spencer. Novel implementation and assessment of a digital filter based approach for the generation of LES inlet conditions. *Flow, Turbulence and Combustion*, 79:1–24, 2007.

[95] J. M. Villafruela, F. Castro, and M. T. Parra. Experimental study of parallel and inclined turbulent wall jets. *Experimental Thermal and Fluid Science*, 33:132–139, 2008.

[96] B. Vreman, B. Geurts, and H. Kuerten. Large-eddy simulation of the turbulent mixing layer. *Journal of Fluid Mechanics*, 339:357–390, 1997.

[97] Z. Wang, P. He, Y. Lv, J. Zhou, J. Fan, and K. Cen. Direct numerical simulation of subsonic round turbulent jet. *Flow, Turbulence and Combustion*, 84:669–686, 2010.

[98] Z. Warhaft. Passive scalars in turbulent flows. *Annual Review of Fluid Mechanics*, 32:203–240, 2000.

[99] M. Yoda, L. Hesselink, and M. G. Mungal. The evolution and nature of large-scale structures in the turbulent jet. *Physics of Fluids A: Fluid Dynamics*, 4(4):803–811, 1992.

[100] A. Yoshizawa and K. Horiuti. A statistically-derived subgrid-scale kinetic energy model for the large-eddy simulation of turbulent flows. *Journal of the Physical Society of Japan*, 54(8):2834–2839, 1985.